Archives of Computational Methods in Engineering manuscript No.
(will be inserted by the editor)

Modelling techniques for vibro-acoustic dynamics of poroelastic materials

Elke Deckers · Stijn Jonckheere · Dirk Vandepitte · Wim Desmet

Received: date / Accepted: date

Abstract Given the quest for mass reduction while preserving proper vibration and acoustic comfort levels in industrial machinery and vehicles, lightweight poroelastic materials have gained a lot of importance. Often, these materials are applied in a multilayered configuration, which can consist of a number of acoustic, elastic, viscoelastic and poroelastic layers. Among these, poroelastic materials are the main focus of this paper. A poroelastic material comprises two constituents, being the elastic solid constituent, also called the frame, and the fluid filling the voids. Depending on the frequency range of interest, the motion of both phases can be strongly coupled. Poroelastic materials can dissipate energy very effectively by structural, thermal and viscous means. Considerable research effort has been put in the development of robust models and prediction techniques which are capable of accurately describing the damping phenomena of these materials. After a broad introduction, this paper reviews the most commonly used models, ranging from simple empirical relations to detailed models accounting for the coupled behaviour of both phases and the CAE modelling techniques currently being applied for the analysis of the time-harmonic vibro-acoustic behaviour of these materials. Commonly used methods, such as the Finite Element Method and the Transfer Matrix Method which are mainly fitted for low-freqency and high-frequency applications, respectively, are discussed as well as extensions to improve their efficiency and applicability. The two final sections pay special attention to the promising Wave Based Method, a Trefftz-based technique, the application range of which was recently extended towards poroelastic problems.

Keywords Poroelastic materials · Biot theory · Wave Based Method

E. Deckers, S. Jonckheere, D. Vandepitte, W. Desmet
KU Leuven, Department of Mechanical Engineering, Celestijnenlaan 300B, box 2420, 3001 Leuven (Heverlee), Belgium
Tel.: +32-16-322480
Fax: +32-16-322987
E-mail: elke.deckers@mech.kuleuven.be

1 Introduction

Growing customer expectations regarding vibro-acoustic performance together with more restrictive regulations on noise emission levels and human exposure to noise, have forced design engineers to take the vibro-acoustic behaviour of their products into account in the development process. Customers judge thsound quality emitted by products, and although this impression is often subjective, it contributes to a large extent to the general appraisal of a product. As such, sound quality has become a commercially important factor. Moreover, an increasing number of studies demonstrate that exposure to higher noise levels can constitute a health hazard; it can for instance induce tinnitus, sleep disturbance and hypertension. Noise exposure is on the increase, implying it will be a major public health problem in the twenty-first century [1]. In consequence of the increased understanding of the relation between exposure to noise and health, European guidelines have been set.

Since the vibro-acoustic properties of a product typically depend on the dimensions and the shape of the product, it is particularly important to consider the vibro-acoustic problem early on in the design phase. Following the current ecological trends, lightweight designs are preferred, to save material costs and to reduce fuel consumption. However, decreasing a compo-

nent's weight, while retaining its stiffness, may lead to strongly reduced noise and vibration insulation properties. In the olden days, a product was mainly designed to meet a few primary goals, such as strength, stiffness and durability. At the end of the design cycle, secondary features such as noise and vibration levels were evaluated and tackled, often leading to heavy and costly add-on solutions. Such a procedure is no longer sufficient to obtain a high-performance, competitive product. Machine and vehicle manufacturers face the challenging task to meet several, often conflicting, design requirements. Additionally, to remain competitive in a fast moving market, the time to market has decreased.

Over the last decades, the advent of powerful Computer Aided Engineering (CAE) tools, and the exponential increase in computational power, have drastically changed the design and development process. Numerical prediction techniques allow the design engineer to evaluate the sensitivity of different parameters to the design criteria, and limit the need for time-consuming and expensive prototypes. Cost-saving measures can be undertaken, leading to a more robust and optimised design and a faster product launch. Due to the increasing importance of vibration comfort, noise emission and sound quality, a vast amount of research is spent on the development of faster and more cost-effective vibro-acoustic prediction methods.

The modelling of the vibro-acoustic behaviour of physical systems is far from trivial. In a general coupled vibro-acoustic system, in which structural and poroelastic components and acoustic cavities mutually interact with each other, the system behaviour is typically determined by the coupled steady-state response of each of the components. In an ideal setting, the design engineer would have a modelling tool at his disposal, allowing calculations over the whole frequency range of interest, which typically runs up to 20kHz. In real life, however, this is not possible due to the limitations of the current CAE tools at hand. Moreover, there is a significantly different response in different frequency regions. In general, three different frequency regions can be identified, which are problem dependent:

Low frequency range – In the low frequency range, the characteristic length of the studied problem is smaller than or in the same order of magnitude as the dominant physical wavelengths in the dynamic response. In this frequency range, the response of the system is determined by well-separated modes and can be predicted by means of deterministic approaches. For vibro-acoustic problems, element based techniques, such as the Finite Element Method (FEM) [2,3] and the Boundary Element Method (BEM) [4,5] are most commonly applied. Element based approaches divide the problem domain or its boundary into a large number of small elements. Inside these elements, the field variables are approximated using simple, often polynomial functions. As wavelenghts shorten with increasing frequency, the element sizes also need to decrease to diminish the effect of interpolation and pollution errors [6–8]. As a consequence, the number of degrees of freedom (DOFs) increases, as does the size of the system matrices, limiting the practical use of element based approaches to low frequency applications.

High frequency range – When the characteristic length of studied problem is much larger than the dominant physical wavelengths in the dynamic response, the considered problem is located in the high frequency range. Typically, the modal density and modal overlap are high and the system is very sensitive to small variations in for instance material properties and geometrical details. As small variabilities are inevitable in real-life applications, the response of one nominal system loses its meaning. As a result, the spatially averaged response of a number of realisations is of interest together with its variance. In this frequency range, statistical techniques are applied; for instance the Statistical Energy Analysis (SEA) [9] is often used for vibro-acoustic analysis. The SEA divides the problem domain into a small number of subsystems in which a spatially averaged estimate of the energy level is obtained. SEA is computationally not demanding, but relies on a number of assumptions, such as for instance a high modal overlap and an energetic similarity of the different subsystems. Since these assumptions are only met above a certain frequency limit, the method is restricted to the high frequency range.

Mid frequency range – In between the low and the high frequency range, a frequency band exists for which currently no mature and adequate prediction techniques are available. However, for many applications, this mid frequency gap coincides with the frequency range where the human hearing is highly sensitive. Therefore, solutions are sought to bridge (part of) this gap, and can be categorised into three classes of approaches:

- *Extend the frequency range of the deterministic approaches.* Optimised solvers [10] and domain decomposition methods [11] can be applied to the element based approaches, knowledge on the dynamic problem can be incorporated [12,13], etc. Trefftz approaches [14], which use exact solutions of the governing differential equation(s) to describe the field variables, can also be consid-

ered in this category. The Wave Based Method, which will be discussed in detail in this paper, belongs to the family of Trefftz approaches.

- *Extend the statistical methods towards lower frequencies.* Approaches belonging to this category, for instance, try to get a better estimation of the SEA parameters [15] or try to relax the assumptions imposed by SEA such that the modal energies in subsystems do not have to be similar [16].
- *Combine deterministic and statistical approaches.* A last category of methods tries to combine the best of two worlds, such that a system which consists of both stiff, deterministic components and flexible, statistical components can be tackled. The hybrid Finite Element/Statistical Energy Analysis, which describes fully deterministic components via FE and highly random components by SEA, is the prime example [17,18].

Mass reduction has become an emerging trend in the transportation as well as in the industrial machinery sector. It is recognised as the only viable path to save costs and to reduce the ecological footprint of a product. Lightweight materials come to the fore, such as composites and sandwich structures. These material concepts are mainly designed for high static stiffness and strength, and good impact resistance. Given their low mass, a major bottleneck in their widespread breakthrough is their strongly deteriorated NVH (Noise Vibration Harshness) behaviour. In this context, lightweight poroelastic materials have gained a lot of importance. These materials provide excellent damping properties and can be applied in stiff, multifunctional, multi-layered structures, which are called trim components.

Although, the focus in this review article is on the application of poroelastic materials in vibro-acoustic settings, poroelastic materials can be found in many branches of engineering and physics. For instance, models for poroelastic materials are widely employed in the field of geo-mechanics [19,20], oceanography [21] and biological systems [22].

Concerning the application of poroelastic materials in vibro-acoustic problem settings, the reference textbook by Allard and Atalla [23] provides a good overview of the developed theories, numerical methods and applications. Due to significant interactions between the two phases, energy is dissipated in the material by thermal and viscous means. Furthermore, due to irreversible losses in the frame material, energy is also dissipated by structural damping. Because of the complexity of the interactions and the significance of these materials, a great amount of research effort has been spent to formulate mathematical models, and to develop numerical prediction techniques to solve these models.

Most of the material parameters of poroelastic materials, taking into account dissipation phenomena, are complex and frequency-dependent. The presence of poroelastic layers in a vibro-acoustic model prohibits efficient numerical solutions. Since two phases need to be represented, the number of DOFs per FE node is high. Additionally, the wavelengths in poroelastic materials are relatively short, requiring fine meshes even at lower frequencies to obtain accurate solutions. By combining several layers with different physical behaviour, near-field effects are present and should be accurately taken into account. As a consequence, element-based approaches are restricted to even lower frequencies when poroelastic materials are present in the problem setting.

The objective of this paper is to give an overview of the state-of-the-art of the models for poroelastic materials and the numerical prediction techniques applied to solve vibro-acoustic problems containing poroelastic materials. The paper is outlined as follows. Section 2 gives an overview of the models used to represent the dynamic behaviour of a poroelastic material. Empirical relations, equivalent fluid and equivalent solid models and the theory of Biot are reviewed. Section 3 describes analytical and numerical modelling techniques to predict the behaviour of a poroelastic material. Element based descriptions and possible reduction schemes, the Transfer Matrix Method and Trefftz approaches are described together with their advantages and drawbacks. Section 4 discusses the general modelling procedure of the WBM, a promising indirect Trefftz method. Section 5 details the capabilities of the WBM for simulating mid-frequency poroelastic problems and demonstrates its use for 2D Cartesian, axisymmetric and 3D vibro-acoustic problems.

2 Models for the acoustic analysis of poroelastic materials

This section presents an overview of the different theories to model the steady-state dynamic behaviour of poroelastic materials in vibro-acoustic applications. A time-harmonic motion with $e^{j\omega t}$-dependence is assumed, where j is the imaginary unit $j^2 = -1$, $\omega{=}2\pi f$ is the circular frequency and t is the time. Different theories are presented, ranging from simple empirical relations to complex models describing the interaction between the two phases.

2.1 Equivalent fluid representations

When it is assumed that the poroelastic material has a rigid, motionless or a limp frame, only one wave type can propagate in the porous material. Its general acoustic behaviour can be described using an equivalent fluid model, governed by the Helmholtz equation [24]:

$$\nabla^2 p^{eq}(\mathbf{r}) + k_{eq}^2(\omega) p^{eq}(\mathbf{r}) = 0, \tag{1}$$

where $p^{eq}(\mathbf{r})$ is the acoustic pressure inside the poroelastic material, the superscript eq indicates that the variable is associated to an equivalent fluid description and the frequency dependent wave number $k_{eq}(\omega)$ is defined as

$$k_{eq}(\omega) = \omega \sqrt{\frac{\rho_{eq}(\omega)}{K_{eq}(\omega)}}, \tag{2}$$

with

$$K_{eq}(\omega) = \frac{K(\omega)}{\phi}, \tag{3}$$

$$\rho_{eq}(\omega) = \frac{\rho(\omega)}{\phi}, \tag{4}$$

the frequency dependent bulk modulus and density of the equivalent fluid, respectively. The effective bulk modulus $K(\omega)$ and the effective density of the fluid $\rho(\omega)$ take into account thermal and viscous effects due to the presence of the pores. The porosity ϕ is required to represent the poroelastic layer as an homogeneous isotropic fluid layer and is defined as the ratio of the volume fraction of air in the open pores and the total volume of material. This quantity is sometimes also called the effective porosity. Any fluid, which is fully enclosed by the solid phase, is considered to be part of the solid frame [25], since no relative motion exists between both phases. Sound absorbing poroelastic materials generally have a high porosity, $\phi \geq 0.95$. From $\rho_{eq}(\omega)$ and $K_{eq}(\omega)$ also the characteristic impedance of the fluid, $Z_{eq,c}$, can be directly obtained:

$$Z_{eq,c}(\omega) = \sqrt{\rho_{eq}(\omega) K_{eq}(\omega)}. \tag{5}$$

In general, the theory is valid as long as the wavelength is much larger than the characteristic dimensions of the pores, and as long as the fluid behaves as an incompressible fluid at the microscopic scale. Different approaches have been proposed to determine expressions for $K_f(\omega)$ and $\rho_f(\omega)$.

2.1.1 Empirical relations

For simplicity reasons, empirical relations based on a small number of parameters are still often used. Delany and Bazley [26] provide a simplified model for fibrous materials, based on the static flow resistivity σ of the porous material. The flow resistivity is the specific flow resistance per unit thickness and is expressed in Nsm^{-4}. According to many fibrous material measurements with porosities close to 1, a good fit of the measured values of k and Z_c can be obtained using the following equations:

$$Z_c = \rho_0 c_0 \left(1 + 9.08 \left(1000 \frac{f}{\sigma}\right)^{-0.75} - j11.9 \left(1000 \frac{f}{\sigma}\right)^{-0.73}\right), \tag{6}$$

$$k = \frac{\omega}{c_0} \left(1 + 10.8 \left(1000 \frac{f}{\sigma}\right)^{-0.70} - j10.3 \left(1000 \frac{f}{\sigma}\right)^{-0.59}\right), \tag{7}$$

where ρ_0 and c_0 are the density of air and the speed of sound in air. The empirical curves may be used with confidence within the interpolating range $0.01 \leq \frac{f}{\sigma} \leq 1$. Miki, however, adapted the Delany-Bazley laws (6)-(7) since he found that the real part of the surface impedance sometimes becomes negative for low frequencies, which is a non-physical result. He proposes the following expressions [27]:

$$Z_c = \rho_0 c_0 \left(1 + 5.50 \left(1000 \frac{f}{\sigma}\right)^{-0.632} - j8.43 \left(1000 \frac{f}{\sigma}\right)^{-0.632}\right), \tag{8}$$

$$k = \frac{\omega}{c_0} \left(1 + 7.81 \left(1000 \frac{f}{\sigma}\right)^{-0.618} - j11.41 \left(1000 \frac{f}{\sigma}\right)^{-0.618}\right). \tag{9}$$

The same boundaries as for the Delany-Bazley laws are applicable. Of course, one single relation does not provide a good prediction for all porous materials. Other models exist, e.g. [28,29], however, the laws by Delany and Bazley and Miki are most widespread.

2.1.2 Rigid frame models with straight pores

The exact solution of the propagation of sound in a uniform, rigid, cylindrical tube was given by Kirchhoff [30], considering the linearised Navier-Stokes equations, the mass conservation equation, the ideal gas law and the thermal conductivity equation. Although these equations hold, they are in general unnecessarily complicated to describe wave propagation in pores. Zwikker and Kosten [24] used a simplified approach

and treated thermal conductivity and viscosity separately. They have shown that, at least in the limiting cases of low and high frequencies, the correct results can be expressed using a complex density and a complex compressibility. The complex density accounts for the viscous losses whereas the complex compressibility (or equivalently bulk modulus) accounts for the thermal dissipation. Later, a.o. Stinson [31] has validated their approximation for a wide range of tube radii and frequencies. The simplified equations can be found in [23,31]. Closed form expressions for $K(\omega)$ and $\rho(\omega)$ can be found for a cylindrical pore and a slit and read:

– Cylindrical pores:

$$\rho(\omega) = \frac{\rho_0}{1 - \frac{2}{s\sqrt{-j}} \frac{J_1\left(s\sqrt{-j}\right)}{J_0\left(s\sqrt{-j}\right)}}, \tag{10}$$

$$K(\omega) = \frac{\gamma P_0}{1 + (\gamma - 1) \frac{2}{s\sqrt{-jPr}} \frac{J_1\left(s\sqrt{-jPr}\right)}{J_0\left(s\sqrt{-jPr}\right)}}, \tag{11}$$

where γ is the ratio of specific heats, P_0 is the ambient pressure of air, $J_0(z)$ and $J_1(z)$ are the ordinary Bessel function of order zero and one, respectively, Pr is the Prandtl number, with c_p the specific heat capacity at constant pressure, η_f the dynamic viscosity and κ the thermal conductivity:

$$Pr = \frac{c_p}{\eta_f \kappa}, \tag{12}$$

and s is given by:

$$s = \sqrt{\frac{\omega \rho_0 R_0^2}{\eta_f}}, \tag{13}$$

where R_0 is the radius of the cylindrical pore.

– Slits:

$$\rho(\omega) = \frac{\rho_0}{1 - \frac{\tanh\left(s'\sqrt{j}\right)}{s'\sqrt{j}}}, \tag{14}$$

$$K(\omega) = \frac{\gamma P_0}{1 + (\gamma - 1) \frac{\tanh\left(s'\sqrt{jPr}\right)}{s'\sqrt{jPr}}}, \tag{15}$$

where s' is given by

$$s' = \sqrt{\frac{\omega \rho_0 a^2}{\eta_f}}, \tag{16}$$

with $2a$ the length of the slit.

The effective density for both the cylindrical pore and the slit is shown as a function of s and s', respectively, in Figure 1. The behaviour of both curves is similar. The viscous skin depth δ is given by

$$\delta = \sqrt{\frac{2\eta_f}{\omega \rho_0}} \tag{17}$$

and is approximately equal to the thickness of the layer of air where the velocity distribution is influenced by the viscous interaction with the rigid wall of the pore. At low frequencies, the effect of viscous forces is important everywhere in the pore. As the viscous skin depth decreases with frequency, viscosity effects become more and more negligible in the central part of the pore. Figure 1 clearly shows that the imaginary part of the effective density approaches zero for large values of s and s' and the real part tends to ρ_0.

Similarly, the thermal skin depth δ' is defined as:

$$\delta' = \sqrt{\frac{2\eta_f}{\omega Pr \rho_0}}, \tag{18}$$

also decreasing with frequency. The bulk modulus K of air in a cylindrical pore and a slit is shown as a function of s and s' in Figure 2. The real part equals P_0 at low frequencies, being the isothermal asymptote and evolves towards γP_0 as the high frequency limit, representing the adiabatic asymptote. These expressions for $K(\omega)$ and $\rho(\omega)$ can be directly used in an equivalent fluid model, using formulas (3)-(4).

Similarly, analytical models can be derived for porous materials with other simple pore morphologies. Stinson [31] generalised the theory for cross sections of arbitrary shape and applied it to rectangular tubes and equilateral triangles.

It can be concluded that $\rho(\omega)$ and $K(\omega)$ can be written in terms of a frequency- and shape-dependent function $F(\omega)$:

$$\rho = \frac{\rho_0}{F(\omega)}, \tag{19}$$

$$K = \frac{\gamma P_0}{\gamma - (\gamma - 1) F(\omega Pr)}. \tag{20}$$

When considering more than one pore, the flow resistivity σ in combination with the porosity ϕ can be used to eliminate R_0 and a in the expressions of s and s' respectively. For a material with n cylindrical pores with radius R_0 perpendicular to the surface per unit area of surface, the porosity ϕ simply equals $n\pi R_0^2$. It can be shown by simple calculus that the flow resistivity reads

$$\sigma = \frac{8\eta_f}{R_0^2 \phi}, \tag{21}$$

leading to

$$s = \sqrt{\frac{8\omega\rho_0}{\sigma\phi}}. \tag{22}$$

Taking into account this expression of s, the following definitions of the effective density and bulk modulus are

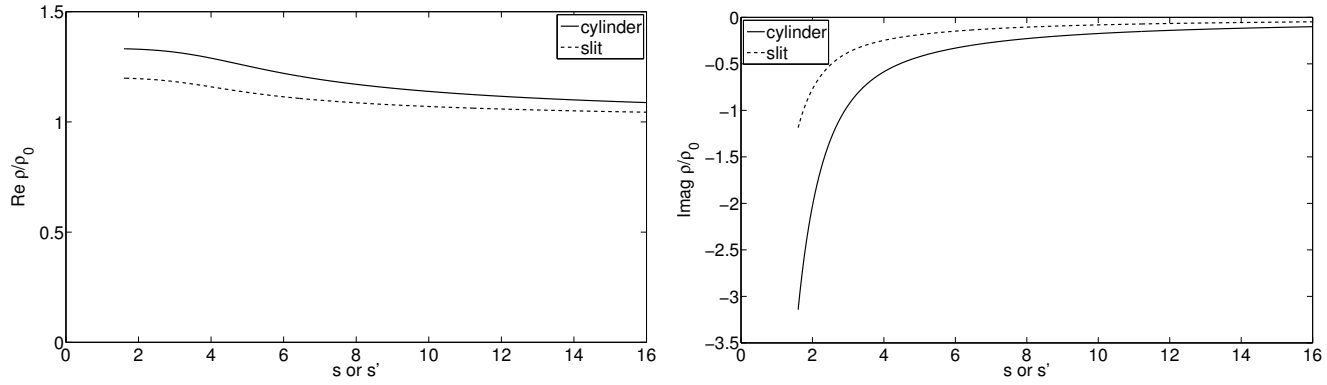

(a) real part of ρ/ρ_0 (b) imaginary part of ρ/ρ_0

Fig. 1 Ratio of the effective density of a fluid in a cylindrical pore and a slit, and the density in free air, ρ/ρ_0 as a function of s or s' respectively.

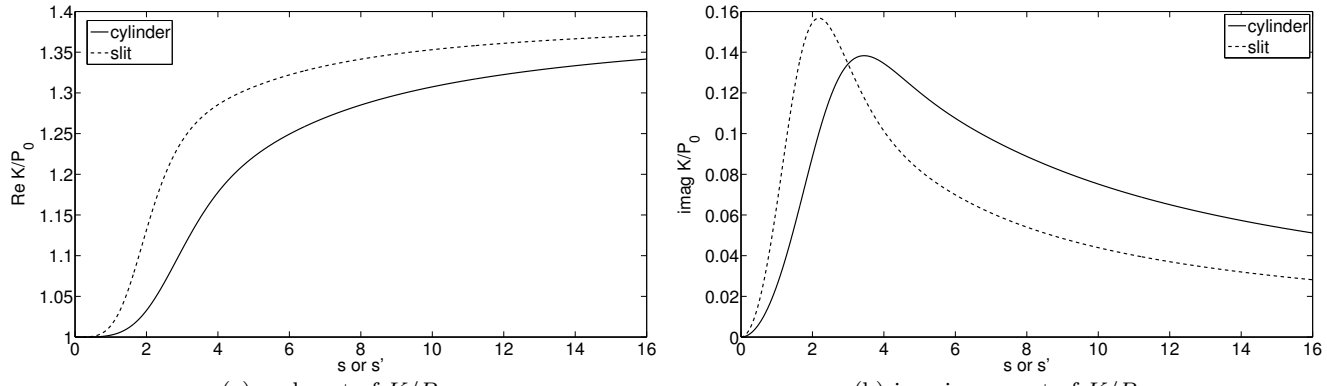

(a) real part of K/P_0 (b) imaginary part of K/P_0

Fig. 2 Ratio of the bulk modulus in air in a cylindrical pore and a slit, and the atmospheric pressure P_0, as a function of s or s' respectively.

found:

$$\rho = \rho_0 \left(1 + \frac{\sigma\phi}{j\omega\rho_0} G_c(s)\right), \tag{23}$$

$$K = \frac{\gamma P_0}{\gamma - (\gamma-1)F(\omega Pr)}, \tag{24}$$

where the subscript c indicates cylindrical pores and

$$F(\omega Pr) = \frac{1}{1 + \frac{\sigma\phi}{jPr\omega\rho_0} G_c(s\sqrt{Pr})}, \tag{25}$$

$$G_c(s) = \frac{-s\sqrt{-j}}{4} \frac{\frac{J_1(s\sqrt{-j})}{J_0(s\sqrt{-j})}}{1 - \frac{2}{s\sqrt{-j}} \frac{J_1(s\sqrt{-j})}{J_0(s\sqrt{-j})}}. \tag{26}$$

For a slit, a similar reasoning can be followed [23]:

$$\sigma = \frac{3\eta}{\phi a^2}, \tag{27}$$

leading to

$$s' = \sqrt{\frac{3\omega\rho_0}{\sigma\phi}}. \tag{28}$$

Expressions for $\rho(\omega)$ and $K(\omega)$ can be given, similarly to expressions (23)-(24), using $G_s(s')$ instead of $G_c(s)$, where the subscript s indicates that the pores have a slit-shape:

$$G_s(s') = \frac{\sqrt{j}s' \tanh(s'\sqrt{j})}{3\left(1 - \frac{\tanh(s'\sqrt{j})}{s'\sqrt{j}}\right)}. \tag{29}$$

As pointed out by Biot [32], it can be shown that G_s and G_c have a very similar shape if s is replaced by $4/3s'$. Consequently, G_c can be used to evaluate the effective density and bulk modulus of rigid frame porous material for pores of an arbitrary cross section if the definition of s is altered:

$$s = c\sqrt{\frac{8\omega\rho_0}{\sigma\phi}}, \tag{30}$$

where c is a shape factor depending on the cross section of the straight pores [23,33].

When considering straight pores, all inclined with an angle θ to the surface, the porosity is increased by a factor $\frac{1}{\cos\theta}$. Taking into account this increase in porosity together with the longer distance acoustic waves have to travel through the porous material, the flow

resistivity is increased by $\frac{1}{\cos^2\theta}$. This quantity is called the tortuosity α_∞, and will be generalised further on. In earlier works the tortuosity is also referred to as the structure form factor k_s [24]. By using the tortuosity for straight, oblique pores, s reads:

$$s = c\sqrt{\frac{8\omega\rho_0\alpha_\infty}{\sigma\phi}}, \tag{31}$$

and of course also the effective density is increased:

$$\rho = \alpha_\infty\rho_0\left(1 + \frac{\sigma\phi}{j\omega\alpha_\infty\rho_0}G_c(s)\right), \tag{32}$$

accounting for the fact that the fluid moves with a greater speed on the microscopic scale than on the macroscopic scale of propagation. Expression (24) still holds, but $F(\omega Pr)$ is given by:

$$F(\omega Pr) = \frac{1}{1 + \frac{\sigma\phi}{j\omega\rho_0\alpha_\infty Pr}G_c\sqrt{Pr}s}. \tag{33}$$

As a conclusion, when considering geometrically simple pores such as cylinders or slits perpendicular or inclined with a certain angle to the surface and assuming propagation along the direction of the pores, viscous and thermal effects can be analytically calculated and taken into account. Viscous losses are accounted for within the effective density $\rho(\omega)$, whereas thermal losses are included in the effective bulk modulus $K(\omega)$. At low frequencies, viscous forces are more important. The effective density $\rho(\omega)$ takes into account the transition to inviscid flow as high frequency asymptote. The frequency dependent effective bulk modulus $K(\omega)$ takes into account the transition from isothermal behaviour as low frequency limit to adiabatic behaviour as high frequency limit.

2.1.3 Semi-phenomenological models

The pore geometry of a porous material is in general highly complicated. As such, it is not possible to straightforwardly calculate the viscous and thermal interactions between the fluid in the pores and the skeleton material.

For common porous materials, due to the complex microstructure, mostly phenomenological models are being applied, using the same mechanisms as the analytical models mentioned above. Attenborough [34] stressed the importance of tortuosity and proposed the use of two shape factors, validated for granular media. A substantial improvement was, however, made by Johnson et al. [35] who introduced the concept of dynamic tortuosity to account for the frequency-dependent viscous effects in the pores. To take into account the complexity of the pore shape, the concept of the viscous characteristic length Λ was introduced. In a similar fashion, a thermal characteristic length Λ' has been introduced by Champoux and Allard [36] in order to better account for the thermal effects. Although further improvements have been made, the so-called Johnson-Champoux-Allard model is the most commonly used theory today and is discussed here.

Johnson et al. [35] define the concept of tortuosity. When a porous solid frame is filled with a non-viscous fluid, the effective density of the fluid is determined by the tortuosity:

$$\rho = \rho_0\alpha_\infty, \tag{34}$$

being an intrinsic parameter of the poroelastic frame, depending on the complex microstructure. The tortuosity takes into account the actual distance the acoustic waves have to propagate in the microstructure due to the curvature of the pores through a layer to the thickness of the layer. Whereas it can be directly calculated for simple pore geometries as explained in Section 2.1.2, this is obviously not possible for a complex microstructure. Most often the tortuosity is obtained via measurements, but can also be retrieved by doing simulations on actual microstructures [37,38]. According to the Johnson-Champoux-Allard model the fluid density can be written as:

$$\rho_f(\omega) = \rho_0\alpha(\omega), \tag{35}$$

with $\alpha(\omega)$, the dynamic tortuosity; a function to take into account the frequency-dependent viscous effects [35]. The viscous interaction between air and the pore walls is known exactly at the low and the high frequency asymptote. In the intermediate frequency regime a simple analytical function is used to approximate the viscous interaction:

$$\alpha(\omega) = \alpha_\infty\left[1 + \frac{\sigma\phi}{j\omega\rho_0\alpha_\infty}G_J(\omega)\right], \tag{36}$$

where $G_J(\omega)$ is a relaxation function which takes into account the transition from microscale Stokes flow at very low frequencies to inviscid flow as high frequency asymptote:

$$G_J(\omega) = \sqrt{1 + \frac{4j\alpha_\infty^2\eta_f\rho_0\omega}{\sigma^2\Lambda^2\phi^2}}, \tag{37}$$

where Λ is the viscous characteristic length [35]. This transition is, for rigid cylindrical pores, determined by the pore radius and for slits determined by the length of the slit. The viscous characteristic length provides a characteristic dimension for arbitrary and more general microstructures and is defined as:

$$\Lambda = 2\frac{\int_V v_i^2(\mathbf{r})dV}{\int_A v_i^2(\mathbf{r_w})dA}. \tag{38}$$

The integral in the denominator is performed over the pore surfaces A of a representative volume of material, $v_i(\mathbf{r_w})$ is the velocity of the fluid on the pore surface, the integral in the numerator is performed over the pore volume V and the velocity $v_i(\mathbf{r})$ is the velocity inside the pores. Smaller sections contribute to a larger extent to Λ since velocity gradients are higher as compared to larger sections [39].

In a similar way as for viscous effects, a function $\alpha'(\omega)$ can be used [40] to take into account thermal effects:

$$K(\omega) = \frac{\gamma P_0}{\gamma - (\gamma-1)(\alpha'(\omega))^{-1}}. \tag{39}$$

Again, the thermal interaction is known exactly at low and high frequencies. Champoux and Allard [36] have shown that the equivalent bulk modulus is controlled by different aspects of the pore geometry, introducing the thermal characteristic length Λ'. Following their approach, $\alpha'(\omega)$ is given by:

$$\alpha'(\omega) = 1 + \frac{8\eta_f}{j\Lambda'^2 Pr\omega\rho_0}\sqrt{1 + j\rho_0\frac{\omega Pr\Lambda'^2}{16\eta_f}}, \tag{40}$$

The thermal characteristic length is defined as:

$$\Lambda' = 2\frac{\int_V dV}{\int_A dA}, \tag{41}$$

being twice the ratio of the pore volume to the pore surface. Since no weighting is applied, the thermal characteristic length will be larger than or equal to the viscous characteristic length. Larger pore sections contribute more to Λ' than smaller pore sections. Similarly as for tortuosity, the characteristic lengths of a porous material are mostly obtained by dedicated measurements, but can also be obtained by performing detailed simulations on the real microstructure, e.g. see [41].

Using this model, the poroelastic material can be described as an equivalent fluid, for which thermal and viscous effects are accounted for. The semi-phenomenological models only hold when the wavelengths are much larger than the pore size and have been validated using homogenisation theory and a separation of scales, see e.g. [42].

Besides the Johnson-Champoux-Allard model using 5 parameters, Wilson [43] proposes to describe the viscous and thermal dissipation using relaxation processes. The model focuses on matching the intermediate frequencies and does not fit the asymptotic behaviour at low and high frequencies. The advantage with respect to the previous formulations is that the expressions are simpler and that one less parameter is required.

Also more advanced expressions with respect to the Johnson-Champoux-Allard model can be found, which take into account more parameters. Lafarge et al. [40] indicate a lack of information at low frequencies for thermal effects. Only 2 parameters (ϕ,Λ') are used in the Johnson-Champoux-Allard model to describe the dynamic bulk modulus, whereas four parameters are required to calculate the effective density (Λ,ϕ,α_∞,σ). They introduce a new parameter, k_0', the static thermal permeability, to better describe thermal effects in the low frequency range.

However, the real part of the dynamic density is still not correct if ω tends to zero. A similar reasoning holds for the dynamic bulk modulus. Pride et al. [44] proposed a modified expression of the dynamic density which was further improved by Lafarge [45]. The static viscous tortuosity α_0 is introduced and it was shown that $\alpha_0 \geq \alpha_\infty$. In a similar fashion the static thermal tortuosity α_0' is introduced to correct the effective bulk modulus if ω tends to zero [40]. Those extended models are, however, rarely used, as the new parameters should be characterised, also requiring new developments on the measurement side.

A comparison between a number of models can for instance be found in [23,46,47].

2.1.4 Limp model

Beside equivalent fluid models which describe the dynamic behaviour of the materials when the frame if supposed to be motionless, also the assumption of a limp frame can be made. This means that the frame does not resist to external excitations, which occur for poroelastic media when the elasticity of the frame can be neglected. Similarly to equivalent fluid models, only one compressional wave type is accounted for. The resulting governing equation can be obtained starting from the Biot equations, which are explained in section 2.2, and neglecting the stress tensor of the solid phase in vacuum [23,48]. By combining the two resulting equations, one obtains:

$$\nabla^2 p^l(\mathbf{r}) + \frac{\rho_{limp}}{K_{eq}}\omega^2 p^l(\mathbf{r}) = 0, \tag{42}$$

which is again a Hemholtz equation. The superscript l indicates that a limp model is considered, and the limp effective density ρ_{limp} takes into account the inertia of the frame:

$$\rho_{limp} = \frac{\tilde{\rho}\rho_{eq}}{\tilde{\rho} + \rho_{eq}\tilde{\gamma}^2}. \tag{43}$$

Expressions for $\tilde{\rho}$ and $\tilde{\gamma}$ are given in Section 3.1.4. The difference between the equivalent fluid and the limp model is mainly important at low frequencies, as illustrated in [48]. An important difference is that the equivalent fluid model does not allow for rigid body

motion of the material, whereas the limp model does. Generally, rigid frame material models should not be used when the material is bonded to a vibrating structure. The limp material model can be used in this case, if the bulk modulus of the fluid is much higher than the bulk modulus of the frame in vacuum.

Doutres et al. [49] propose the frame stiffness influence (FSI) as a criterion to identify porous materials for which the limp model can be used. The FSI is frequency dependent and expresses the the influence of the frameborne wave on the fluid phase displacement. For two cases, aborsorption of a poroelastic layer attached to a rigid backing and a sound radiation of a vibrating plate with a poroelastic layer, critical values FSI are derived, showing that the limp model can be used for certain cases. Since only 1D simulations are considered, the shear wave is not considered. The authors, however, state that it seems realistic that the same criteria apply to three-dimensional problems where the shear wave is not mainly excited. The FSI criterion confirms that the use of a limp model is less restrictive than the rigid frame one.

2.1.5 Double porosity materials with a rigid frame

Other developments, which are not detailed here, include double porosity materials [50,51]. Double porosity models are semi-phenomenological models accounting for media with two networks of pores of very different sizes. In this specific case three scales are considered: (i) the macroscopic scale of wave propagation, (ii) the pores at the mesoscopic scale and (iii) the pores in the frame material on the microscopic scale. By using the homogenisation method for periodic structures and using a separation of scales, it has been shown theoretically that the absorption coefficient of poroelastic materials with a high flow resistivity can be increased compared to a single porosity material for a wide frequency range. Double porosity materials with a rigid frame can be represented as an equivalent fluid with effective density ρ_{dp} and effective bulk modulus K_{dp}, where the subscript dp indicates double porosity quantities. Those macroscopic quantities depend on the static permeability contrast between the micropores and the pores at the mesoscopic scale and two regimes are represented: the low and the high permeability contrast [51]. Atalla et al. [52] confirmed the results of Olny et al. and validated the influence of several design parameters on the absorption coefficient. The work by Sgard et al. [53] gives a nice summary of the developed theories and provides design rules to obtain the best noise reduction using perforations.

2.1.6 Boundary and coupling conditions

Since the Helmholtz equation (1) is a second order partial differential equation, one boundary condition needs to be specified on each point of the boundary of the domain to obtain a well-posed problem. Similar boundary conditions as for purely acoustic problems can be applied, however, taking into account the porosity, included in $\rho_{eq}(\omega)$ and $K_{eq}(\omega)$. Typical boundary conditions and coupling conditions to an acoustic cavity can be found, for instance, in [54]. The boundary Γ^{eq} can be subdivided into non-overlapping parts: $\Gamma^{eq} = \Gamma_v^{eq} \cup \Gamma_p^{eq} \cup \Gamma_Z^{eq} \cup \Gamma_C^{eqa} \cup \Gamma_C^{eqeq}$. On the three first parts, the following residuals apply:

$$\mathbf{r} \in \Gamma_v^{eq} : \; R_v^{eq} = \mathcal{L}_v^{eq}(p^{eq}(\mathbf{r})) - \overline{v}_n(\mathbf{r}) = 0, \tag{44}$$

$$\mathbf{r} \in \Gamma_p^{eq} : \; R_p^{eq} = p^{eq}(\mathbf{r}) - \overline{p}(\mathbf{r}) = 0, \tag{45}$$

$$\mathbf{r} \in \Gamma_Z^{eq} : \; R_Z^{eq} = \mathcal{L}_v^{eq}(p^{eq}(\mathbf{r})) - \frac{p^{eq}(\mathbf{r})}{\overline{Z}_n(\mathbf{r})} = 0, \tag{46}$$

where the quantities $\overline{v}_n$, $\overline{p}$ and $\overline{Z}_n$ are, respectively, the imposed normal velocity, pressure and normal impedance. The velocity operator $\mathcal{L}_v^{eq}(\bullet)$ is defined as:

$$\mathcal{L}_v^{eq}(\bullet) = \frac{j}{\rho_{eq}\omega} \frac{\partial \bullet}{\partial \mathbf{n}}, \tag{47}$$

where $\mathbf{n}$ is the local normal on the boundary, pointing outwards.

On the interface Γ_C^{eqa} between an equivalent fluid and an acoustic domain, the following residuals are applied:

$$\mathbf{r} \in \Gamma_C^{eqa} : \begin{cases} R_p^{eqa}(\mathbf{r}) = p^a(\mathbf{r}) - p^{eq}(\mathbf{r}) = 0, \\ R_{v_n}^{eqa}(\mathbf{r}) = \mathcal{L}_v(p^a(\mathbf{r})) \\ \qquad\qquad + \mathcal{L}_v^{eq}(p^{eq}(\mathbf{r})) = 0. \end{cases} \tag{48}$$

The first equation indicates the equilibrium between the pressure in the acoustic and the poroelastic domain. The second equation describes the continuity of acoustic velocity, taking into account the porosity.

On the interface Γ_C^{eqeq} between two equivalent fluid domains with different material properties, indicated by superscripts $eq1$ and $eq2$, the following coupling conditions hold:

$$\mathbf{r} \in \Gamma_C^{eqeq} : \begin{cases} R_p^{eqeq}(\mathbf{r}) = p^{eq1}(\mathbf{r}) - p^{eq2}(\mathbf{r}) = 0, \\ R_{v_n}^{eqeq}(\mathbf{r}) = \mathcal{L}_v^{eq1}\left(p^{eq1}(\mathbf{r})\right) \\ \qquad\qquad + \mathcal{L}_v^{eq2}\left(p^{eq2}(\mathbf{r})\right) = 0. \end{cases} \tag{49}$$

The first equation takes into account the equilibrium of forces. The second one imposes the continuity of acoustic velocity and takes into account the porosity of both media.

2.2 Theory by Biot

When the solid phase is not considered to be rigid or limp, but elastic, the vibrations of the frame and the mutual interaction between both phases also need to be accounted for. The Biot theory [25,32,55], as adopted by Johnson et al. [35], Champoux and Allard [36], and as is presented in [23], is most commonly used to model the fully coupled dynamic behaviour of poroelastic materials. This theory predicts the existence of three different types of coupled propagating waves: one shear wave and two compressional waves. The Biot theory applies a homogenised solid and a compressible fluid continuum description on a macroscopic level. This is justified in the case when the characteristic dimensions of the material, e.g. the pore sizes, are small as compared to characteristic dimensions on the macroscopic level, typically the wavelengths of the different types of waves which propagate through the material [56,57]. The interaction between both phases is described using coupling parameters which are derived from measurable macroscopic properties. Fluid-structure interaction occurs throughout the whole material, and the different waves can be strongly coupled.

According to the Biot theory, the momentum equations can be written as:

$$\begin{aligned}\nabla \cdot \boldsymbol{\sigma^s}(\mathbf{r}) = &-\omega^2 \rho_1 \mathbf{u^s}(\mathbf{r}) \\ &-(\omega^2 \rho_a - j\omega b(\omega))(\mathbf{u^s}(\mathbf{r}) - \mathbf{u^f}(\mathbf{r})),\end{aligned} \tag{50}$$

$$\begin{aligned}\nabla \cdot \boldsymbol{\sigma^f}(\mathbf{r}) = &-\omega^2 \rho_2 \mathbf{u^f}(\mathbf{r}) \\ &-(\omega^2 \rho_a - j\omega b(\omega))(\mathbf{u^f}(\mathbf{r}) - \mathbf{u^s}(\mathbf{r})),\end{aligned} \tag{51}$$

with $\boldsymbol{\sigma}^\bullet(\mathbf{r})$ the partial stress tensor and $\mathbf{u}^\bullet(\mathbf{r})$ the displacement vector of phase $\bullet$. The partial stress tensor of the solid phase $\boldsymbol{\sigma^s}(\mathbf{r})$ is symmetric and gathers the stress components acting on the solid part of the poroelastic material and is denoted as:

$$\boldsymbol{\sigma^s}(\mathbf{r}) = \begin{bmatrix} \sigma^s_{xx}(\mathbf{r}) & \sigma^s_{xy}(\mathbf{r}) & \sigma^s_{xz}(\mathbf{r}) \\ \sigma^s_{yx}(\mathbf{r}) & \sigma^s_{yy}(\mathbf{r}) & \sigma^s_{yz}(\mathbf{r}) \\ \sigma^s_{zx}(\mathbf{r}) & \sigma^s_{zy}(\mathbf{r}) & \sigma^s_{zz}(\mathbf{r}) \end{bmatrix}. \tag{52}$$

The partial stress tensor of the fluid phase $\boldsymbol{\sigma^f}(\mathbf{r})$ contains the stress components acting on the fluid part:

$$\boldsymbol{\sigma^f}(\mathbf{r}) = \begin{bmatrix} \sigma^f(\mathbf{r}) & 0 & 0 \\ 0 & \sigma^f(\mathbf{r}) & 0 \\ 0 & 0 & \sigma^f(\mathbf{r}) \end{bmatrix}, \tag{53}$$

with the scalar $\sigma^f(\mathbf{r})$ proportional to the hydrostatic fluid pore pressure $p^f(\mathbf{r})$:

$$\sigma^f(\mathbf{r}) = -\phi p^f(\mathbf{r}). \tag{54}$$

The first term in the right hand side of equation (50) takes into account the inertia of the solid frame. The density $\rho_1 = (1-\phi)\rho_s$ is the bulk density of the solid phase. The second term in the right hand side depends on the relative motion between the solid and the fluid phase and contains two dynamic coupling effects. Due to the viscosity of the fluid, viscous drag forces are generated between the fluid and the solid phase when both phases move with a relative velocity with respect to each other. The frequency dependent viscous drag $b(\omega)$ accounts for this effect and is given by [35]:

$$b(\omega) = \sigma\phi^2 G_J(\omega). \tag{55}$$

Secondly, due to the complex pore geometry, inertial interactions occur between the two vibrating phases, which can be taken into account by introducing an inertial coupling term ρ_a, which depends on the porosity and the tortuosity:

$$\rho_a = \phi\rho_0(\alpha_\infty - 1). \tag{56}$$

Similarly, the first term in the right hand side of equation (51), with $\rho_2 = \phi\rho_0$ the bulk density of the fluid phase, takes into account the inertia of the fluid phase. Due to the principle of action and reaction, the same viscous and inertial interactions apply as in equation (50), but with an opposite sign.

The constitutive relations are:

$$\boldsymbol{\sigma^s}(\mathbf{r}) = [A(\omega)e^s(\mathbf{r}) + Q(\omega)e^f(\mathbf{r})]\mathbf{I} + 2N\mathbf{e^s}(\mathbf{r}), \tag{57}$$

$$\boldsymbol{\sigma^f}(\mathbf{r}) = [Q(\omega)e^s(\mathbf{r}) + R(\omega)e^f(\mathbf{r})]\mathbf{I}, \tag{58}$$

where $\mathbf{I}$ is the identity matrix, $e^\bullet(\mathbf{r})$ is the volumetric strain of phase $\bullet$, also known as dilatation:

$$e^\bullet(\mathbf{r}) = \nabla \cdot \mathbf{u}^\bullet = \frac{\partial u^\bullet_x}{\partial x} + \frac{\partial u^\bullet_y}{\partial y} + \frac{\partial u^\bullet_z}{\partial z}, \tag{59}$$

and $\mathbf{e^s}(\mathbf{r})$ is the symmetric strain tensor of the solid phase:

$$\begin{aligned}\mathbf{e^s}(\mathbf{r}) &= \begin{bmatrix} e^s_{xx} & e^s_{xy} & e^s_{xz} \\ e^s_{yx} & e^s_{yy} & e^s_{yz} \\ e^s_{zx} & e^s_{zy} & e^s_{zz} \end{bmatrix} \\ &= \begin{bmatrix} \frac{\partial u^s_x}{\partial x} & \frac{1}{2}\left(\frac{\partial u^s_y}{\partial x} + \frac{\partial u^s_x}{\partial y}\right) & \frac{1}{2}\left(\frac{\partial u^s_z}{\partial x} + \frac{\partial u^s_x}{\partial z}\right) \\ \frac{1}{2}\left(\frac{\partial u^s_x}{\partial y} + \frac{\partial u^s_y}{\partial x}\right) & \frac{\partial u^s_y}{\partial y} & \frac{1}{2}\left(\frac{\partial u^s_z}{\partial y} + \frac{\partial u^s_y}{\partial z}\right) \\ \frac{1}{2}\left(\frac{\partial u^s_x}{\partial z} + \frac{\partial u^s_z}{\partial x}\right) & \frac{1}{2}\left(\frac{\partial u^s_y}{\partial z} + \frac{\partial u^s_z}{\partial y}\right) & \frac{\partial u^s_z}{\partial z} \end{bmatrix}.\end{aligned} \tag{60}$$

The parameter N is the second Lamé coefficient of the solid frame, $Q(\omega)$ is a dilatational coupling factor describing fluid stress dependence on frame dilatation and conversely frame stress dependence on fluid dilatation and $R(\omega)$ can be interpreted as the fluid phase bulk stiffness at zero frame dilatation. Expressions for the

elastic constants N, $R(\omega)$, $Q(\omega)$ and $A(\omega)$ can be found by using Biot's '*gedanken experiments*' [58]. Four independent measurements in three tests are specified to obtain these constants, and the dependence of the different parameters on the angular frequency is omitted for the remainder of the text for the sake of clarity:

1. Jacketed compressibility test: the poroelastic specimen is inserted in an impermeable, flexible jacket, which is subjected to a hydrostatic pressure p'. The pressure inside the jacket remains constant during the test. The pressure p' is transmitted to the solid portions of the surface and $\sigma^s_{xx} = \sigma^s_{yy} = \sigma^s_{zz} = -p'$. The dilatation of the solid phase is measured and the bulk modulus K_b of the frame material at constant pressure in air reads:

$$K_b = -\frac{p'}{e^s}. \tag{61}$$

   Often, K_b is referred to as the bulk modulus of the frame *in vacuo*. The pore pressure remains constant, leading to $\sigma^f = 0N/m^2$. By using equations (57)-(58), and eliminating p' and e^f one finds the following relation:

$$K_b = \frac{2}{3}N + A - \frac{Q^2}{R}. \tag{62}$$

   indicating that $A - \frac{Q^2}{R}$ is the first Lamé coefficient λ of the poroelastic material at constant pore pressure.
2. Unjacketed compressibility test: the poroelastic specimen is open and is subjected to an increase of pressure in the air p'. In this case the pressure p' acts on both the solid and the fluid phase: $\sigma^s_{xx} = \sigma^s_{yy} = \sigma^s_{zz} = -(1-\phi)p'$ and $\sigma^f_{xx} = -\phi p'$. Two bulk moduli are defined:

$$K_s = \frac{-p'}{e^s}, \tag{63}$$

$$K_f = \frac{-p'}{e^f}, \tag{64}$$

   where K_s is the bulk modulus of the elastic solid from which the frame is made and K_f is the bulk modulus of the air. By substituting these expressions and the values for the stresses into (57)-(58) and eliminating p', e^s and e^f and using equation (62) leads to the three following expressions:

$$\phi\left(\frac{Q+R}{R}\right) = 1 - \frac{K_b}{K_s}, \tag{65}$$

$$\frac{Q}{K_s} + \frac{R}{K_f} = \phi. \tag{66}$$

3. Pure shear test: If the material is subjected to a pure shear loading, e^s and e^f are zero and we obtain:

$$\sigma^s_{ij} = 2Ne^s_{ij}, \tag{67}$$

$$\sigma^f = 0, \tag{68}$$

   indicating that N is the shear modulus of the material and also the shear modulus of the frame since the air does not contribute to the shear restoring force.

By combining equations (62), (65) and (66), expressions for A, Q and R are obtained in function of measurable quantities:

$$A = \frac{(1-\phi)\left(1-\phi-\frac{K_b}{K_s}\right)K_s + \phi\frac{K_bK_s}{K_f}}{1-\phi-\frac{K_b}{K_s}+\phi\frac{K_s}{K_f}} - \frac{2}{3}N, \tag{69}$$

$$Q = \frac{\left(1-\phi-\frac{K_b}{K_s}\right)\phi K_s}{1-\phi-\frac{K_b}{K_s}+\phi\frac{K_s}{K_f}}, \tag{70}$$

$$R = \frac{\phi^2 K_s}{1-\phi-\frac{K_b}{K_s}+\phi\frac{K_s}{K_f}}. \tag{71}$$

For typical poroelastic materials used in acoustic applications, the bulk modulus of the elastic solid from which the frame is made K_s is very large as compared to the bulk modulus of the porous material *in vacuo* K_b and the bulk modulus of the fluid in the pores K_f. In that case, the solid material can be treated as incompressible and the expressions of the elastic constants reduce to:

$$A = \lambda + \frac{(1-\phi)^2}{\phi}K_f, \tag{72}$$

$$Q = (1-\phi)K_f, \tag{73}$$

$$R = \phi K_f, \tag{74}$$

with $\lambda = \frac{E\nu}{(1+\nu)(1-2\nu)}$ the first Lamé coefficient of the solid phase material and $E = E_s(1+j\eta_l)$ the *in vacuo* modulus of elasticity of the bulk solid phase, ν the Poisson coefficient and η_l the loss factor to take into account internal frictional losses. Taking into account the Johnson-Champoux-Allard theory, the expression of $K(\omega)$ (39) can be used to evaluate the bulk modulus of the fluid in the pores K_f. The subscript f has been added in this section to make a clear distinction between the different bulk moduli.

Other ways to include structural damping are also being applied, such as for instance the augmented Hooke's law [59–61]. The Lamé coefficients are then augmented with complex and frequency dependent damping functions which take into account relaxation processes.

The substitution of the constitutive relations (57)-(58) into the momentum equations (50)-(51) leads to

the Biot equations:

$$N\nabla^2\mathbf{u^s}(\mathbf{r}) + \nabla[(\lambda + \frac{Q^2}{R} + N)e^s(\mathbf{r}) + Qe^f(\mathbf{r})] = -\omega^2(\tilde{\rho}_{11}\mathbf{u^s}(\mathbf{r}) + \tilde{\rho}_{12}\mathbf{u^f}(\mathbf{r})), \quad (75)$$

$$\nabla[Qe^s(\mathbf{r}) + Re^f(\mathbf{r})] = -\omega^2(\tilde{\rho}_{12}\mathbf{u^s}(\mathbf{r}) + \tilde{\rho}_{22}\mathbf{u^f}(\mathbf{r})), \quad (76)$$

where $\tilde{\rho}_{11} = \rho_1 + \rho_a + b/j\omega$, $\tilde{\rho}_{12} = -\rho_a - b/j\omega$ and $\tilde{\rho}_{22} = \rho_2 + \rho_a + b/j\omega$ [23]. The complex and frequency dependent densities $\tilde{\rho}_{11}$, $\tilde{\rho}_{22}$ and $\tilde{\rho}_{12}$ take into account the total viscous and inertial energy dissipation caused by the relative motion between the solid and the fluid phase. The Biot equations (75)-(76) are expressed in terms of the solid and the fluid displacement components but other formulations exist. Some of them are discussed in Section 3.1. As predicted by the Biot theory, three different wave types can exist in poroelastic materials: two compressional wave types and one shear wave type. The wave numbers k_{l_1} and k_{l_2} associated with the compressional waves are given by [23]:

$$\begin{cases} k_{l_1} = \sqrt{\frac{A_1}{2} - \sqrt{\frac{A_1^2}{4} - A_2}} \\ k_{l_2} = \sqrt{\frac{A_1}{2} + \sqrt{\frac{A_1^2}{4} - A_2}} \end{cases}, \quad (77)$$

$$\text{with} \quad \begin{cases} A_1 = \omega^2 \frac{\tilde{\rho}_{11}R - 2\tilde{\rho}_{12}Q + \tilde{\rho}_{22}P}{RP - Q^2} \\ A_2 = \omega^4 \frac{\tilde{\rho}_{11}\tilde{\rho}_{22} - \tilde{\rho}_{12}^2}{RP - Q^2} \end{cases},$$

where $P = A + 2N$. The wave number associated with the shear wave is given by [23]:

$$k_t = \omega\sqrt{\frac{\tilde{\rho}_{11}\tilde{\rho}_{22} - \tilde{\rho}_{12}^2}{N\tilde{\rho}_{22}}}. \quad (78)$$

Each of the three waves propagates in the solid as well as in the fluid phase of the poroelastic material. The ratios of the fluid over the solid velocities of the different wave types, μ_{l_1}, μ_{l_2} and μ_t, are given by [23]:

$$\mu_{l_1} = \frac{Pk_{l_1}^2 - \omega^2\tilde{\rho}_{11}}{\omega^2\tilde{\rho}_{12} - Qk_{l_1}^2}, \quad (79)$$

$$\mu_{l_2} = \frac{Pk_{l_2}^2 - \omega^2\tilde{\rho}_{11}}{\omega^2\tilde{\rho}_{12} - Qk_{l_2}^2}, \quad (80)$$

$$\mu_t = -\frac{\tilde{\rho}_{12}}{\tilde{\rho}_{22}}. \quad (81)$$

2.2.1 Example

For the vibro-acoustic applications considered in this review paper, the saturating fluid is air. The wave numbers are frequency dependent and complex, and can be very different from one material to another, due to the large variety of material properties. As an example, Figure 3 illustrates the physics of the different waves in a melamine foam as a function of the dimensionless frequency f/f_c. The material properties of the foam and air are given in Appendix A. The characteristic frequency f_c is given by [25]:

$$f_c = \frac{\phi\sigma}{2\pi\rho_0}, \quad (82)$$

and is for the considered melamine foam equal to 1240Hz. Whereas for this poroelastic material the interval $0.1f_c$-$10f_c$ well captures the transition zone from low to high frequency behaviour, this does not necessarily hold for all combinations of frames and fluids. A discussion is given in [62], including enhancements considering the effects of inertia and elasticity of the solid phase and momentum exchange.

The slow and fast compressional wave types are indicated by 'Compressional-S' and 'Compressional-F', respectively. Whenever applicable, the associated property for the equivalent fluid as described in Section 2.1.6, assuming a rigid frame, is also added to the figures. Similarly, curves associated to the compressional wave that would propagate in the frame in vacuum are added to the figures. The wave number of this compressional wave in vacuum is given by [23]:

$$k' = \omega\sqrt{\frac{\rho_1}{\lambda + 2N}}. \quad (83)$$

For low values of f/f_c, where the viscous forces are strong, it can be seen from Figure 3 that there is no relative motion between the solid and the fluid for the fast compressional wave and the shear wave. The modulus is close to one, and the phase difference between the solid and the fluid phase is close to zero. In addition, the fast compressional wave and the shear wave have a low attenuation coefficient in the low frequency range. The slow compressional wave, on the other hand, has a higher attenuation coefficient; the solid and the fluid phase move close to out of phase. The fluid velocity is higher than the solid velocity, as shown by the modulus.

For high dimensionless frequencies, the fast wave mainly propagates in the fluid phase as reflected by the high modulus, whereas the shear wave and the slow wave propagate in both phases, but with a higher contribution in the solid phase. As can be seen, the behaviour of the two compressional waves can be captured by the equivalent fluid model and the wave that propagates in the frame in vacuum. When both longitudinal waves are well decoupled, which may occur at higher frequencies, the terminology 'frame-borne' wave and 'airborne wave' is often used [23]. Note that the curve for the equivalent fluid consistently aligns with the wave with the highest contribution in the fluid

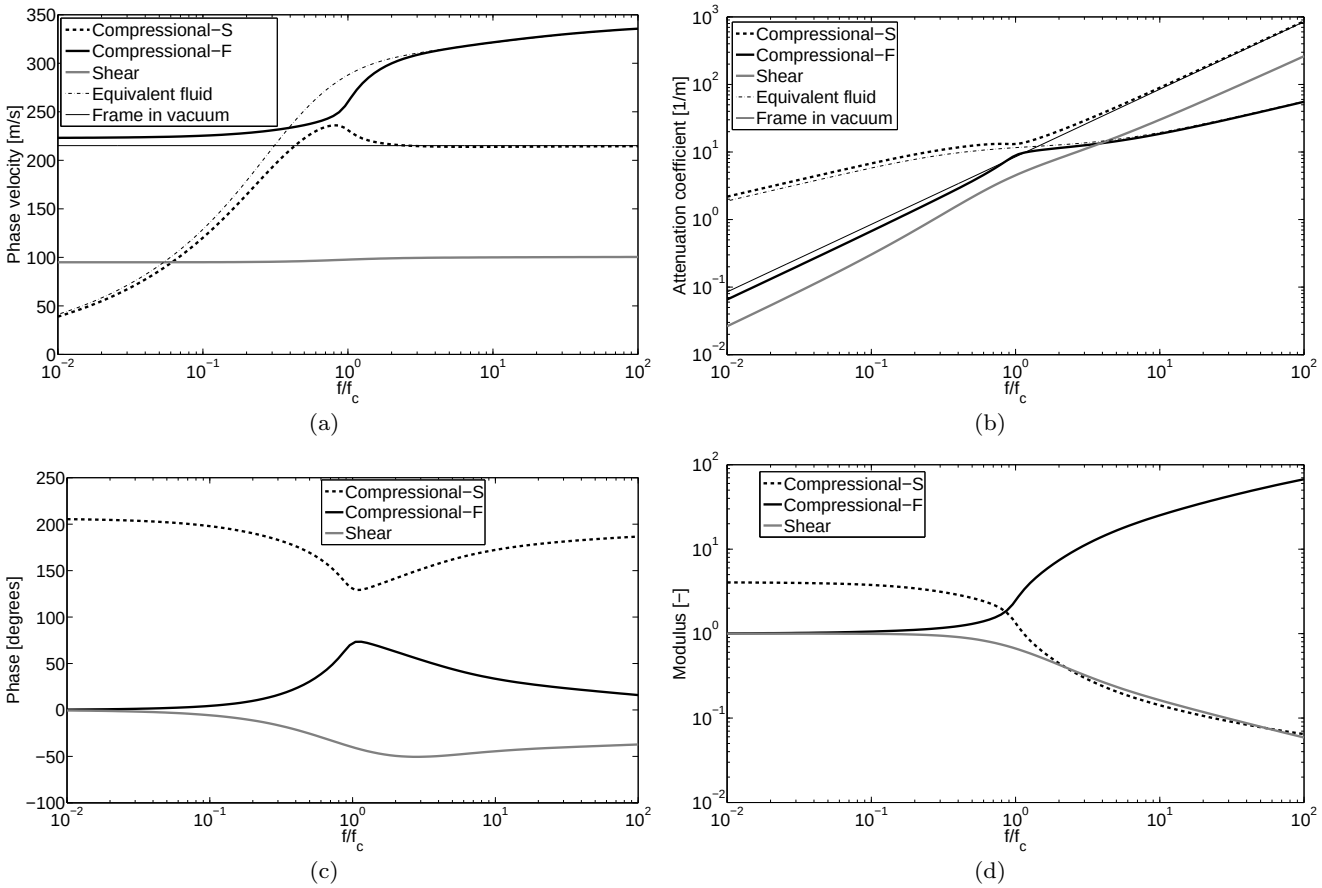

Fig. 3 (a) Phase velocity, (b) attenuation coefficient, (c) modulus and (d) phase of $\mu_\bullet$ of the slow compressional (Compressional-S), the fast compressional (Compressional-F) and the shear wave in a melamine foam as a function of the dimensionless frequency f/f_c. Where applicable, also the property associated with the equivalent fluid and the frame in vacuum is shown.

phase. At higher frequencies, when acoustic excitation is applied, the velocity of the frame will be negligible compared to the velocity of the air and the equivalent fluid model with a rigid frame can be used to represent the dynamic behaviour of the material.

2.2.2 Boundary and coupling conditions

For a poroelastic material, three boundary conditions have to be specified at each point of the boundary in order to have a well-posed problem. Three types of boundary conditions imposed on a poroelastic domain are considered here, as well as coupling conditions between two different poroelastic layers and coupling conditions between a poroelastic material and an acoustic domain. The boundary $\Gamma^p = \partial\Omega^p$ of a poroelastic domain Ω^p is can be subdivided into five non-overlapping parts: $\Gamma^p = \Gamma^p_{ki} \bigcup \Gamma^p_{me} \bigcup \Gamma^p_{mi} \bigcup \Gamma^{pa}_C \bigcup \Gamma^{pp}_C$. For a discussion on coupling conditions between a poroelastic medium and an elastic medium or a septum, and open and closed pores, the reader is referred to [63,64].

Boundary conditions For each kind of boundary, three residual error functions can be defined:

– kinematic boundary conditions along Γ^p_{ki}; the displacement components are prescribed:

$$\mathbf{r} \in \Gamma^p_{ki} : \begin{cases} R^p_{u^s_n}(\mathbf{r}) = u^s_n(\mathbf{r}) - \bar{u}^s_n(\mathbf{r}) = 0, \\ R^p_{u^s_s}(\mathbf{r}) = u^s_s(\mathbf{r}) - \bar{u}^s_s(\mathbf{r}) = 0, \\ R^p_{u^f_n}(\mathbf{r}) = u^f_n(\mathbf{r}) - \bar{u}^f_n(\mathbf{r}) = 0, \end{cases} \tag{84}$$

with $\bar{u}^s_n(\mathbf{r})$, $\bar{u}^s_s(\mathbf{r})$ and $\bar{u}^f_n(\mathbf{r})$ the prescribed values of the displacement components of the solid phase in the normal and tangential direction to the boundary and the prescribed value of the displacement of the fluid phase in the normal direction to the boundary, respectively. Using this type of boundary condition, fixed edges and imposed displacements (e.g. piston movement [65]) can be represented.

– mechanical boundary conditions along Γ_{me}; the stress resultants are prescribed:

$$\mathbf{r} \in \Gamma^p_{me} : \begin{cases} R^p_{\sigma^s_n}(\mathbf{r}) = \sigma^s_n(\mathbf{r}) - \bar{\sigma}^s_n(\mathbf{r}) = 0, \\ R^p_{\sigma^s_s}(\mathbf{r}) = \sigma^s_s(\mathbf{r}) - \bar{\sigma}^s_s(\mathbf{r}) = 0, \\ R^p_{\sigma^f}(\mathbf{r}) = \sigma^f(\mathbf{r}) - \bar{\sigma}^f(\mathbf{r}) = 0, \end{cases} \tag{85}$$

with $\bar{\sigma}^s_n(\mathbf{r})$, $\bar{\sigma}^s_s(\mathbf{r})$ and $\bar{\sigma}^f(\mathbf{r})$ the prescribed values of the stress resultant components of the solid phase in the normal and tangential direction to the boundary and the prescribed hydrodynamic stress of the fluid phase, respectively. Using this condition, for instance an imposed acoustic pressure can be accounted for.

– mixed boundary conditions along Γ^p_{mi}:

$$\mathbf{r} \in \Gamma^p_{mi} : \begin{cases} R^p_{u^s_n}(\mathbf{r}) = u^s_n(\mathbf{r}) - \bar{u}^s_n(\mathbf{r}) = 0, \\ R^p_{u^f_n}(\mathbf{r}) = u^f_n(\mathbf{r}) - \bar{u}^f_n(\mathbf{r}) = 0, \\ R^p_{\sigma^s_s}(\mathbf{r}) = \sigma^s_s(\mathbf{r}) - \bar{\sigma}^s_{ns}(\mathbf{r}) = 0. \end{cases} \tag{86}$$

For sliding edge boundary conditions [63] the prescribed values of $\bar{u}^s_n(\mathbf{r})$, $\bar{u}^f_n(\mathbf{r})$ and $\bar{\sigma}^s_s(\mathbf{r})$ are zero.

Coupling conditions Coupling conditions are conditions imposed between two different media. Coupling conditions between an acoustic cavity, in which the behaviour is governed by the acoustic Helmholtz equation and a poroelastic material and the coupling conditions between two different poroelastic domains are considered.

On the interface Γ^{pa}_C in between an acoustic and a poroelastic subdomain the four following coupling conditions are imposed:

$$\mathbf{r} \in \Gamma^{pa}_C : \begin{cases} R^{pa}_{\sigma^s_n}(\mathbf{r}) = \sigma^s_n(\mathbf{r}) + (1-\phi)p^a(\mathbf{r}) = 0, \\ R^{pa}_{\sigma^f}(\mathbf{r}) = \sigma^f(\mathbf{r}) + \phi p^a(\mathbf{r}) = 0, \\ R^{pa}_{\sigma^s_s}(\mathbf{r}) = \sigma^s_s(\mathbf{r}) = 0, \\ R^{pa}_{u}(\mathbf{r}) = \mathcal{L}_v(p^a(\mathbf{r})) \\ \quad - j\omega\left((1-\phi)u^s_n(\mathbf{r}) + \phi u^f_n(\mathbf{r})\right) = 0. \end{cases} \tag{87}$$

The first condition requires that the normal stress acting on the solid phase of the porous material is equal to $-(1-\phi)$ times the pressure $p^a(\mathbf{r})$ of the acoustic domain on the interface Γ^{pa}_C. The second equation gives a similar relation for the stress acting on the fluid phase of the poroelastic material. Consequently, the total normal stress $\sigma^t_n(\mathbf{r}) = \sigma^s_n(\mathbf{r}) + \sigma^f(\mathbf{r})$ equals $-p^a(\mathbf{r})$ on the interface. Since the air in the acoustic cavity is considered to be non viscous, the shear stress of the solid phase of the poroelastic material $\sigma^s_s(\mathbf{r})$ has to be zero on the interface. The final condition represents the continuity of the normal volume velocity where the velocity operator is defined as:

$$\mathcal{L}_v = \frac{j}{\rho_0 \omega} \frac{\partial}{\partial \mathbf{n}}, \tag{88}$$

with $\mathbf{n}$ the normal direction of the boundary. The first three boundary conditions are imposed on the poroelastic domain, the last one on the acoustic domain.

To ensure continuity between two different poroelastic domains, continuity conditions between the approximations in each of the subdomains need to be imposed. Since in both subdomains, three decoupled Helmholtz equations are considered, six continuity conditions have to be imposed. This leads to the following six residuals [23]:

$$\mathbf{r} \in \Gamma^{pp}_C : \begin{cases} R^{p1p2}_{u^s_n}(\mathbf{r}) = u^{s,p1}_n(\mathbf{r}) + u^{s,p2}_n(\mathbf{r}) = 0, \\ R^{p1p2}_{u^s_s}(\mathbf{r}) = u^{s,p1}_s(\mathbf{r}) + u^{s,p2}_s(\mathbf{r}) = 0, \\ R^{p1p2}_{u^f_n}(\mathbf{r}) = \phi_{p1}(u^{f,p1}_n(\mathbf{r}) - u^{s,p1}_n(\mathbf{r})) \\ \quad + \phi_{p2}(u^{f,p2}_n(\mathbf{r}) - u^{s,p2}_n(\mathbf{r})) = 0, \\ R^{p1p2}_{\sigma^s_n}(\mathbf{r}) = (\sigma^{s,p1}_n(\mathbf{r}) + \sigma^{f,p1}(\mathbf{r})) \\ \quad - (\sigma^{s,p2}_n(\mathbf{r}) + \sigma^{f,p2}(\mathbf{r})) = 0, \\ R^{p1p2}_{\sigma^s_s}(\mathbf{r}) = \sigma^{s,p1}_s(\mathbf{r}) - \sigma^{s,p2}_s(\mathbf{r}) = 0, \\ R^{p1p2}_{\sigma^f}(\mathbf{r}) = \frac{\sigma^{f,p1}(\mathbf{r})}{\phi_{p1}} - \frac{\sigma^{f,p2}(\mathbf{r})}{\phi_{p2}} = 0. \end{cases} \tag{89}$$

where superscripts $p1$ and $p2$ indicate the two different materials. Three conditions have to be imposed on the first problem domain and the other three on the second poroelastic subdomain. Logically, the continuity conditions are affected by the porosities of the layers.

2.2.3 Material properties characterisation

The models discussed in the previous sections require a number of material parameters, and the accuracy of the outcome of course depends on the accuracy with which the material parameters are retrieved. As dedicated tests are required for each of the parameters, the characterisation process can be time consuming. A discussion of all characterisation methods for the different parameters is beyond the scope of this paper. An overview of testing procedures can be found a.o. in [23, 39, 66–69].

2.2.4 Transversally isotropic and anisotropic poroelastic materials

The focus in this review article is on models to predict the behaviour of isotropic poroelastic materials. This section briefly discusses the modelling of transversally and more general anisotropic poroelastic materials.

Whereas poroelastic materials are often modelled as being isotropic, this is in reality of course not the case. The manufacturing processes influence the microstructure of the poroelastic medium and induce a certain degree of anisotropy in the macroscopic properties of the material. Commonly, materials are considered as being transversally isotropic, for instance due to the

layered structure of fibrous material or due to the effect of gravity when growing a foam. Wave propagation in transversally isotropic materials is described in e.g. [70,71] where the axis of symmetry is perpendicular to the surface.

Biot [25] also initiated works on the acoustic propagation in orthotropic and anisotropic materials. The textbook by Carcione [72] covers various aspects of anisotropy. Hörlin and Göransson [73] derive constitutive relations for anisotropic porous materials assuming that the frame material itself is isotropic and that the anisotropy results from the microstructure geometry. They present two formulations together with their associated weak formulations to be used in a finite element environment and also indicate the potential to increase the efficiency of the materials by exploiting the anisotropy and optimising the alignment. As shown numerically by Göransson et al. [74] and Lind Nordgren et al. [75] for fictitious materials, the influence of anisotropy can be significant and the orientation of different layers with respect to each other can be optimised to achieve for instance noise reduction at certain frequencies. The numerical models are still expensive, but they are becoming feasible thanks to the increasing computational resources.

At present, the degree of anisotropy in existing porous material is still unclear. Moreover, not all implications of the anisotropy are yet fully discovered. An important step to investigate the consequences of anisotropy is the further experimental characterisation of the anisotropic properties of these materials.

2.2.5 Double porosity materials with an elastic frame

In Section 2.1.5, the idea of rigid frame materials with double porosity was mentioned. However, if a double porosity material is attached to a vibrating structure, also structural effects should be accounted for. Bécot et al. [76] suggest to substitute K_f and ρ_f in the Biot model by K_{dp} and ρ_{dp}, assuming that the viscous and thermal effects in double porosity materials are not modified due to deformations of the frame. Analytical expressions are derived and validated against measurements, indicating a good correlation. Dazel et al. [77] use a similar reasoning but use the transversely isotropic models of Khurana et al. [71]. The models take into account the effects of double porosity and effects due to frame deformation.

2.3 Equivalent solid models

Similarly as for rigid frame materials, but under different boundary conditions and/or excitation frequencies, one can assume that no wave propagates in the fluid phase. At very low frequencies, when the wavelength is much larger than the thickness of the poroelastic material, under structural excitations, the rigid frame materials can not be used. However, it can be assumed that the acoustic pressure is the same on both sides of the sample. In that case one may assume that the pressure field is uniform inside the poroelastic material and one may apply an equivalent solid description; by assuming that $\sigma^f(\mathbf{r})$ is zero in equation (58) and by substituting $e^f(\mathbf{r})$ by $\frac{-Q}{R}e^s(\mathbf{r})$ in (57), one simply retrieves the elastic constitutive relations. When frequency increases, and the wavelengths are no longer much larger than the thickness of the poroelastic sample, one should use a model considering two phases, also accounting for the fluid phase. In vibro-acoustic applications, equivalent solid models are not often used, since one considers relatively high frequencies and often acoustic excitations. However, an example can be found in [78] and further discussions on the use and the validity of equivalent plate models is given in [79].

3 Numerical prediction techniques for the modelling of poroelastic materials

In parallel with refinements to the theory of Biot, numerical approaches have been developed to predict the dynamic response of poroelastic materials. Only for simple 1D applications, exact analytical solutions can be found. For more general problems, numerical approaches are mainly applied. In this overview, they are divided into three categories: element based approaches, transfer matrix approaches and Trefftz based approaches.

3.1 Element-based prediction techniques

Element-based techniques are very well suited to tackle arbitrarily shaped systems and are most commonly used to solve vibro-acoustic problems in the low-frequency range. Whereas the Finite Element Method (FEM) [2,3] discretises the whole problem domain into a large number of small problems, the Boundary Element Method (BEM) [4,5] only discretises the boundaries of the problem. The use of BEM consequently leads to a lower number of DOFs and a smaller system to solve, but comes with fully populated and frequency dependent matrices, impeding the use of efficient sparse solvers. Consequently, the BEM is mainly applied for problems with a high volume to boundary ratio, and is also particularly interesting for unbounded problems, since the formulation inherently takes into account the

radiation conditions at infinity. Although mainly FE schemes have been developed to model poroelastic materials within vibro-acoustic problems, e.g. Tanneau et al. presented a BEM formulation for the modelling of the full Biot equations in 2D [80]. The focus of this subsection will, however, be on FE approaches. This section starts with a generalised mathematical formulation of the problem, continuing with the modelling procedure of the FEM. Thereafter, it gives an overview of the method's properties. The last part provides a thorough overview of the state of the art in the modelling of the steady state dynamics of poroelastic materials.

3.1.1 Generalised problem

Consider a general interior steady-state dynamic problem as given in Figure 4. The mathematical description of the dynamic behaviour inside the problem domain Ω consists of a number of N_{DE} coupled differential equations, which can be generally described in the following formalism:

$$\mathcal{D}_j(\mathbf{v}(\mathbf{r})) = \mathcal{F}_j(\mathbf{r}), \quad \mathbf{r} \in \Omega, \quad j = 1, ..., N_{DE}. \tag{90}$$

In this equation, $\mathcal{D}_j(\bullet)$ is a general domain differential operator and $\mathbf{v}(\mathbf{r}) = [v_1(\mathbf{r}), \cdots, v_{N_{DE}}(\mathbf{r})]^T$ is a vector containing the N_{DE} dynamic field variables. The right hand side $\mathcal{F}_j$ represents non-homogeneous forcing terms.

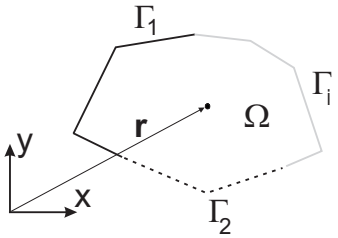

Fig. 4 General interior steady-state dynamic problem description.

On the problem boundary $\Gamma = \bigcup_i \Gamma_i = \partial\Omega$, a number of N_{BC} boundary conditions need to be defined to obtain a well-posed problem. The set of N_{BC} boundary conditions on the problem boundary Γ_i can be written in the general form:

$$\mathcal{B}_{i,l}(\mathbf{v}(\mathbf{r})) = \overline{\mathcal{B}}_{i,l}(\mathbf{r}), \quad \mathbf{r} \in \Gamma_i, \quad l = 1, ..., N_{BC}, \tag{91}$$

with $\mathcal{B}_{i,l}(\bullet)$ a general boundary differential operator and $\overline{\mathcal{B}}_{i,l}(\mathbf{r})$ an imposed boundary field. Note that the subscript $\bullet_{,l}$ denotes a counter, and not a derivation of the parameter $\bullet$ with respect to the parameter l.

The differential equations (90) together with the applied boundary conditions (91) define unique field variables $v_j(\mathbf{r})$.

3.1.2 The FEM modelling procedure

The general modelling procedure of the FEM, as applied to a general set of coupled differential equations, consists of the following four steps, which will be explained afterwards:

A. Discretisation of the problem domain into nodes and elements,
B. Approximation of the field variables by means of polynomial shape functions,
C. Construction of the FE system matrices via a weighted residual formulation of the differential equations and boundary conditions,
D. Solution of the system of equations, yielding the nodal values and postprocessing of the dynamic variables.

Discretisation of the problem domain In a first step, the problem domain is discretised into a large number of small elements which are interconnected by a network of n_{fe} nodes. Figure 5 illustrates the principle.

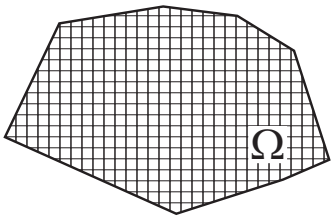

Fig. 5 FE discretisation of a bounded problem domain into elements.

Field variable expansion The steady-state dynamic field $v_j(\mathbf{r})$ in each of the elements is approximated by a solution expansion $\hat{v}_j(\mathbf{r})$ in terms of n_{fe} (polynomial) shape functions N_{f_j}:

$$\begin{aligned} v_j(\mathbf{r}) \simeq \hat{v}_j(\mathbf{r}) &= \sum_{f_j=1}^{n_{fe}} N_{f_j}(\mathbf{r}) v_{f_j} \\ &= \mathbf{N_j}(\mathbf{r})\mathbf{v_j}. \end{aligned} \tag{92}$$

The nodal values v_{f_j} belonging to each of the nodes n_{fe} are gathered in the vector of the degrees of freedom $\mathbf{v_j}$. The row vector $\mathbf{N_j}$ collects the n_{fe} shape functions N_{f_j}. These shape functions are defined per element. Each shape function has a nonzero value in only one element. Moreover, each shape function has a value of 1 for only one DOF of the element and is zero at all others.

Construction of the system of equations The polynomial shape functions do not satisfy the underlying differential equations, nor the imposed boundary conditions. By applying a weighted residual formulation, these errors are orthogonalised with respect to a set of weighting functions $\tilde{\mathbf{t}}(\mathbf{r})$ and minimised:

$$\sum_{j}^{N_{DE}} \int_{\Omega} \tilde{\mathbf{t}}(\mathbf{r}) \, [\mathcal{D}_j(\mathbf{v}(\mathbf{r})) - \mathcal{F}_j(\mathbf{v}(\mathbf{r}))] \, \mathrm{d}\Omega = 0. \tag{93}$$

Through application of the divergence theorem, this strong integral formulation is transformed into integrals over both the domain Ω and its boundary Γ:

$$\begin{aligned} \sum_{j}^{N_{DE}} \Bigg[& \int_{\Omega} \mathcal{W}_{\Omega,j}(\tilde{\mathbf{t}}(\mathbf{r})) \, \mathcal{O}_{\Omega,j}(\mathbf{v}(\mathbf{r})) \mathrm{d}\Omega \\ & - \int_{\Omega} \tilde{\mathbf{t}}(\mathbf{r}) \, \mathcal{F}_j(\mathbf{v}(\mathbf{r})) \mathrm{d}\Omega \\ & + \int_{\Gamma} \mathcal{W}_{\Gamma,j}(\tilde{\mathbf{t}}(\mathbf{r})) \mathcal{O}_{\Gamma,j}(\mathbf{v}(\mathbf{r})) \mathrm{d}\Gamma \Bigg] = 0, \end{aligned} \tag{94}$$

with $\mathcal{W}_{\bullet}(\star)$ and $\mathcal{O}_{\bullet}(\star)$ domain and boundary residual dependent operators. Since $\mathcal{O}_{\bullet}(\star)$ is generally of lower order than $\mathcal{D}_{\bullet}(\star)$, this formulation is referred to as the weak integral formulation.

In a Galerkin weighted procedure, as often applied in the FEM, the weighting functions $\tilde{t}_j(\mathbf{r})$ in the vector $\tilde{\mathbf{t}}(\mathbf{r})$ are expanded in terms of the same locally defined shape functions as for the field variable $v_j(\mathbf{r})$:

$$\begin{aligned} \tilde{t}_j(\mathbf{r}) &= \sum_{f_j=1}^{n_{fe}} N_{f_j}(\mathbf{r}) \tilde{t}_{f_j} \\ &= \mathbf{N_j}(\mathbf{r}) \tilde{\mathbf{t}}_{\mathbf{j}}. \end{aligned} \tag{95}$$

Substitution of the field variable expansion (92) and the weighting function expansion (95) yields an algebraic equation linking the unknown nodal values to each other. The enforcement that these equations should hold for any combination of the weighting functions results in a matrix system of equations. Neumann and Robin boundary conditions can be applied through these boundary residuals. By means of row and column elimination, Dirichlet boundary conditions can be applied such that the final system reads:

$$[\mathbf{D}] \, \{\mathbf{u}\} = \mathbf{f}, \tag{96}$$

where $\mathbf{D}$ represent the dynamic system matrix, $\mathbf{u}$ the vector of unknown nodal values and $\mathbf{f}$ represent loading vectors, containing externally applied forces originating from $\mathcal{F}_j$ in (90).

Solution and postprocessing In a final step, the system matrix of equation (96) is solved for the unknown nodal values. The backsubstitution of these values in the field variable expansions (92) leads to an expression of the approximation of the field variables $\hat{v}_j(\mathbf{r})$ inside the problem domain. Derivative quantities, such as acoustic velocities and structural displacements and stresses can be obtained by applying differential operators to the shape functions. Note however that this always comes with a loss of spatial resolution as they consist of derivatives of the polynomial shape functions.

3.1.3 FEM Properties

The discretisation strategy of the FEM and the use of simple polynomial interpolation functions has its advantages and disadvantages. This leads to the following characteristics:

Problem discretization and degrees of freedom – The FEM divides the problem domain into a large number of small elements. The DOFs in an FE model are the nodal values of the field variables, and inside the elements, the dynamic field is approximated using simple polynomial shape functions. As frequency increases and wavelengths shorten, the FE mesh needs to be refined to retain a similar accuracy as driven by interpolation and pollution errors [6–8].

Problem geometric complexity – Due to the fine discretization typically necessary to capture the wavelength, the FEM has almost no restrictions regarding the geometrical complexity.

System matrix properties – In general, the system matrices of the FEM are real-valued, large, frequency independent and sparsely populated with a banded structure. These properties allow for an efficient solution and a reuse of the matrices for different frequencies. Nevertheless, for some problems, the material properties are complex and frequency dependent. In this case, the FE matrices, which are complex, have to be recalculated for each frequency, hampering the efficient solution and also the applicability of modal reduction schemes.

Accuracy of derivative variables – Since the FEM commonly applies polynomial shape functions to approximate the primary response variables, the higher order derived quantities are approximated with a lower spatial resolution.

Computational performance – Although the FE matrices are in general sparse and symmetric, because of the large number of FE degrees of freedom, the solution of the FE models is computationally demanding. The CPU time required to build and solve the

system is proportional to $N\Delta^2$, with N the number of DOFs and Δ the bandwidth of the system matrix.

3.1.4 FEM for poroelastic materials

When considering FE approaches, a wide range of formulations can be found. When the poroelastic material is represented by an equivalent fluid or a limp material, the problem can be modelled as if it were an acoustic problem, solving a Helmholtz equation with a complex and frequency dependent speed of sound and density, see for instance [81,82]. This implies that, as compared to standard acoustic FE schemes, the matrices need to be recalculated for every frequency, but nevertheless, only one DOF per node is required to represent the dynamic fields.

The formalism of the FEM can also be used to deal with the full Biot equations. This subsection gives an overview of the different formulations which have been presented over time and zooms in on the properties of poroelastic FEM systems and the typical problems with them. Finally, a number of approaches to alleviate these problems are presented.

Formulations Over the years, several formulations have been presented to deal with the full Biot equations:

($\mathbf{u^s}$,$\mathbf{u^f}$)-formulation – This formulation is based on the equations as given in Section 2.2 and applies the displacements of both phases as primary variables. The formulation was used by Kang and Bolton [83] for 2D poroelastic problems, coupled to acoustic cavities. Later, this approach was extended to 3D poroelastic problems [84]. It requires 4(6) displacement DOFs per node for 2(3)D simulations.

First ($\mathbf{u^s}$,$\mathbf{w}$)-formulation – In his later work, Biot developed a second representation of his theory for poroelasticity [55]. This formulation is called the mixed displacement formulation and uses $\mathbf{w}(\mathbf{r}) = \phi(\mathbf{u^f}(\mathbf{r}) - \mathbf{u^s}(\mathbf{r}))$, the fluid flow components relative to the solid skeleton measured in terms of volume per unit area of the bulk medium, as a primary field variables instead of the fluid displacements. Moreover, the stress components $\boldsymbol{\sigma^t}(\mathbf{r})$ and p^f are used instead of $\boldsymbol{\sigma^s}(\mathbf{r})$ and $\boldsymbol{\sigma^f}(\mathbf{r})$. This leads to the following expressions:

$$\begin{aligned}&\nabla\left[(\lambda+N+K_{eq})e^s(\mathbf{r})+K_{eq}e^w(\mathbf{r})\right]\\&+N\nabla^2\mathbf{u^s}(\mathbf{r})=\omega^2(\rho_t\mathbf{u^s}(\mathbf{r})+\rho_0\mathbf{w}(\mathbf{r})),\end{aligned}\tag{97}$$

$$\begin{aligned}&\nabla\left[\phi K_{eq}e^s(\mathbf{r})+\phi K_{eq}e^w(\mathbf{r})\right]=\\&\qquad-\omega^2\left(\rho_2\mathbf{u^s}(\mathbf{r})+\frac{\tilde{\rho}_{22}}{\phi}\mathbf{w}(\mathbf{r})\right),\end{aligned}\tag{98}$$

with $e^w = \nabla\cdot\mathbf{w}(\mathbf{r})$ the volume of fluid which escapes from the pores of a unit volume of bulk material, $\rho_t = \rho_1+\rho_2$ the total density and $K_{eq} = K_f/\phi$ corresponds to the compressibility of the equivalent fluid model. This formulation simplifies the coupling conditions between two layers of different poroelastic materials. By using this formulation, the displacement components $\mathbf{u^s}(\mathbf{r})$ and $\mathbf{w}(\mathbf{r})$ of the two layers have to be equal to each other at the interface. When the ($\mathbf{u^s}$,$\mathbf{u^f}$)-formulation is used, the coupling conditions are more complex since the porosities of both layers should be taken into account. However, performance is similar to the ($\mathbf{u^s}$,$\mathbf{u^f}$)-formulation, requiring also 4(6)DOFs per node for 2(3)D calculations.

Second ($\mathbf{u^s}$,$\mathbf{w}$)-formulation – An alternative ($\mathbf{u^s}$,$\mathbf{w}$)-formulation can be derived by using the stress components $\boldsymbol{\sigma^s}(\mathbf{r})$ and $\boldsymbol{\sigma^f}(\mathbf{r})$ [85,86]:

$$\begin{aligned}&\nabla\left[\left(\lambda+\frac{Q^2}{R}+N+Q\right)e^s(\mathbf{r})+\frac{Q}{\phi}e^w(\mathbf{r})\right]\\&+N\nabla^2\mathbf{u^s}(\mathbf{r})=\omega^2\left(\rho_1\mathbf{u^s}(\mathbf{r})+\frac{\tilde{\rho}_{12}}{\phi}\mathbf{w}(\mathbf{r})\right),\end{aligned}\tag{99}$$

$$\begin{aligned}&\nabla\left[\phi K_{eq}e^s(\mathbf{r})+\phi K_{eq}e^w(\mathbf{r})\right]=\\&\qquad-\omega^2\left(\rho_2\mathbf{u^s}(\mathbf{r})+\frac{\tilde{\rho}_{22}}{\phi}\mathbf{w}(\mathbf{r})\right).\end{aligned}\tag{100}$$

This formulation simplifies the coupling conditions between two layers of different poroelastic materials as well. Performance is similar to the ($\mathbf{u^s}$,$\mathbf{u^f}$)-formulation and the previously mentioned ($\mathbf{u^s}$,$\mathbf{w}$)-formulation, as it also requires 4(6)DOFs per node for 2(3)D calculations.

($\mathbf{u^s}$,p^f,φ^f)-formulation – Göransson [87] formulated the problem based on the solid displacements, the fluid pore pressure $p(\mathbf{r}) = -\phi\sigma^f(\mathbf{r})$ and the fluid displacement scalar potential $\varphi^f(\mathbf{r})$ as primary variables. The fluid scalar potential is defined by:

$$\mathbf{u^f}(\mathbf{r}) = \nabla\varphi^f(\mathbf{r}).\tag{101}$$

As such, the vector potential of the Helmholtz decomposition of a vector field is neglected, excluding the rotational motion of the fluid phase. The three governing equations read:

$$\frac{\phi^2}{R}p^f(\mathbf{r})+\phi\nabla^2\varphi^f(\mathbf{r})+\frac{\phi Q}{R}e^s(\mathbf{r})=0,\tag{102}$$

$$\phi\nabla p^f(\mathbf{r})-\omega^2\left(\tilde{\rho}_{22}\nabla\varphi^f(\mathbf{r})+\tilde{\rho}_{12}\mathbf{u^s}(\mathbf{r})\right)=0,\tag{103}$$

$$N\nabla^2\mathbf{u^s}(\mathbf{r})+\nabla\left(A+N-\frac{Q^2}{R}\right)e^s(\mathbf{r})\tag{104}$$

$$-\frac{\phi Q}{R}\nabla p^f(\mathbf{r})=-\omega^2\left(\tilde{\rho}_{11}\mathbf{u^s}(\mathbf{r})+\tilde{\rho}_{12}\nabla\varphi^f(\mathbf{r})\right).$$

Due to the introduction of the scalar potential, a fully symmetric finite element problem is obtained,

even when coupled to an elastic material or an exterior fluid. The method leads to 5 DOFs as compared to 6 for the $(\mathbf{u^s},\mathbf{u^f})$-formulation for 3D calculations. However, the fluid is forced to be irrotational since only the curl-free component and not the divergence-free component of the Helmholtz decomposition of a vector field is taken into account. Even though the fluid is assumed to be non-viscous in the linear acoustic approximation, due to the interaction between the frame and the fluid, the fluid may be set into rotational motion. This is the case when there are strong viscous and inertial interactions with the solid phase. This is particularly important when materials with a high tortuosity and/or a high flow resistivity are considered.

$(\mathbf{u^s},p^f)$-formulation – This formulation was used by Atalla et al. [88,89] and depends on the fluid pore pressure instead of the fluid displacements. Starting from the momentum equation (51) and using $-\phi\nabla p^f(\mathbf{r}) = \nabla\cdot\boldsymbol{\sigma^f}(\mathbf{r})$, the vector of fluid displacements $\mathbf{u^f}(\mathbf{r})$ can be written as:

$$\mathbf{u^f}(\mathbf{r}) = \frac{\phi}{\tilde{\rho}_{22}\omega^2}\nabla p^f(\mathbf{r}) - \frac{\tilde{\rho}_{12}}{\tilde{\rho}_{22}}\mathbf{u^s}(\mathbf{r}). \tag{105}$$

The stress tensor of the frame *in vacuo* $\hat{\boldsymbol{\sigma}}^{\boldsymbol{s}}(\mathbf{r})$ is introduced, which is independent of the fluid displacement vector $\mathbf{u^f}(\mathbf{r})$:

$$\begin{aligned}\hat{\boldsymbol{\sigma}}^{\boldsymbol{s}}(\mathbf{r}) &= \boldsymbol{\sigma^s}(\mathbf{r}) + \phi\frac{Q}{R}p^f(\mathbf{r})\mathbf{I}\\ &= \left(A - \frac{Q^2}{R}\right)e^s(\mathbf{r})\mathbf{I} + 2N\mathbf{e^s}(\mathbf{r}).\end{aligned} \tag{106}$$

By substituting equations (105) and (106) into equations (50) and (58), the Biot poroelasticity equations in terms of $(\mathbf{u^s},p^f)$ variables are given by:

$$\nabla\cdot\hat{\boldsymbol{\sigma}}^{\boldsymbol{s}}(\mathbf{r}) + \omega^2\tilde{\rho}\mathbf{u^s}(\mathbf{r}) + \tilde{\gamma}\nabla p^f(\mathbf{r}) = 0, \tag{107}$$

$$\nabla^2 p^f(\mathbf{r}) + \omega^2\tfrac{\tilde{\rho}_{22}}{R}p^f(\mathbf{r}) - \omega^2\tilde{\gamma}\tfrac{\tilde{\rho}_{22}}{\phi^2}\nabla\cdot\mathbf{u^s}(\mathbf{r}) = 0, \tag{108}$$

with

$$\tilde{\rho} = \tilde{\rho}_{11} - \frac{\tilde{\rho}_{12}^2}{\tilde{\rho}_{22}}, \tag{109}$$

and

$$\tilde{\gamma} = \phi\left(\frac{\tilde{\rho}_{12}}{\tilde{\rho}_{22}} - \frac{Q}{R}\right). \tag{110}$$

The advantages of this formulation are that the number of degrees of freedom is decreased to 3(4) per node for 2(3)D simulations and it leads to simpler coupling and boundary conditions [63]. Consequently, it is computationally cheaper than the previous approaches.

$(\mathbf{u^s},\mathbf{u^t})$-formulation – Dazel et al. [90] propose an alternative displacement formulation, based on a strain decoupling, in terms of the solid displacement vector $\mathbf{u^s}$ and $\mathbf{u^W} = \phi(\mathbf{u^f} + \frac{Q}{R}\mathbf{u^s})$, which is the apparent displacement for the pressure of the fluid phase taking into account the motion of the solid phase. The equations of motion read:

$$\nabla\cdot\hat{\boldsymbol{\sigma}}^{\boldsymbol{s}}(\mathbf{r}) = -\rho_s\omega^2\mathbf{u^s}(\mathbf{r}) - \rho_{eq}\gamma\omega^2\mathbf{u^W}(\mathbf{r}), \tag{111}$$

$$K_{eq}\nabla\zeta(\mathbf{r}) = -\rho_{eq}\gamma\omega^2\mathbf{u^s}(\mathbf{r}) - \rho_{eq}\omega^2\mathbf{u^W}(\mathbf{r}), \tag{112}$$

with $\zeta(\mathbf{r}) = \nabla\cdot\mathbf{u^W}(\mathbf{r})$ and $\rho_s = \rho_1 + \rho_2\left(\frac{Q^2}{R}\right) - \rho_{12}\frac{\gamma'^2}{\phi^2}$ with $\gamma' = \phi\left(1 + \frac{Q}{R}\right)$. Unlike the $(\mathbf{u^s},\mathbf{u^f})$-equations, there are no stress-coupling terms involved as each stress tensor is a function of the associated displacement only. By using this approach, simpler expressions for the constitutive coefficients and wave numbers are obtained as compared to the $(\mathbf{u^s},\mathbf{u^f})$-formulation. The formulation is also very well-fitted to derive limp and equivalent fluid descriptions.
When the bulk modulus of the porous material *in vacuo* K_b and the effective bulk modulus of air K_f are much smaller than K_s, which is the case for most commonly used poroelastic materials in vibro-acoustic applications, the bulk modulus of the elastic solid from which the skeleton is made of $\mathbf{u^W}(\mathbf{r})$ is equal to the total displacement of the porous material $\mathbf{u^t}(\mathbf{r}) = \phi\mathbf{u^f}(\mathbf{r}) + (1-\phi)\mathbf{u^s}(\mathbf{r})$ and γ' simplifies to 1. As such, the coupling conditions between a poroelastic material and an acoustic, elastic or poroelastic domain simplify. Similarly as for the $(\mathbf{u^s},\mathbf{u^f})$-formulation 4(6) DOFs are required per node for 2(3)D calculations.

$(\mathbf{u^s},p^f,\varphi^f,\boldsymbol{\psi^f})$-formulation – This approach improves the $(\mathbf{u^s},p^f,\varphi^f)$-formulation by Göransson [87] by also taking into account the fluid vector potential $\boldsymbol{\psi^f}(\mathbf{r})$ as a primary field variable [91]. The fluid displacement vector is Helmholtz decomposed into a scalar and a vector potential:

$$\mathbf{u^f}(\mathbf{r}) = \nabla\varphi^f(\mathbf{r}) + \nabla\times\boldsymbol{\psi^f}(\mathbf{r}). \tag{113}$$

The governing equations read:

$$\frac{\phi^2}{R}p^f(\mathbf{r}) + \phi\nabla^2\varphi^f(\mathbf{r}) + \phi\nabla\cdot\nabla\times\boldsymbol{\psi^f}(\mathbf{r}) + \frac{\phi Q}{R}\nabla\cdot\mathbf{u^s}(\mathbf{r}) = 0, \tag{114}$$

$$\phi\nabla p^f(\mathbf{r}) - \omega^2\left(\tilde{\rho}_{22}\left(\nabla\varphi^f(\mathbf{r}) + \nabla\times\boldsymbol{\psi^f}(\mathbf{r})\right)\right) - \omega^2\tilde{\rho}_{12}\mathbf{u^s}(\mathbf{r}) = 0, \tag{115}$$

$$N\nabla^2\mathbf{u^s}(\mathbf{r}) + \nabla(A+N-\frac{Q^2}{R})e^s(\mathbf{r}) - \frac{\phi Q}{R}\nabla p^f(\mathbf{r}) = -\omega^2\left(\tilde{\rho}_{11}\mathbf{u^s}(\mathbf{r}) + \tilde{\rho}_{12}(\nabla\varphi^f(\mathbf{r}) + \nabla\times\boldsymbol{\psi^f}(\mathbf{r}))\right). \tag{116}$$

When deriving the weak form of these equations, equation (115) is weighted with a function which is also written as a Helmholtz decomposed field. Consequently, this equation splits into two equations in the weak formulation as shown in [91]. This formulation leads to symmetric matrices and the potentials in the weak form of this formulation do not appear in the boundary integrals. It is able to represent the same results as obtained by the ($\mathbf{u^s}$,$\mathbf{u^f}$) and the ($\mathbf{u^s}$,p^f) formulation. The computational cost is increased (6(8)DOFs per node for 2(3)D calculations), but the method may be useful for benchmark purposes and possibly for eigenvalues problems.

Due to the lower number of degrees of freedom and the simplified coupling conditions, the ($\mathbf{u^s}$,p^f)-formulation is most commonly used. However, ($\mathbf{u^s}$,$\mathbf{u^f}$) and ($\mathbf{u^s}$,$\mathbf{u^t}$)-approaches are better suited for standard eigenvalue problems, since contrarily to the ($\mathbf{u^s}$,p^f)-formulation, except for parameter dependence, the angular frequency only appears in the numerator.

Specific properties The use of the FEM for poroelastic materials is mainly limited to low frequency calculations due to their high computational cost. The reason is threefold: firstly, the FE matrices have to be recalculated for each frequency due to the frequency-dependent parameters. Secondly, the number of unknowns per node is relatively high. Finally, the physics of poroelastic materials involve short wavelengths. To resolve these, often extremely fine meshes are needed. Since the dimensions of the computational domain are often large as compared to the wavelengths, the numerical dispersion error, also known as pollution error, becomes significant, leading to even more restrictive requirements on the mesh discretisation [78].

Extended frequency range To alleviate these problems, several approaches have been proposed and are being developed. Whenever possible, symmetries should be exploited. Axisymmetric FE models for poroelastic media can be found in [92]. For cylindrical coordinates, instead of using full 3D models, an harmonic expansion has also been proposed for the circumferential direction [93]. Besides, hierarchical elements have been applied [60,65,94]. Linear and quadratic finite elements are however widely used, due to their simplicity.

Another approach is the use of modal reduction schemes. However, because of the complex behaviour of the two coupled phases, with high frequency dependent dissipation mechanisms, the calculation of a modal base is not trivial. Dazel et al. were the first to use generalised complex modes, including non-linearities. The technique applies Taylor expansions for the frequency dependent parameters and solves the eigenvalue problem in a generalised state space. It has been applied for 1D [95] and 3D cases [96]. Whereas it leads to a reduction of the number of degrees of freedom, the calculation of the modes proved very difficult. This has instigated an interest in real, decoupled modal vectors. Sgard et al. [97] calculate the uncoupled, undamped modes of each phase. This, however, neglects the importance of the coupling terms. Davidson and Sandberg [98] propose to calculate in a first step the decoupled modes of both phases and then calculate interface-dependent Lanczos vectors for each mode to construct coupled modes. While providing good results for the shown example in terms of reduction, the efficiency is, however, not discussed. Dazel et al. [99] developed a reduction scheme based on normal modes obtained from the ($\mathbf{u^s}$,$\mathbf{u^t}$)-formulation, showing promising performance for 1D and 2D problems. By using a free interface Component Mode Synthesis, coupled problems (2 poroelastic layers and an acoustic-poroelastic problem) have been studied [100] for 1D problems. The efficiency of the method still needs to be studied for 2D and 3D examples, involving shear waves. Rumpler [101] rewrites the constitutive equations in the ($\mathbf{u^s}$,$\mathbf{u^f}$)-formulation, and proposes the use of real coupled normal modes, based on the conservative poroelastic eigenvalue problem. Also a selection criterion is presented, since the modal base would become too large [102]. The method can be used in combination with Padé approximants for fast multiple frequency sweeps [103]. The approach gives promising results for 3D coupled acoustic poroelastic problems, but still needs to be validated for more complex and for structurally excited poroelastic problems. Recently, Dazel et al. [104] proposed a reduced order model based on a decoupled normal mode basis calculated with a ($\mathbf{u^s}$, p^f)-model and completed with static response vectors of the non-preserved modes. The approach shows a significant reduction in terms of DOFs and in terms of computation time. More-

over, the authors claim that the method is more efficient than other existing modal reduction techniques for poroelastic materials.

3.2 Transfer matrix approaches

At higher frequencies, the Transfer Matrix Method (TMM) is widely used to predict the transmission loss of multilayer structures [23,105,106]. Assuming an infinitely extended material layer, it models the propagation of a plane wave through a layered structure, consisting of e.g. porous, elastic and acoustic layers.

This section starts with a description of the problem and the general modelling procedure. Thereafter, it gives an overview of the limitations of the method and a state of the art of the extensions that have been developed to overcome them.

3.2.1 Problem description

The TMM models the propagation of a plane wave through a multilayer of infinite lateral dimensions. Considering Figure 6, a plane wave impinges upon the multilayer at an angle θ. Because of the infinite layer assumption, the problem geometry is 2D, i.e. in the (x_1, x_3)-plane.

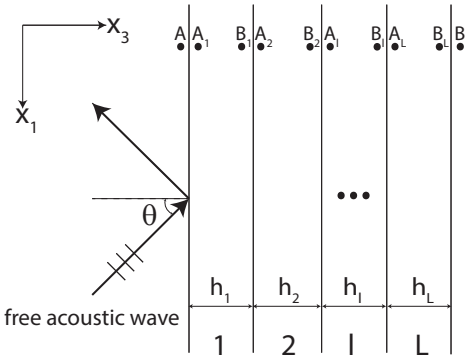

Fig. 6 Infinitely extended multilayer with an impinging plane wave at angle θ.

The sound propagation from the point A to the point B through a multilayer material with thickness $\sum_l h_l$ is governed by a transfer matrix $\mathbf{T}$.

3.2.2 The TMM modelling procedure

The general modelling procedure of the TMM consists of the following steps, which will be explained in more detail and with a specific application to acoustic/poroelastic problems:

A. Partitioning of the multilayer in L layers,
B. Expression of the wave propagation through layer l,
C. Calculation of the layer transfer matrices,
D. Assembly of global transfer matrix through interface and termination conditions.

Partitioning of the multilayer In a first step, the multilayer is divided into l separate layers. For each layer l, the propagating wave field can be decomposed in an incident and a reflected field. This means that for each wave type two constants should be known or, alternatively, two independent field variables. Since the propagation through the multilayer can be described using a low number of degrees of freedom, the method results in a very low computational load.

An acoustic layer only sustains one propagating wave type. It is thus completely defined in each point x_3 by two variables:

$$\mathbf{v_a}(x_3) = \left[p^a(x_3), v_3^a(x_3)\right]^T, \tag{117}$$

using the acoustic pressure and the acoustic velocity in the x_3-direction, respectively.

A poroelastic material, on the other hand, can sustain three different wave types: two dilatational waves and one shear wave. Therefore the complete wave field is only uniquely defined using six independent variables:

$$\mathbf{v_p}(x_3) = \Big[v_1^s(x_3), v_3^s(x_3), v_3^f(x_3)\ , \\ \sigma_{33}^s(x_3), \sigma_{13}^s(x_3), \sigma_{33}^f(x_3)\Big]^T, \tag{118}$$

where $v_1^s(x_3)$, $v_3^s(x_3)$ and $v_3^f(x_3)$ represent the velocity in the solid phase in the x_1- and x_3-direction and the velocity in the fluid phase in the x_3-direction, respectively.

Expression of the wave propagation When travelling under an angle θ in free air, the incident plane wave also has a trace x_1-component. The wave number k_{x_1} can be easily calculated as:

$$k_{x_1} = k_a \sin\theta. \tag{119}$$

For each of the propagating wave types $\bullet$, the x_3-component can then be determined using the dispersion relation

$$k_{\bullet,3} = \sqrt{k_\bullet^2 - k_{x_1}^2}. \tag{120}$$

The wave propagation of the field variables $\mathbf{v_l}$ in a layer l can be generally described in the following format:

$$\mathbf{v_l}(x_3) = \mathbf{\Gamma_l}(x_3)\mathbf{W_l}, \tag{121}$$

with $\mathbf{\Gamma_l}(x_3)$ the propagating wave functions and $\mathbf{W_l}$ the vector containing a linear combination of the amplitudes of the propagating waves in the $\pm x_3$-direction.

For an acoustic layer, the wavenumber k_3 reads:

$$k_{a,3} = \sqrt{k_a^2 - k_{x_1}^2}, \tag{122}$$

and the vector $\mathbf{\Gamma_a}$ is:

$$\mathbf{\Gamma_a}(x_3) = \begin{bmatrix} e^{(-jk_{a,3}x_3)} & e^{(jk_{a,3}x_3)} \\ \frac{k_{a,3}}{\rho_0\omega}e^{(-jk_{a,3}x_3)} & -\frac{k_{a,3}}{\rho_0\omega}e^{(jk_{a,3}x_3)} \end{bmatrix}. \tag{123}$$

For a poroelastic layer, because of the three propagating wave types, the expressions are more complicated. The wavenumber components $k_{l_1,3}$, $k_{l,2,3}$ and $k_{t,3}$ are:

$$k_{\bullet,3} = \sqrt{k_\bullet^2 - k_{x_1}^2} \qquad \bullet = l_1, l_2, t. \tag{124}$$

The vector $\mathbf{\Gamma_p}$ is described in Eq. (125).

Calculation of the layer transfer matrices Setting an arbitrary coordinate system at side B_l, the wave field at both sides of the layer, i.e. at A_l ($x_3 = -h_l$) and B_l ($x_3 = 0$) can be evaluated.

$$\begin{cases} \mathbf{v_l}(A_l) = \mathbf{\Gamma_l}(-h_l)\mathbf{W_l}, \\ \mathbf{v_l}(B_l) = \mathbf{\Gamma_l}(0)\mathbf{W_l}. \end{cases} \tag{126}$$

After elimination of $\mathbf{W_l}$, the layer transfer matrix $\mathbf{T_l}$ can be easily calculated as:

$$\mathbf{T_l} = \mathbf{\Gamma_l}(-h_l)\mathbf{\Gamma_l}(0)^{-1}. \tag{127}$$

Assembly of the global transfer matrix Since not all types of transfer matrices have the same dimensions (e.g. 2×2 for fluid layers and 6×6 for poroelastic layers), the global transfer matrix cannot be calculated using a simple matrix product of the layer transfer matrices. The global transfer matrix $\mathbf{T}$ is assembled from the transfer matrices $\mathbf{T_l}$ of the separate layers, supplemented with interface conditions between the layers and termination conditions at the excitation and the opposite side.

The continuity conditions over the interface between two layers can generally be written in the following matrix form:

$$\mathbf{I_{(l-1)(l)}}\mathbf{v_{(l-1)}}(B_{(l-1)})) + \mathbf{J_{(l-1)(l)}}\mathbf{v_l}(A_l) = 0, \tag{128}$$

with $\mathbf{I_{(l-1)(l)}}$ and $\mathbf{J_{(l-1)(l)}}$ the mutual coupling matrices between layer $(l-1)$ and layer l. The combination of transfer matrices of each layer and interface conditions between subsequent layers, leads to the global transfer matrix, relating the variables on both sides of the multilayer.

The assembled transfer matrix $\mathbf{T_0}$ can then be constructed from the transfer and interface matrices of the separate layers. The total set of wave propagation and interface equations then reads:

$$\mathbf{T_0}\mathbf{v_0} = \mathbf{0}, \tag{129}$$

where

$$\mathbf{T_0} = \begin{bmatrix} \mathbf{I_{f1}} & \mathbf{J_{f1}}\mathbf{T_1} & \mathbf{0} & \cdots & \mathbf{0} & \mathbf{0} \\ \mathbf{0} & \mathbf{I_{12}} & \mathbf{J_{12}}\mathbf{T_2} & \cdots & \mathbf{0} & \mathbf{0} \\ \vdots & \vdots & \vdots & & \vdots & \vdots \\ \mathbf{0} & \mathbf{0} & \mathbf{0} & \cdots & \mathbf{J_{(L-2)(L-1)}}\mathbf{T_{(L-1)}} & \mathbf{0} \\ \mathbf{0} & \mathbf{0} & \mathbf{0} & \cdots & \mathbf{I_{(L-1)L}} & \mathbf{J_{(L-1)L}}\mathbf{T_L} \end{bmatrix}, \tag{130}$$

with $\mathbf{I_{f1}}$ and $\mathbf{J_{f1}}$ the coupling matrices between the free acoustic field and the first layer on the excitation side and

$$\mathbf{v_0} = [\mathbf{v_f}(A), \mathbf{v_1}(B_1), \cdots, \mathbf{v_L}(B_L)]^T. \tag{131}$$

The matrix $\mathbf{T_0}$, however, is not square. Additional conditions are necessary to have a well-posed problem. Both on the excitation and the termination side additional information has to be provided about the impedance, mutually linking the field variables.

On the termination side, two types are possible: rigid wall backing or semi-infinite fluid termination.

For a rigid wall backing, all velocity components are set to zero. Adding these new conditions to the system of equations gives

$$\mathbf{T_t}\mathbf{v_0} = \left[\begin{array}{c} \mathbf{T_0} \\ \hline \mathbf{0} \cdots \mathbf{0}\ \mathbf{R_L} \end{array}\right] \mathbf{v_0} = \mathbf{0}, \tag{132}$$

where $\mathbf{T_t}$ represents the transfer matrix $\mathbf{T_0}$, extended with termination conditions and $\mathbf{R_L}$ is a matrix which consists of a diagonal matrix in the velocity components and an all-zero matrix in the pressure/stress components.

For a semi-infinite fluid termination, the coupling to a fluid is applied for the variables at the termination side. Adding these new equations gives:

$$\mathbf{T_t}\mathbf{v} = \left[\begin{array}{ccc|c} & & & \mathbf{0} \\ & \mathbf{T_0} & & \vdots \\ & & & \mathbf{0} \\ \hline \mathbf{0} & \cdots & \mathbf{0}\ \mathbf{I_{Lf}} & \mathbf{J_{Lf}} \\ 0 & \cdots & 0 & -1\ \frac{Z_B}{\cos\theta} \end{array}\right] \left[\begin{array}{c} \mathbf{v_0} \\ \hline \mathbf{v}(B) \end{array}\right] = \mathbf{0}, \tag{133}$$

On the excitation side, information about the surface impedance of the layer is necessary. This can be introduced by adding a new equation to the global transfer matrix such that

$$\left[\begin{array}{c} -1\ Z_s\ 0 \cdots 0 \\ \hline \mathbf{T_t} \end{array}\right] \mathbf{v_0} = \mathbf{0}, \tag{134}$$

where the surface impedance Z_s can be calculated by

$$Z_s = -\frac{\det \mathbf{T_{t1}}}{\det \mathbf{T_{t2}}}, \tag{135}$$

$$\mathbf{\Gamma_p}(x_3) = \begin{bmatrix} \omega k_{x_1}\cos(k_{l_1,3}x_3) & -j\omega k_{x_1}\sin(k_{l_1,3}x_3) & \omega k_{x_1}\cos(k_{l_2,3}x_3) \\ -j\omega k_{l_1,3}\sin(k_{l_1,3}x_3) & \omega k_{l_1,3}\cos(k_{l_1,3}x_3) & -j\omega k_{l_2,3}\sin(k_{l_2,3}x_3) \\ -j\omega k_{l_1,3}\mu_{l_1}\sin(k_{l_1,3}x_3) & \omega k_{l_1,3}\mu_{l_1}\cos(k_{l_1,3}x_3) & -j\omega k_{l_2,3}\mu_{l_2}\sin(k_{l_2,3}x_3) \\ -D_{l_1}\cos(k_{l_1,3}x_3) & jD_{l_1}\sin(k_{l_1,3}x_3) & -D_{l_2}\cos(k_{l_2,3}x_3) \\ 2jNk_{x_1}k_{l_1,3}\sin(k_{l_1,3}x_3) & -2Nk_{x_1}k_{l_1,3}\cos(k_{l_1,3}x_3) & 2jNk_{x_1}k_{l_2,3}\sin(k_{l_2,3}x_3) \\ -E_{l_1}\cos(k_{l_1,3}x_3) & jE_{l_1}\sin(k_{l_1,3}x_3) & -E_{l_2}\cos(k_{l_2,3}x_3) \end{bmatrix} \quad \cdots$$

$$\cdots \quad \begin{bmatrix} -j\omega k_{x_1}\sin(k_{l_2,3}x_3) & j\omega k_{t,3}\sin(k_{t,3}x_3) & -\omega k_{t,3}\cos(k_{t,3}x_3) \\ \omega k_{l_2,3}\cos(k_{l_2,3}x_3) & \omega k_t\cos(k_{t,3}x_3) & -j\omega k_{x_1}\sin(k_{t,3}x_3) \\ \omega k_{l_2,3}\mu_{l_2}\cos(k_{l_2,3}x_3) & \omega k_{x_1}\mu_t\cos(k_{t,3}x_3) & -j\omega k_{x_1}\mu_t\sin(k_{t,3}x_3) \\ jD_{l_2}\sin(k_{l_2,3}x_3) & 2jNk_{t,3}k_{x_1}\sin(k_{t,3}x_3) & -2Nk_{t,3}k_{x_1}\cos(k_{t,3}x_3) \\ -2Nk_{x_1}k_{l_2,3}\cos(k_{l_2,3}x_3) & N(k_{t,3}^2-k_{x_1}^2)\cos(k_{t,3}x_3) & -jN(k_{t,3}^2-k_{x_1}^2)\sin(k_{t,3}x_3) \\ jE_{l_2}\sin(k_{l_2,3}x_3) & 0 & 0 \end{bmatrix}, \tag{125}$$

where $D_\bullet = (P+Q\mu_\bullet)(k_{x_1}^2+k_{\bullet,3}^2) - 2Nk_{x_1}^2$ and $E_\bullet = (R\mu_\bullet+Q)(k_{x_1}^2+k_{\bullet,3}^2)$ for $\bullet = l_1, l_2$.

with $\mathbf{T_{t1}}$ and $\mathbf{T_{t2}}$ the matrices obtained by removing the first and second column from $\mathbf{T_t}$ respectively.

The resulting matrix $\mathbf{T}$, when equipped with the appropriate impedance and termination relations, is an $(L+2)\times(L+2)$ matrix which relates the dynamic behaviour of both sides of the multilayer.

Applied to a coupled acoustic/poroelastic problem, the continuity conditions, formulated in (87), can be written in the following matrix form:

$$\mathbf{I_{pa}}\mathbf{v_p}(B_p) + \mathbf{J_{pf}}\mathbf{v_a}(A_a) = 0, \tag{136}$$

where

$$\mathbf{I_{pa}} = \begin{bmatrix} 0 & (1-\phi) & \phi & 0 & 0 & 0 \\ 0 & 0 & 0 & 1 & 0 & 0 \\ 0 & 0 & 0 & 0 & 1 & 0 \\ 0 & 0 & 0 & 0 & 0 & 1 \end{bmatrix}, \tag{137}$$

and

$$\mathbf{J_{pa}} = \begin{bmatrix} 0 & -1 \\ (1-\phi) & 0 \\ 0 & 0 \\ \phi & 0 \end{bmatrix}. \tag{138}$$

For an acoustic-poroelastic interface, the matrices are switched, i.e. $\mathbf{J_{pa}}$ becomes $\mathbf{I_{ap}}$ and $\mathbf{I_{pa}}$ becomes $\mathbf{J_{ap}}$.

When coupling two layers of the same nature (e.g. two fluid layers), the global transfer matrix is equal to the product of the separate transfer matrices of the layers. However, for poroelastic layers, this does not hold since the interface conditions are influenced by the porosities of the layers (89).

In this case, the assembled transfer matrix $\mathbf{T_0}$ can be written as a matrix multiplication:

$$\mathbf{T_0} = \mathbf{T_{p1}}\mathbf{I_{p1p2}}\mathbf{T_{p2}}, \tag{139}$$

where

$$\mathbf{I}_{pp} = \begin{bmatrix} 1 & 0 & 0 & 0 & 0 & 0 \\ 0 & 1 & 0 & 0 & 0 & 0 \\ 0 & \left(1-\frac{\phi_{p,2}}{\phi_{p,1}}\right) & \frac{\phi_{p,2}}{\phi_{p,1}} & 0 & 0 & 0 \\ 0 & 0 & 0 & 1 & 0 & \left(1-\frac{\phi_{p,2}}{\phi_{p,1}}\right) \\ 0 & 0 & 0 & 0 & 1 & 0 \\ 0 & 0 & 0 & 0 & 0 & \frac{\phi_{p,2}}{\phi_{p,1}} \end{bmatrix}. \tag{140}$$

A more elaborated overview of the theory of the TMM, including other domain types and interface conditions, can be found in [23].

3.2.3 Extensions

Due to the many assumptions made, either on the material side (homogeneous, infinitely extended flat interface), or on the wave field (plane waves) or on the transmission path, it may be hard to get accurate results in several cases. Therefore, extensions have been developed to enhance the applicability of the TMM over its original assumptions.

Infinite extent – Due to the infinite extent assumption, the TMM is only applicable for layers of finite extent when higher frequencies are considered. Also, when applied to finite structures, the method is mainly useful when locally reacting materials are considered. This means that the local impedance does not depend on the angle of incidence [23].
To account for finite size effects at lower frequencies, Villot [107] applies a spatial windowing correction to the radiation efficiency. Ghinet and Atalla [108] developed the Finite Transfer Matrix method (FTMM) with an alternative correction factor for the radiation efficiency. The FTMM has been applied to calculate transmission loss and absorption of flat finite multilayer structures [109].

Both approaches only account for the geometrical finite size effect. Note that these extensions still do not account for finite size effects caused by the boundary conditions.

Plane wave excitation – The TMM in its original form models the transmission of a plane wave through a multilayer material. However, the method can be extended to more complex load cases by representing the source (e.g. a mechanical point force or an acoustic point source) as a superposition of plane waves in the wave number domain. For each wave number component, the TMM can be applied. Thereafter, the results are recombined using the two-dimensional inverse Fourier transform [23,110].

Transmission path – The TMM assumes that transmission between two layers only happens through the material layer. However, when the structure is stiffened or point connections are present, these can act as sound bridges and provide an additional transmission path from excitation to receiver side. In a first order approximation, these two transmission paths can be considered decoupled and the stiffeners infinitely stiff [111]. However, as Legault and Atalla [112,113] show, the decoupled approaches are highly approximative and next to effects of the stiffness, there are also non-negligible effects of periodicity and mass of the stiffeners.

Isotropy / Homogeneity – The TMM is originally derived for an assembly of laterally infinite, homogeneous isotropic layers. Khuruna et al. [71] extended the application range to transversely isotropic materials. Recently, Verdière et al. [114] extended the framework to heterogeneous materials in the form of patchworks.

Combined techniques – The TMM can be readily exploited in other numerical models. This gives rise to a number of hybrid approaches in which the full modelling of the trim layer can be done using the TMM. In a hybrid coupling between FEM and TMM, the expensive explicit modelling of the multilayer can be replaced by a TM model, while the detailed vibroacoustic system model can still be done using the FEM [115,116]. By combining the TMM and the SEA, the effects of a sound package, i.e. equivalent damping and added mass, can be estimated using the TMM and used further in an SEA approach [23,110]. The TMM also works very well with modal approaches, where for each mode different transfer parameters can be applied, based on a superposition in the wavenumber domain [23,110].

Curvature – So far, the flat panel assumption of the TMM remains one of the major restrictions of the use of the TMM. Nevertheless, this effect is mainly present below the first ring frequency. In some cases, e.g. aircraft fuselages, the curvature is low enough to be neglected in a first order approximation [117].

3.2.4 Applications

Using the TMM, acoustic indicators such as absorption coefficients and transmission loss can be straightforwardly predicted [23].

This ease of use and the method's low computational requirements are distinct advantages of the TMM. Notwithstanding its sometimes crude approximations and inherent limitations, this makes the TMM a very convenient method to predict trends and qualitative results. It is therefore often used in the industrial practice [118,119].

3.3 Trefftz approaches

Trefftz methods are, similarly to element based techniques, deterministic approaches but apply different domain discretisation strategies and different approximation functions. Exact solutions of the governing equations are used to approximate the field variables, leading to a smaller system of equations and higher convergence rates. Whereas Trefftz approaches are widely available in literature for structural and acoustic problems, applications for poroelastic materials are less common. A complete overview of existing Trefftz methods is not the scope of this paper. However, a classification of and a discussion on different Trefftz methods, their advantages and disadvantages, are given in [120].

When considering equivalent fluid problems, governed by a single Helmholtz equation, existing Trefftz-based approaches for acoustics can be easily adapted, taking into account the effective bulk modulus and the density. Examples can be found in [121,122]. The former applies the Partition of Unity Finite Element Method (PUFEM) [13] to predict the sound field in an interior cavity containing poroelastic materials. The PUFEM enriches standard Finite Elements by including exact solutions of the governing Helmholtz equation, in this case plane waves propagating in different directions. The latter applies the WBM, detailed in Section 4, to predict the sound field above a patchwork of poroelastic materials.

For 2D incompressible biphasic media, Trefftz finite elements have been applied in [123]. In hybrid Trefftz FE methods, the Trefftz elements are based on a classical FE discretisation of the problem domain, but the field variable expansion functions satisfy the governing

differential equations. Also for poroelastic media, recently hybrid-Trefftz elements have been applied, with a focus on geomechanical applications [124–126].

For vibro-acoustic applications, the Method of Fundamental Solutions has been applied to poroelastic media [127]. Plane waves impinging on poroelastic scatterers are considered and each of the three poroelastic wave types is modelled using a distribution of monopoles. Recently, the Discontinuous Galerkin Method [128] has been extended for absorbing poroelastic materials described by the Biot theory [129]. Within this method, the governing equations are formulated as a first-order system and the solution and the numerical flux at the interfaces between elements is discussed. The solutions are implemented in function of the three Biot waves. For a simple 2D problem, excellent accuracies have been reported.

Recently, the Wave Based Method has also been extended for poroelastic problems. Given the potential of this method, its general modelling concept and properties are detailed in Section 4. The specific application of the WBM to the Biot equations and its hybrid extension are discussed in Section 5.

4 The Wave Based Method

The WBM [130] is a deterministic numerical modelling method, which belongs to the family of Trefftz approaches [14]. It is designed for solving steady-state dynamic problems, described by a (set of) Helmholtz equation(s), and can be applied to bounded as well as (semi-)unbounded problem domains. Contrarily to element based approaches, which divide the problem domain or the boundary of the problem domain into a large number of small elements, the WBM partitions the problem domain into a small number of large subdomains. Instead of using simple approximating polynomials, the WBM expresses the field variables as a weighted sum of so-called wave functions, which are exact solutions of the governing differential equation(s). The degrees of freedom are the contribution factors of the wave functions in this expansion. The WBM is an indirect approach since the contribution factors are not the dynamic field variables themselves. The wave functions fulfill the dynamic equations *a priori*, but the resulting dynamic field(s) may violate the boundary and continuity conditions. Minimising these errors using a weighted residual formulation leads to a system of linear equations which can be solved for the unknown wave function contribution factors. In a post-processing step, the field variables and derived variables can be determined in the points of interest.

This section explains the modelling procedure of the WBM and gives an overview of its current state of the art and its application areas. A first subsection describes the generalised Helmholtz problem definition. Next, the four steps involved in the WB modelling procedure are detailed. Thereafter, the typical properties of the WB models and their strengths and weaknesses are compared to element based approaches. Finally, the application areas of the WBM and its current state of the art are discussed. An overview of the WB modelling procedure and application areas can also be found in [131,132].

4.1 Generalised Helmholtz problem

Consider a general interior/exterior steady-state dynamic problem as given in Figure 7. It is assumed that the mathematical formulation of the physics inside the problem domain Ω gives rise to, or can be cast by applying for instance the Helmholtz decomposition theorem [133] into a number of N_H (modified) second-order Helmholtz equations:

$$\nabla^2 u_j(\mathbf{r}) + k_j^2 u_j(\mathbf{r}) = \mathcal{Q}_j(\mathbf{r}),\ \mathbf{r} \in \Omega,\ j = 1, ..., N_H. \quad (141)$$

In this equation, ∇^2 is the Laplacian operator, $u_j(\mathbf{r})$ is the dynamic field variable of the j^{th} Helmholtz equation, and k_j is the physical wave number of the j^{th} Helmholtz equation, which is determined by the physical properties of the medium inside the problem domain Ω. $\mathcal{Q}_j(\mathbf{r})$ represents non-homogenous forcing terms. The vector $\mathbf{u}(\mathbf{r}) = [u_1(\mathbf{r}), ..., u_{N_H}(\mathbf{r})]^T$, contains the N_H number of considered dynamic field variables.

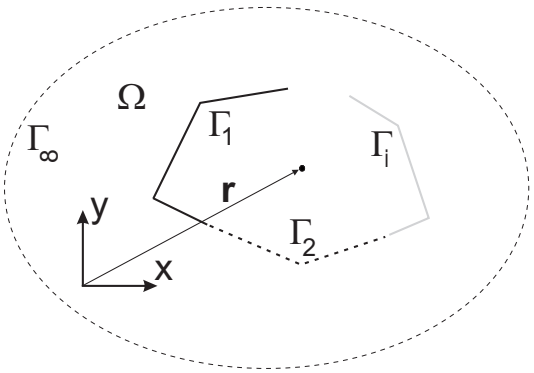

Fig. 7 General steady-state dynamic problem description.

The problem boundary $\Gamma = \partial\Omega$ consists of two parts in case the problem domain is unbounded: the finite part of the boundary, Γ_b, and the boundary at infinity, Γ_∞. For a bounded domain, obviously, only Γ_b has to be considered. The finite part of the boundary

can be divided into non-overlapping parts: $\Gamma_b = \bigcup_i \Gamma_i$, on which different boundary conditions can be imposed. On each point of the boundary, N_H number of boundary conditions need to be defined to obtain a well-posed problem. The set of N_H boundary conditions on a general boundary Γ_i can be written in the general form:

$$\mathcal{H}_{i,l}(\mathbf{u}(\mathbf{r})) = \overline{\mathcal{H}}_{i,l}(\mathbf{r}), \quad \mathbf{r} \in \Gamma_i, \;\; l = 1, ..., N_H, \tag{142}$$

with $\mathcal{H}_{i,l}(\bullet)$ a general boundary differential operator and $\overline{\mathcal{H}}_{i,l}(\mathbf{r})$ an imposed boundary field. Note that the subscript $\bullet_{,l}$ denotes a counter and not a derivation of the parameter $\bullet$ with respect to coordinate l. The N_H number of field variables inside the problem domain are coupled through the boundary conditions. At the boundary at infinity Γ_∞, non-reflecting boundary conditions are imposed, ensuring that the resulting wave field is purely outgoing and no energy is reflected back into the problem domain:

$$\mathcal{H}_{\infty,l}(\mathbf{u}(\mathbf{r})) = 0, \quad \mathbf{r} \in \Gamma_i, \;\; l = 1, ..., N_H. \tag{143}$$

The Helmholtz equation(s) (141) together with the applied boundary conditions (142), and (143) for an unbounded problem, define unique field variables $u_j(\mathbf{r})$. Once these field variables are known, derived quantities can be obtained.

4.2 The WBM modelling procedure

The general modelling procedure of the WBM, as applied to a general Helmholtz problem, consists of the following four steps which will be explained afterwards:

A. Partitioning of the considered problem domain into convex subdomains,
B. Selection of a suitable set of wave functions for each subdomain,
C. Construction of the WB system matrices via a weighted residual formulation of the boundary and interface conditions,
D. Solution of the system of equations, yielding the wave function contribution factors and postprocessing of the dynamic variables.

Partitioning of the problem domain When applied to bounded problems, the convexity of the considered domain is a sufficient condition for the WB approximations to converge towards the exact solution of the problem under study [130]. When the considered problem domain is non-convex, it is, in a first step, partitioned into a number of convex subdomains. When applied to unbounded problems, an initial partitioning of the unbounded domain into a bounded and an unbounded region by a truncation curve Γ_t precedes the partitioning into convex subdomains [120]. Figure 8 illustrates the principle. The unbounded region exterior to Γ_t is considered as one unbounded subdomain.

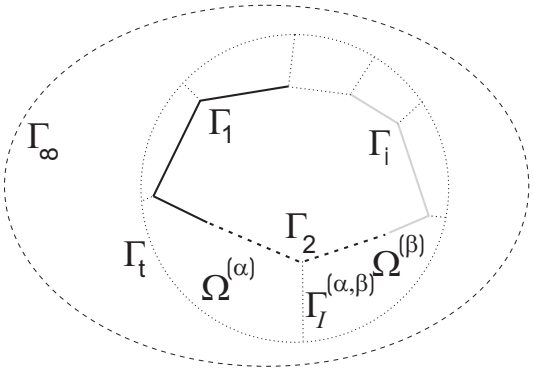

Fig. 8 WB partitioning of an unbounded problem. Subdomain interfaces are shown in dotted lines $(\cdots)$.

Following this approach, the total problem domain Ω is subdivided into N_Ω number of non-overlapping subdomains $\Omega^{(\alpha)}$ $(\alpha = 1, \ldots, N_\Omega)$, which may be bounded or unbounded. On the interface $\Gamma_I^{(\alpha,\beta)}$ between two subdomains $\Omega^{(\alpha)}$ and $\Omega^{(\beta)}$, created in the partition procedure, continuity conditions need to be imposed:

$$\begin{aligned} \mathcal{H}_{I,l}^{(\alpha,\beta)}(\mathbf{u}^{(\alpha)}(\mathbf{r}), \mathbf{u}^{(\beta)}(\mathbf{r})) = 0, \quad & \mathbf{r} \in \Gamma_I^{(\alpha,\beta)} \\ & l = 1, ..., 2N_H, \end{aligned} \tag{144}$$

with $\mathbf{u}^{(\alpha)}(\mathbf{r})$ and $\mathbf{u}^{(\beta)}(\mathbf{r})$ the dynamic field variables in the two adjacent subdomains and $\mathcal{H}_{I,l}^{(\alpha,\beta)}(\bullet,\star) = \mathcal{H}_{I,l}^{(\alpha)}(\bullet) + \mathcal{H}_{I,l}^{(\beta)}(\star)$ a general boundary differential operator expressing the continuity constraints on the fields $\bullet$ and $\star$ and their derived quantities. In order to obtain a well-posed system, one continuity condition is imposed for each of the N_H dynamic variables on each subdomain.

Field variable expansion The steady-state dynamic field(s) $u_j^{(\alpha)}(\mathbf{r})$ in each of the problem subdomains $\Omega^{(\alpha)}$, $\alpha = 1, ..., N_\Omega$, are approximated by a solution expansion $\hat{u}_j^{(\alpha)}(\mathbf{r})$ in terms of $n_j^{(\alpha)}$ wave functions $\Phi_{w_j}^{(\alpha)}$:

$$\begin{aligned} u_j^{(\alpha)}(\mathbf{r}) \simeq \hat{u}_j^{(\alpha)}(\mathbf{r}) &= \sum_{w_j=1}^{n_j^{(\alpha)}} u_{w_j}^{(\alpha)} \Phi_{w_j}^{(\alpha)}(\mathbf{r}) + \hat{u}_{p,j}^{(\alpha)}(\mathbf{r}) \\ &= \mathbf{\Phi}_{\mathbf{j}}^{(\alpha)}(\mathbf{r})\, \mathbf{u}_{\mathbf{j}}^{(\alpha)} + \hat{u}_{p,j}^{(\alpha)}(\mathbf{r}). \end{aligned} \tag{145}$$

The wave function contribution factors $u_{w_j}^{(\alpha)}$ belonging to each of the wave functions $\Phi_{w_j}^{(\alpha)}(\mathbf{r})$ are gathered in

the vector of degrees of freedom $\mathbf{u_j}^{(\alpha)}$. The row vector $\mathbf{\Phi}_\mathbf{j}^{(\alpha)}$ collects the $n_j^{(\alpha)}$ wave functions $\Phi_{w_j}^{(\alpha)}$.

In accordance with the Trefftz principle [14], each of the wave functions $\Phi_{w_j}^{(\alpha)}(\mathbf{r})$ exactly satisfies the homogeneous part of the associated governing Helmholtz equation (141). In the case of an unbounded subdomain, the wave functions are selected to additionally inherently fulfill the non-reflecting boundary condition (143) at Γ_∞. The term $\hat{u}_{p,j}^{(\alpha)}$ represents a particular solution resulting from the combined source terms $\mathcal{Q}_j(\mathbf{r})$ in the right hand side of the inhomogeneous Helmholtz equation (141). Depending on the studied problem, these particular solutions usually take the form of dynamic fields generated by sources or forces in a homogeneous medium which extends to infinity. Consequently, irrespective of the values of the wave function contribution factors, the expansion (145) always satisfies the associated governing Helmholtz equation (141).

Nevertheless, different sets of wave functions can be found, fulfilling these conditions. Several alternative definitions have been proposed in literature (e.g. plane waves [134], the function sets as proposed by Herrera [135],...).

Desmet [130] has proposed to select wave number components based on the characteristic dimensions of the problem at hand. For instance, for a bounded dynamic problem, the smallest rectangle (or rectangular box) circumscribing the considered 2D (3D) problem domains is selected. The combinations of cosine and/or sine functions in one (two) direction(s) and an exponential function in the second (third) direction are used as wave functions. The wave number component(s) associated with the cosine or sine functions are selected such that an integer number of half wavelengths fits into the corresponding bounding box dimension(s). The second (third) wave number component belonging to the exponential function is then selected such that the dispersion relation holds. As such, standing waves in one (two) directions are obtained, multiplied by a propagating or evanescent component in the second (third) direction. Desmet [130] has shown that this set is convergent. Since evanescent components are used in the wave function sets, also near field effects can be captured. The applied sets of wave functions within the WBM for the solution expansions for 2D and 3D bounded and unbounded subdomains, and for various dynamic equations, can be found in the papers cited in Section 4.4 and in Section 5.

Construction of the system of equations Within each subdomain $\Omega^{(\alpha)}$, the proposed solution expansion (145) always exactly satisfies the Helmholtz equation(s) (141), irrespective of the values of the unknown contribution factors $u_{w_j}^{(\alpha)}$. In case an unbounded subdomain is considered, the wave functions also fulfill the radiation condition (143) at Γ_∞. However, the resulting dynamic field(s), such as for instance displacements, stresses etc., which can be obtained by applying an appropriate differential operator to the dynamic field variables $\mathbf{u}(\mathbf{r})$, may violate the imposed boundary conditions on the finite part of the boundary Γ_b and interface conditions. The system of matrices is constructed by minimising these errors by applying a weighted residual approach. The residuals on the boundaries and interfaces of subdomain $\Omega^{(\alpha)}$ are orthogonalised with respect to a set of weighting functions $\tilde{\mathbf{t}}_\bullet^{(\alpha)}$ (146).

The first term comprises the continuity conditions between two subdomains $\Omega^{(\alpha)}$ and $\Omega^{(\beta)}$ and the second term expresses the imposed boundary conditions on subdomain $\Omega^{(\alpha)}$. Similarly as in the FEM, the weighting function $\tilde{\mathbf{t}}_\bullet^{(\alpha)}(\mathbf{r})$ for each type of boundary and continuity condition can be derived from the underlying weighting functions $\tilde{t}_j^{(\alpha)}(\mathbf{r})$ with the same physical meaning as the field variables $u_j^{(\alpha)}$:

$$\tilde{\mathbf{t}}_\bullet^{(\alpha)}(\mathbf{r}) = \mathcal{T}_\bullet\left(\tilde{\mathbf{t}}(\mathbf{r})\right), \tag{147}$$

with $\mathbf{t}(\mathbf{r})$ the vector containing the weighting functions for the different components $t_j^{(\alpha)}$, and $\mathcal{T}_\bullet(\star)$ a problem and boundary condition dependent specific operator, generally determined based on a variational analysis of the considered problem [136]. Similarly to the Galerkin weighted procedure, as often applied in the FEM, the weighting functions $t_j^{(\alpha)}(\mathbf{r})$ are expanded in terms of the same wave functions as for the field variable $u_j^{(\alpha)}(\mathbf{r})$:

$$t_j^{(\alpha)}(\mathbf{r}) = \sum_{w_j=1}^{n_j^{(\alpha)}} \tilde{t}_{w_j}^{(\alpha)} \Phi_{w_j}^{(\alpha)}(\mathbf{r}) = \mathbf{\Phi}_\mathbf{j}^{(\alpha)} \mathbf{t}_\mathbf{j}^{(\alpha)}. \tag{148}$$

Substitution of the field variable expansion (145) and the weighting function expansion (148) yields an algebraic equation, linking the unknown contribution factors of each wave function of subdomain $\Omega^{(\alpha)}$ to the unknown contribution factors of adjacent subdomains. For each subdomain $\Omega^{(\alpha)}$, a similar algebraic equation can be constructed. The enforcement that these N_Ω equations should hold for any combination of the weighting functions results in a matrix system of equations of the following shape:

$$[\mathbf{A}]\{\mathbf{u}\} = \mathbf{b}, \tag{149}$$

with $\mathbf{u}$ the vector containing all $n_w = \sum_{\alpha=1}^{N_\Omega} \sum_{j=1}^{N_H} n_j^{(\alpha)}$ unknown wave function contribution factors, $\mathbf{A}$ the system matrix and $\mathbf{b}$ the right-hand side vector, resulting from non-zero boundary conditions $\bar{\mathcal{H}}_{i,l}(\mathbf{r})$ and particular solution terms $\hat{u}_{p,j}^{(\alpha)}(\mathbf{r})$.

$$\sum_{\beta=1,\beta\neq\alpha}^{N_\Omega}\sum_{l}^{N_H}\int_{\Gamma_I^{(\alpha,\beta)}}\tilde{\mathbf{t}}_{I,l}^{(\alpha)}(\mathbf{r})\,\mathcal{H}_{I,l}^{(\alpha,\beta)}(\hat{\mathbf{u}}^{(\alpha)}(\mathbf{r}),\hat{\mathbf{u}}^{(\beta)}(\mathbf{r}))\mathrm{d}\Gamma+\sum_{i}\sum_{l}^{N_H}\int_{\Gamma_i^{(\alpha)}}\tilde{\mathbf{t}}_{i,l}^{(\alpha)}(\mathbf{r})\,\left[\mathcal{H}_{i,l}(\hat{\mathbf{u}}^{(\alpha)}(\mathbf{r}))-\overline{\mathcal{H}}_{i,l}(\mathbf{r})\right]\mathrm{d}\Gamma=0. \tag{146}$$

Solution and postprocessing In a final step, the system matrix of equation (149) is solved for the n_w number of unknown wave function contribution factors. The back-substitution of these values in the field variable expansions (145) leads to an analytical expression of the approximation of the field variables $\hat{u}_j^{(\alpha)}(\mathbf{r})$ in each of the subdomains $\Omega^{(\alpha)}$. Derivative quantities, such as acoustic velocities and structural displacements and stresses can be easily obtained by applying differential operators to the wave function sets.

4.3 WBM Properties

The FEM and the WBM both belong to the family of deterministic approaches. Nevertheless, due to the fundamentally different choice of approximation functions and domain discretisations, a different modelling procedure and different properties are obtained. This section briefly highlights the advantages and disadvantages of the WB modelling approach.

Problem discretization and degrees of freedom – Contrarily to the FEM, the WBM partitions the domain into a small number of large subdomains, which are frequency independent. The only prerequisite is that the bounded subdomains have to be convex [130]. The applied wave functions are frequency dependent, and they are exact solutions of the governing equations. The DOFs are the contribution factors of each of the wave functions and do not have a direct physical meaning. To obtain a finer spatial resolution of the dynamic field, the number of wave functions is increased, while keeping the domain decomposition the same.

Problem geometric complexity – For the WBM all subdomains need to fulfill the convexity requirement. Non-convex domains have to be partitioned into an as small as possible number of large, convex subdomains. As the number of subdomains increases, so does the number of interfaces and consequently the integration length, leading to an increase in computational load. Consequently, the WBM shows its full efficiency for geometrically simple problems. To increase the applicability of the method, two recent developments partially relax those constraints: the multilevel framework [137, 138] and hybrid approaches [136,139]. The multilevel framework alleviates the problem of multiple scatterers or inclusions. For such problems, the partitioning into convex domains could lead to a very large number of subdomains if it is at all feasible. The multilevel framework treats each of the objects in the problem domain as different levels which consider only the reflection and scattering of one object. By using the superposition theorem, the results of each of the levels are combined. Hybrid approaches combine the best of two worlds and use the ability of element-based techniques to tackle the geometrically complex parts of the problem at hand, and the WBM to deal in a more efficient way with the large, convex parts of the problem domain. The multilevel and hybrid approaches are discussed in somewhat more detail in Section 4.4.

System matrix properties – In contrast to FE matrices, the WB matrices are always complex, frequency dependent and fully populated. The matrices have a limited size but need to be reconstructed for every frequency of interest. As is common for Trefftz approaches, also the WBM yields ill-conditioned matrices [140,141]. However, Desmet [130] has shown that, despite this ill-conditioning, an accurate solution can be obtained by applying direct solution methods if the WB matrices satisfy both Picard conditions [142,143].

Accuracy of derivative variables – Since derivatives of wave functions are again wave functions, with the same spatial resolution, derivative variables are predicted with the same spatial resolution as the primary variables.

Construction of the system matrices – Building the WB models involves the evaluation of integrals of highly oscillatory functions and is computationally more demanding than the construction of the FE matrices, which only requires the integration of simple polynomial functions. Due to the ill-conditioning of the WB matrices, these integrations must be performed carefully to obtain a sufficient accuracy of the matrix coefficients. Numerical integration by applying the Gauss-Legendre integration rule, was shown to be the most efficient for the kind of integrals to be solved for a WB scheme, since an efficient matrix multiplication [136] can be applied. This numerical integration technique is applied with a fixed number of quadrature points per smallest

wavelength resulting from the selected wave number components in the wave function sets.

Computational performance – Since the WB matrices are fully populated, the required CPU time is proportional to N^3. Despite the fact that the construction of the WB matrices is computationally more demanding than the construction of the FE matrices, and the ill-conditioning of the WB matrices prevents the use of fast iterative solvers, due to the difference in size, the solution of the WB system of equations is computationally much less demanding than the solution of the FE system of equations. Furthermore, since the WBM uses a Trefftz basis, it exhibits a high convergence rate, which makes the WBM appropriate to tackle problems for an increased frequency range.

4.4 WBM state of the art

The concept of the WBM has been introduced by Desmet [130] and since then has been the topic of continuous research. This section gives a short overview of the problem types that can currently be tackled by the WBM and discusses two different enhancements to overcome some of the WBM's limitations and to increase its applicability and versatility: the multilevel approach and hybrid-approaches.

Current capabilities of the 'basic' version of WBM As it is already indicated in Section 4.2, every dynamic problem, of which the mathematical formulation is given by or can be cast into a (number of) Helmholtz equation(s), can be tackled by the WBM. So far, the WBM has been applied to the following problem types:

Interior acoustic problems – The WBM was originally developed for simple interior acoustic problems [130] and was further continued by Van Hal [136,144, 145]. Furthermore, the method was extended to 3D problems [146].

Exterior acoustic problems – Pluymers [144,147] introduced the concept of the initial partitioning of the problem by the truncation boundary Γ_t into a bounded and an unbounded subdomain and defined 2D unbounded wave function sets, not only satisfying the homogeneous Helmholtz equation, but also complying with the Sommerfeld radiation condition at Γ_∞ [148]. This work was extended to 3D unbounded acoustic problems [149] and semi-unbounded problems [150,151].

Plate bending problems – This topic was profoundly studied by Vanmaele et al. [152] using the Kirchhoff theory for thin plates. The presence of stress singularities, occurring in corner points of the plate domain was identified, and special purpose enrichment functions were included in the wave function set to incorporate this behaviour [153].

Plate membrane problems – Vanmaele et al. [154] studied membrane problems after casting the Navier equations into two Helmholtz equations.

Assemblies of flat shells – When two flat plates are connected to each other at a certain angle, the in and out of plane displacement components may greatly influence each other. Vanmaele [155] combined the WB approximation fields for membrane and bending behaviour to model shell behaviour for assemblies consisting of several flat plates.

Coupled vibro-acoustic problems – The WB developments for bounded acoustic and structural models are combined to predict the coupled response of an interior vibro-acoustic problem [136,120,130].

Poroelastic material modelling – Desmet [130] touched upon this topic and indicated a possible way to decouple the dynamic Biot equations into three Helmholtz equations. Lanoye et al. [122] developed a WB procedure to study patchworks of porous materials using an equivalent fluid representation. Further developments in this area are presented in Section 5 [156–159].

Multilevel WBM In the case an unbounded problem geometry contains several scatterers, the WBM loses it attractiveness. The truncation Γ_t needs to enclose all scatterers and inside this truncation, the convexity requirement may lead to a very large number of subdomains. When, for instance, a number of circular scatterers are considered, it is even impossible to obtain convex subdomains. The same holds for a bounded subdomain with (a number of) inclusion(s). To overcome these difficulties, the concept of multi-level modelling was introduced for multiple scattering problems. The procedure is depicted in Figure 9. Each of the scatterers in the problem setting is considered as a different level. In every level, the scattering of just one particular object is taken into account. These different levels can be modelled using the existing unbounded WB methodology. By applying the superposition principle and linking all levels together via a weighted residual approach, a fully coupled numerical model is obtained. As such, dynamic problems containing a number of scatterers can be tackled in a much more efficient way.

The concept was first proposed by Van Genechten et al. [137] for 2D acoustic scattering problems. Later, Bergen [151] extended the concept for 3D acoustic scattering problems. The multi-level concept is, however, not restricted to unbounded problems. Bounded prob-

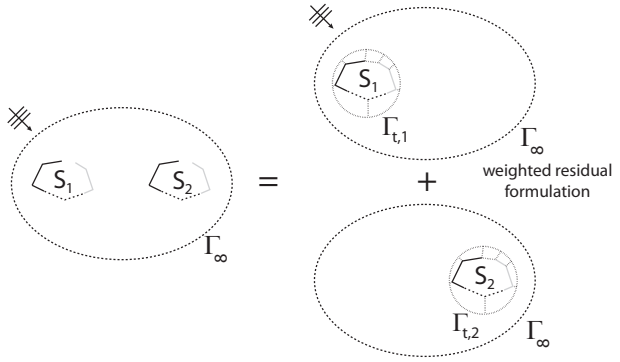

Fig. 9 Concept of the multi-level approach [160].

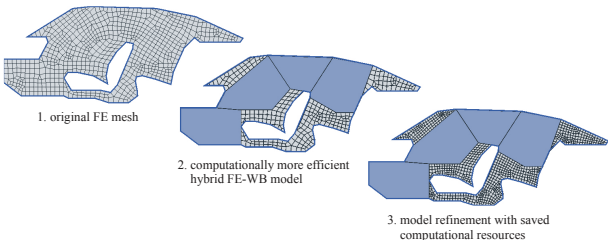

Fig. 10 Concept of hybrid FE-WBM approach [136].

lems, containing a number of inclusions, can be tackled in a completely similar way. Each of the inclusions is studied in a different level, and the surrounding domain is taken into account in an additional, separate level. The 'bounded level' describes the dynamic fields in the bounded domain without inclusions. Van Genechten et al. [138] have applied the multi-level for bounded subdomains with inclusions to 2D acoustic applications and 2D plate membrane problems. Vergote [160] has extended the procedure for plate bending problems.

Hybrid WB methods The second class of enhancements applies the combined use of two numerical methods for one problem under study. Each method is applied according to its own strengths. This way, a strong hybrid approach can be obtained, taking benefit of the best properties of two approaches:

Hybrid Finite Element - Wave Based Method (FE-WBM) – Whereas the WBM is extremely efficient for large problem domains with a simple geometry, the FEM has almost no restrictions regarding the geometrical complexity of a problem domain, but it suffers from dispersion and pollution errors. A hybrid Wave Based-Finite Element Method is developed to benefit from the strengths of both approaches. The main idea is explained in Figure 10. The WBM and the FEM are applied in non-overlapping regions. Large, geometrically simple parts of the problem domain are modelled by the WBM, whereas the FEM focusses on geometrically complex regions. The hybrid FE-WBM approach was proposed by Van Hal [136], who developed two ways of coupling the methods together on the interfaces: a direct and an indirect coupling approach and applied this procedure for 2D bounded acoustic problems. Pluymers [144] extended the approach towards 3D bounded acoustic problems and validated it for several problems of industrial complexity. Vanmaele [155] applied the hybrid methodology to the modelling of membrane problems and for combined plate-beam problems. Van Genechten et al. [139] developed a hybrid WB-FEM for vibro-acoustic problems, modelling the acoustic domain with the WBM and the structural part with the FEM. Van Genechten [161] also proposed to use a modal reduction in the FE subdomain, for a further speed up of the hybrid approach. Bergen [151] proposed a hybrid approach for 2D acoustics, where a finite domain is modelled by the FEM and coupled to an unbounded WB domain outside a circular truncation Γ_t. This approach can be seen as an efficient alternative to the classical Dirichlet-to-Neumann-map (DtN) [162]. Recently, a hybrid FE-WBM was proposed for poroelastic domains [163]. Finally, Jonckheere et al. [159] developed a hybrid approach to model trimmed vibro-acoustic problems. The WBM is applied to the acoustic part of the problem whereas the FEM allows the modelling of the trim layer. This procedure is further detailed in Section 5.2.

Hybrid Boundary Element - Wave Based Method (BE-WBM) – By analogy with the hybrid FE-WBM, recently, a hybrid BE-WBM has been developed, which can be deployed for unbounded acoustic problems, containing geometrically simple as well as complex scatterers. In such a setting, the multilevel WB approach still loses its efficiency, since a large number of subdomains are required in the levels containing the geometrically complex scatterers. Atak et al. [164] proposed the hybrid BE-WBM, where the geometrically simple levels are described by the WBM and the complex scatterers, which would require a large number of WB subdomains, are gathered in one level which is described by the BEM.

Hybrid WBM-SEA – At high frequencies, the effect of variability on for instance material properties and problem geometry, which are inevitably present in a real system, have to be accounted for. The study of one deterministic model is no longer representative to predict the response for a number of products. Typically space- and frequency-averaged responses are then calculated by applying a statistical approach such as the SEA [9]. However, when com-

bining different problem types, especially in built-up structures, some parts of the problem may still behave deterministically, whereas other parts already behave statistically. As such, the cost of a full deterministic model can no longer be justified, but also the SEA can no longer be applied on the full system. Shorter and Langley [18] propose a hybrid FE-SEA to handle this type of mixed problems. Vergote [165] substitutes the FE part in such an approach for the WBM, offering an increased efficiency in the mid-frequency range.

5 Development of the WBM for poroelastic materials

This section presents the application of the WBM to poroelastic problems, as described by the theory of Biot. A first subsection explains how the Biot equations can be decoupled and which wave functions should be selected to describe the field variables. 2D Cartesian and axisymmetric problems are considered. The weighted residual formulation is explained and two numerical validation cases show the efficiency of the method. The second subsection explains the hybrid coupling of acoustic wave based domains and poroelastic finite elements. The ($\mathbf{u^s}$,$\mathbf{u^f}$)- and the ($\mathbf{u^s}$,p^f)-formulation are considered. The latter shows more efficient results.

5.1 The WBM for the Biot equations

As indicated in Section 4, the WBM can applied to dynamic problems of which the mathematical formulation gives rise to or can be cast into a (number of) Helmholtz equation(s). The WBM modelling procedure, presented in Section 4.2, remains unchanged. Consequently, the first step consists of the partitioning of the considered problem domain into a number of convex subdomains and adequate coupling conditions have to be specified on the interfaces, as discussed in Subsection 5.1.1. In order to apply the WBM for poroelastic materials, the Biot equations (75)-(76) need to be decoupled; this is the topic of subsection 5.1.2. Subsections 5.1.3 and 5.1.4 discuss the selection of wave functions for 2D Cartesian and axisymmetric subdomains, respectively. The next subsection discusses the construction and solution of the WB system of equations. The efficiency and accuracy of the approach are illustrated by means of two numerical validation cases.

5.1.1 Partitioning of the problem domain and poroelastic interface conditions

In a general poroelastic problem, the domain Ω may be non convex. According to the WB modelling procedure, a non-convex domain Ω has to be divided into N_Ω non-overlapping convex subdomains $\Omega^{(\alpha)}$, $\alpha = 1, ..., N_\Omega$. Also when different poroelastic materials are present, a corresponding division into subdomains is required. To ensure continuity along the poroelastic interfaces $\Gamma_I^{(\alpha,\beta)}$ between two subdomains $\Omega^{(\alpha)}$ and $\Omega^{(\beta)}$, continuity conditions between the approximations in each of the subdomains need to be explicitly imposed. Since in both subdomains, three decoupled Helmholtz equations are considered, six continuity conditions have to be imposed. This leads to the following six residuals [23]:

$$
\mathbf{r} \in \Gamma_I^{(\alpha,\beta)} : \quad
\begin{cases}
R_{u_n^s}^{(\alpha,\beta)}(\mathbf{r}) = u_n^{s(\alpha)}(\mathbf{r}) + u_n^{s(\beta)}(\mathbf{r}) = 0 \\
R_{u_s^s}^{(\alpha,\beta)}(\mathbf{r}) = u_s^{s(\alpha)}(\mathbf{r}) + u_s^{s(\beta)}(\mathbf{r}) = 0 \\
R_{u_n^f}^{(\alpha,\beta)}(\mathbf{r}) = \phi^{(\alpha)} \left(u_n^{f(\alpha)}(\mathbf{r}) - u_n^{s(\alpha)}(\mathbf{r}) \right) \\
\qquad + \phi^{(\beta)} \left(u_n^{f(\beta)}(\mathbf{r}) - u_n^{s(\beta)}(\mathbf{r}) \right) = 0 \\
R_{\sigma_n^s}^{(\alpha,\beta)}(\mathbf{r}) = (\sigma_n^{s(\alpha)}(\mathbf{r}) + \sigma^{f(\alpha)}(\mathbf{r})) \\
\qquad - (\sigma_n^{s(\beta)}(\mathbf{r}) + \sigma^{f(\beta)}(\mathbf{r})) = 0 \\
R_{\sigma_s^s}^{(\alpha,\beta)}(\mathbf{r}) = \sigma_s^{s(\alpha)}(\mathbf{r}) - \sigma_s^{s(\beta)}(\mathbf{r}) = 0 \\
R_{\sigma^f}^{(\alpha,\beta)}(\mathbf{r}) = \frac{\sigma^{f(\alpha)}(\mathbf{r})}{\phi^{(\alpha)}} - \frac{\sigma^{f(\beta)}(\mathbf{r})}{\phi^{(\beta)}} = 0
\end{cases} , \tag{150}
$$

The first three conditions are imposed on subdomain $\Omega^{(\alpha)}$, the last three on subdomain $\Omega^{(\beta)}$. Together with the boundary conditions (84)-(86), three conditions are defined on each point of the boundary of each subdomain, leading to a well-posed problem description.

5.1.2 Decoupling of the Biot equations

Two possible decompositions for displacements in the solid phase are presented, which are valid for isotropic materials:

A. By applying the divergence operation and the curl operation to the Biot equations [166], the displacement field can be decomposed into two dilatational strains, $e_1^s(\mathbf{r})$ and $e_2^s(\mathbf{r})$, and a rotational strain, $\mathbf{\Omega^s}(\mathbf{r})$:

$$
\mathbf{u^s}(\mathbf{r}) = \nabla\Big(- \frac{1}{k_{l_1}^2} e_1^s(\mathbf{r}) - \frac{1}{k_{l_2}^2} e_2^s(\mathbf{r}) \Big) + \nabla \times \frac{1}{k_t^2} \mathbf{\Omega^s}(\mathbf{r}). \tag{151}
$$

In this decomposition, the dilatation of the solid phase $e^s(\mathbf{r}) = e_1^s(\mathbf{r}) + e_2^s(\mathbf{r})$ and the rotational strain

of the solid phase $\Omega^s(\mathbf{r})$ is given by the curl of the displacement of the solid phase:

$$\boldsymbol{\Omega}^{\mathbf{s}}(\mathbf{r}) = \nabla \times \mathbf{u}^{\mathbf{s}}(\mathbf{r}). \tag{152}$$

B. The second transformation is based on the Helmholtz decomposition of a vector field [133] which states that any vector field can be decomposed into an irrotational and a solenoidal part, provided that this vector field is piecewise differentiable. This transformation is discussed in [23] and leads to a decomposition into two scalar potentials, $\varphi_1^s(\mathbf{r})$ and $\varphi_2^s(\mathbf{r})$, and a vector potential, $\boldsymbol{\psi}^{\boldsymbol{s}}(\mathbf{r})$:

$$\mathbf{u}^{\mathbf{s}}(\mathbf{r}) = \nabla\Big(\varphi_1^s(\mathbf{r}) + \varphi_2^s(\mathbf{r})\Big) + \nabla \times \boldsymbol{\psi}^{\boldsymbol{s}}(\mathbf{r}). \tag{153}$$

By substituting these expressions in the Biot equations, three decoupled Helmholtz equations are found, representing the two longitudinal wave types and the shear wave which can propagate in poroelastic materials:

$$\left(\nabla^2\varsigma_1^s(\mathbf{r}) + k_{l_1}^2\varsigma_1^s(\mathbf{r})\right)\left(\nabla^2\varsigma_2^s(\mathbf{r}) + k_{l_2}^2\varsigma_2^s(\mathbf{r})\right) = 0, \tag{154}$$

$$\nabla^2\boldsymbol{\chi}^{\boldsymbol{s}}(\mathbf{r}) + k_t^2\boldsymbol{\chi}^{\boldsymbol{s}}(\mathbf{r}) = 0, \tag{155}$$

in which $\varsigma^s(\mathbf{r}) = \varsigma_1^s(\mathbf{r}) + \varsigma_2^s(\mathbf{r})$ is either the steady-state volumetric strain $e^s(\mathbf{r})$ or the scalar potential $\varphi^s(\mathbf{r})$ and $\boldsymbol{\chi}^{\boldsymbol{s}}(\mathbf{r})$ is either the steady-state rotational strain $\boldsymbol{\Omega}^{\boldsymbol{s}}(\mathbf{r})$ or the vector potential $\boldsymbol{\psi}^{\boldsymbol{s}}(\mathbf{r})$. Expressions for the wave numbers k_{l_1}, k_{l_2} and k_t are given in equations (77)-(78).

According to the WB principle, each of those three strain (potential) fields in a convex subdomain $\Omega^{(\alpha)}$, is then approximated by a set of wave functions, which are exact solutions of the accompanying Helmholtz equation. Since the wave function sets are different in Cartesian coordinates and in cylinder coordinates, these will be discussed separately.

5.1.3 Wave function selection for 2D Cartesian poroelastic problems

Consider a 2D poroelastic convex subdomain $\Omega^{(\alpha)}$ in a Cartesian coordinate system as shown in Figure 11. It is assumed that the poroelastic field variables are independent of the z-coordinate. Consequently, $\boldsymbol{\chi}^{\boldsymbol{s}}(\mathbf{r}) = \chi^s(\mathbf{r})\cdot\mathbf{e}_z$, with $\mathbf{e}_z$ the unit vector normal to the considered xy-plane. Equation (155) can then be written as a scalar Helmholtz equation:

$$\nabla^2\chi^s(\mathbf{r}) + k_t^2\chi^s(\mathbf{r}) = 0. \tag{156}$$

Each of the three variables, $\varsigma_1^{s^{(\alpha)}}(\mathbf{r})$, $\varsigma_2^{s^{(\alpha)}}(\mathbf{r})$ and $\chi^{s^{(\alpha)}}(\mathbf{r})$ in subdomain $\Omega^{(\alpha)}$ is approximated by a solution expansion in terms of $n_\bullet^{(\alpha)}$ wave functions $\Phi_{w_\bullet}^{(\alpha)}$

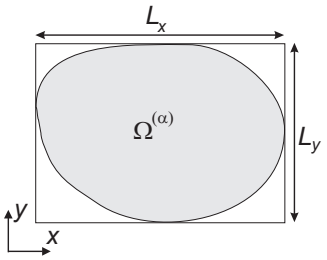

Fig. 11 2D WB subdomain in cartesian coordinates.

$(w_\bullet = 1, ..., n_\bullet^{(\alpha)})$:

$$\begin{cases} \varsigma_1^{s^{(\alpha)}}(\mathbf{r}) \simeq \hat{\varsigma}_1^{s^{(\alpha)}}(\mathbf{r}) = \displaystyle\sum_{w_{\varsigma_1}=1}^{n_{\varsigma_1}^{(\alpha)}} u_{w_{\varsigma_1}}^{(\alpha)}\Phi_{w_{\varsigma_1}}^{(\alpha)}(\mathbf{r}) \\ \qquad\qquad = \boldsymbol{\Phi}_{\mathbf{w}_{\boldsymbol{\varsigma_1}}}^{(\alpha)}(\mathbf{r})\mathbf{u}_{\mathbf{w}_{\boldsymbol{\varsigma_1}}}^{(\alpha)} \\ \varsigma_2^{s^{(\alpha)}}(\mathbf{r}) \simeq \hat{\varsigma}_2^{s^{(\alpha)}}(\mathbf{r}) = \displaystyle\sum_{w_{\varsigma_2}=1}^{n_{\varsigma_2}^{(\alpha)}} u_{w_{\varsigma_2}}^{(\alpha)}\Phi_{w_{\varsigma_2}}^{(\alpha)}(\mathbf{r}) \\ \qquad\qquad = \boldsymbol{\Phi}_{\mathbf{w}_{\boldsymbol{\varsigma_2}}}^{(\alpha)}(\mathbf{r})\mathbf{u}_{\mathbf{w}_{\boldsymbol{\varsigma_2}}}^{(\alpha)} \\ \chi^{s^{(\alpha)}}(\mathbf{r}) \simeq \hat{\chi}^{s^{(\alpha)}}(\mathbf{r}) = \displaystyle\sum_{w_\chi=1}^{n_\chi^{(\alpha)}} u_{w_\chi}^{(\alpha)}\Phi_{w_\chi}^{(\alpha)}(\mathbf{r}) \\ \qquad\qquad = \boldsymbol{\Phi}_{\mathbf{w}_\chi}^{(\alpha)}(\mathbf{r})\mathbf{u}_{\mathbf{w}_\chi}^{(\alpha)} \end{cases}, \tag{157}$$

The wave function contribution factors $u_{w_\bullet}^{(\alpha)}$ belonging to each of the wave functions are gathered in the vectors of degrees of freedom $\mathbf{u}_{\mathbf{w}_\bullet}^{(\alpha)}$. The row vectors $\boldsymbol{\Phi}_{\mathbf{w}_\bullet}^{(\alpha)}(\mathbf{r})$ collect the $n_\bullet^{(\alpha)}$ wave functions $\Phi_{w_\bullet}^{(\alpha)}(\mathbf{r})$. Each wave function $\Phi_{w_\bullet}^{(\alpha)}(\mathbf{r})$ exactly satisfies the corresponding homogeneous Helmholtz equation in (154) and (155). For two-dimensional bounded domains, for each of the three variables, four sets of wave functions are introduced, indicated by superscripts a, b, c and d:

$$\begin{aligned} \sum_{w_\bullet=1}^{n_\bullet^{(\alpha)}} u_{w_\bullet}^{(\alpha)}\Phi_{w_\bullet}^{(\alpha)}(\mathbf{r}) &= \sum_{w_\bullet=1}^{n_\bullet^{a(\alpha)}} u_{w_\bullet}^{a(\alpha)}\Phi_{w_\bullet}^{a(\alpha)}(\mathbf{r}) \\ &+ \sum_{w_\bullet=1}^{n_\bullet^{b(\alpha)}} u_{w_\bullet}^{b(\alpha)}\Phi_{w_\bullet}^{b(\alpha)}(\mathbf{r}) + \sum_{w_\bullet=1}^{n_\bullet^{c(\alpha)}} u_{w_\bullet}^{c(\alpha)}\Phi_{w_\bullet}^{c(\alpha)}(\mathbf{r}) \\ &+ \sum_{w_\bullet=1}^{n_\bullet^{d(\alpha)}} u_{w_\bullet}^{d(\alpha)}\Phi_{w_\bullet}^{d(\alpha)}(\mathbf{r}), \end{aligned} \tag{158}$$

with $n_\bullet^{(\alpha)} = n_\bullet^{a(\alpha)} + n_\bullet^{b(\alpha)} + n_\bullet^{c(\alpha)} + n_\bullet^{d(\alpha)}$, where $\bullet$ can be ς_1^s, ς_2^s or χ^s. The wave functions are defined as:

$$\begin{cases} \Phi_{w_\bullet}^{a(\alpha)}(x,y) = \sin(k_{xw_\bullet}^{a(\alpha)}x)e^{-jk_{yw_\bullet}^{a(\alpha)}y} \\ \Phi_{w_\bullet}^{b(\alpha)}(x,y) = \cos(k_{xw_\bullet}^{b(\alpha)}x)e^{-jk_{yw_\bullet}^{b(\alpha)}y} \\ \Phi_{w_\bullet}^{c(\alpha)}(x,y) = e^{-jk_{xw_\bullet}^{c(\alpha)}x}\sin(k_{yw_\bullet}^{c(\alpha)}y) \\ \Phi_{w_\bullet}^{d(\alpha)}(x,y) = e^{-jk_{xw_\bullet}^{d(\alpha)}x}\cos(k_{yw_\bullet}^{d(\alpha)}y) \end{cases}, \tag{159}$$

The only requirement for these wave functions to be exact solutions of one of the three Helmholtz equations in (154) and (155) is that the wave number components in (159) satisfy the associated dispersion relation:

$$\begin{aligned}&\left(k_{xw_\bullet}^{a(\alpha)}\right)^2+\left(k_{yw_\bullet}^{a(\alpha)}\right)^2=\left(k_{xw_\bullet}^{b(\alpha)}\right)^2+\left(k_{yw_\bullet}^{b(\alpha)}\right)^2=\\&\left(k_{xw_\bullet}^{c(\alpha)}\right)^2+\left(k_{yw_\bullet}^{c(\alpha)}\right)^2=\left(k_{xw_\bullet}^{d(\alpha)}\right)^2+\left(k_{yw_\bullet}^{d(\alpha)}\right)^2=k_j^2,\end{aligned}\tag{160}$$

with k_j one of the three physical wave numbers, k_{l_1}, k_{l_2} or k_t. Similarly as proposed for acoustic and vibro-acoustic problems [130], the following wave number components are selected:

$$\begin{aligned}\left(k_{xw_\bullet}^{a(\alpha)},k_{yw_\bullet}^{a(\alpha)}\right)&=\left(k_{xw_\bullet}^{b(\alpha)},k_{yw_\bullet}^{b(\alpha)}\right)\\&=\left(\tfrac{w_{\bullet,1}^{(\alpha)}\pi}{L_x^{(\alpha)}},\pm\sqrt{k_j^2-\left(k_{xw_\bullet}^{a(\alpha)}\right)^2}\right),\end{aligned}\tag{161}$$

$$\begin{aligned}\left(k_{xw_\bullet}^{c(\alpha)},k_{yw_\bullet}^{c(\alpha)}\right)&=\left(k_{xw_\bullet}^{d(\alpha)},k_{yw_\bullet}^{d(\alpha)}\right)\\&=\left(\pm\sqrt{k_j^2-\left(k_{yw_\bullet}^{c(\alpha)}\right)^2},\tfrac{w_{\bullet,2}^{(\alpha)}\pi}{L_y^{(\alpha)}}\right),\end{aligned}\tag{162}$$

where $w_{\bullet,1}^{(\alpha)}=0,1,2,\ldots$ and $w_{\bullet,2}^{(\alpha)}=0,1,2,\ldots$. The constants $L_x^{(\alpha)}$ and $L_y^{(\alpha)}$ are the dimensions of the smallest rectangular bounding box circumscribing the considered subdomain $\Omega^{(\alpha)}$ as illustrated in Figure 11. The wave number components associated with the cosine and sine are selected such that an integer number of half wavelenghts fits into the corresponding dimension of the bounding box. The other wave number components, associated with the exponential functions are selected such that the dispersion relation holds. Standing waves are obtained in one direction as combined with propagating or evanescent components in the other direction. The latter are useful to take into account near field effects. Desmet [130] has shown that this set of wave functions forms a complete set, and that the WBM will converge towards the exact solution of the problem, given that the subdomains are convex. As compared to the wave function sets for acoustic problems, both the sine and cosine functions are included. By using both sets, the system becomes more ill conditioned and theoretically, the inclusion of both sets is not required for convergence. However, if only one set is included, the convergence for structural problems can be rather slow. Vanmaele [155] has shown by numerous validation cases that the inclusion of both sets leads to a faster convergence for structural problems where the displacement field is represented by a similar combination of strain or potentials.

5.1.4 Wave function selection for axisymmetric poroelastic problems

In case rotational symmetry is present in the problem setting, a large amount of computational effort can be saved by explicitly enforcing the symmetry conditions. This is especially the case for axisymmetric problems. When the geometry, the boundary and loading conditions, and the material properties are independent of the circumferential angle, the solution of the problem is also independent of θ. It is then sufficient to consider just a section in (r,z)-coordinates instead of a full 3D model as illustrated in Figure 12.

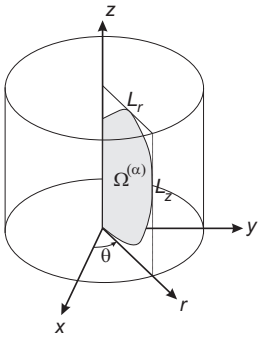

Fig. 12 WB subdomain in axisymmetric coordinates.

For an axisymmetric problem, the displacement associated with the vector potentials can only have components in the r- and the z-direction. Consequently $\boldsymbol{\chi^s}(\mathbf{r})=\chi^s(\mathbf{r})\cdot\mathbf{e}_\theta$, with $\mathbf{e}_\theta$ the unit vector in the θ-direction. By working out the Laplacian operator in cylindrical coordinates on a scalar or a vector field, equations (154) and (155) can be rewritten as:

$$\begin{aligned}&\left[\frac{1}{r}\frac{\partial}{\partial r}\left(r\frac{\partial\varsigma_1^s(r,z)}{\partial r}\right)+\frac{\partial^2\varsigma_1^s(r,z)}{\partial z^2}+k_{l_1}^2\varsigma_1^s(r,z)\right]\\&\quad\left[\frac{1}{r}\frac{\partial}{\partial r}\left(r\frac{\partial\varsigma_2^s(r,z)}{\partial r}\right)+\frac{\partial^2\varsigma_2^s(r,z)}{\partial z^2}\right.\\&\qquad\left.+k_{l_2}^2\varsigma_2^s(r,z)\right]=0,\end{aligned}\tag{163}$$

$$\begin{aligned}&\left(\frac{\partial^2}{\partial r^2}+\frac{1}{r}\frac{\partial}{\partial r}-\frac{1}{r^2}+\frac{\partial^2}{\partial z^2}\right)\chi^s(r,z)\\&\qquad+k_t^2\chi^s(r,z)=0.\end{aligned}\tag{164}$$

In order to apply the WBM, all wave functions in the set have to fulfill the axisymmetric scalar and vector Helmholtz equation. Similarly as for Cartesian coordinates, each of the three field variables $\varsigma_1^{s^{(\alpha)}}(\mathbf{r})$, $\varsigma_2^{s^{(\alpha)}}(\mathbf{r})$ and $\chi^{s^{(\alpha)}}(\mathbf{r})$ in a poroelastic subdomain $\Omega_{pe}^{(\alpha)}$ can be approximated according to equation (157). Each of the wave functions $\Phi_{w_\bullet}(\mathbf{r})$ has to inherently satisfy one of the three associated homogeneous equations as defined

in (163) or (164). In [158] a detailed derivation of complete axisymmetric wave function sets for acoustic and poroelastic subdomains is presented. For axisymmetric poroelastic bounded domains, three sets of wave functions are distinguished, indicated by superscripts s, t and u:

$$\begin{aligned}\sum_{w_\bullet=1}^{n_\bullet^{(\alpha)}} u_{w_\bullet}^{(\alpha)} \Phi_{w_\bullet}^{(\alpha)}(r,z) = \sum_{w_{\bullet,s}=1}^{n_{\bullet,s}^{(\alpha)}} u_{w_{\bullet,s}}^{(\alpha)} \Phi_{w_{\bullet,s}}^{(\alpha)}(r,z) \\ + \sum_{w_{\bullet,t}=1}^{n_{\bullet,t}^{(\alpha)}} u_{w_{\bullet,t}}^{(\alpha)} \Phi_{w_{\bullet,t}}^{(\alpha)}(r,z) + \sum_{w_{\bullet,u}=1}^{n_{\bullet,u}^{(\alpha)}} u_{w_{\bullet,u}}^{(\alpha)} \Phi_{w_{\bullet,u}}^{(\alpha)}(r,z),\end{aligned} \tag{165}$$

with $n_\bullet^{(\alpha)} = n_{\bullet,s}^{(\alpha)} + n_{\bullet,t}^{(\alpha)} + n_{\bullet,u}^{(\alpha)}$ and $\bullet = \varsigma_1, \varsigma_2, \chi$. The wave functions are defined as:

$$\begin{cases} \Phi_{w_{\varsigma_\star,s}}^{(\alpha)}(r,z) = J_0(k_{rw_{\varsigma_\star,s}}^{(\alpha)} r)\cos(k_{zw_{\varsigma_\star,s}}^{(\alpha)} z) \\ \Phi_{w_{\varsigma_\star,u}}^{(\alpha)}(r,z) = J_0(k_{rw_{\varsigma_\star,u}}^{(\alpha)} r)\sin(k_{zw_{\varsigma_\star,u}}^{(\alpha)} z) \\ \Phi_{w_{\varsigma_\star,t}}^{(\alpha)}(r,z) = J_0(k_{rw_{\varsigma_\star,t}}^{(\alpha)} r)\, e^{-jk_{zw_{\varsigma_\star,t}}^{(\alpha)} z} \end{cases}, \tag{166}$$

where $\star$=1,2 and

$$\begin{cases} \Phi_{w_\chi,s}^{(\alpha)}(r,z) = J_1(k_{rw_{\chi,s}}^{(\alpha)} r)\cos(k_{zw_{\chi,s}}^{(\alpha)} z) \\ \Phi_{w_{\chi,u}}^{(\alpha)}(r,z) = J_1(k_{rw_{\chi,u}}^{(\alpha)} r)\sin(k_{zw_{\chi,u}}^{(\alpha)} z) \\ \Phi_{w_{\chi,t}}^{(\alpha)}(r,z) = J_1(k_{rw_{\chi,t}}^{(\alpha)} r)\, e^{-jk_{zw_{\chi,t}}^{(\alpha)} z} \end{cases}, \tag{167}$$

with $J_0(z)$ and $J_1(z)$ the ordinary Bessel functions of first kind and zeroth and first order, respectively. Although the inclusion of both the sine and the cosine set is not strictly necessary for theoretical convergence, also here they are included to obtain a better convergence, following the same reasoning as for Cartesian coordinates. For acoustic axisymmetric problems, in a similar way, only the s- and t-sets are included. The wave number components are given by:

$$\begin{cases} \left(k_{rw_{\varsigma_\star,s}}^{(\alpha)}, k_{zw_{\varsigma_\star,s}}^{(\alpha)}\right) = \left(k_{rw_{\varsigma_\star,u}}^{(\alpha)}, k_{zw_{\varsigma_\star,u}}^{(\alpha)}\right) \\ \qquad = \left(\sqrt{k_{l_\star}^2 - \left(k_{zw_{\varsigma_\star,s}}^{(\alpha)}\right)^2}, \frac{b_{\varsigma_\star,1}^{(\alpha)}\pi}{L_z^{(\alpha)}}\right) \\ \left(k_{rw_{\varsigma_\star,t}}^{(\alpha)}, k_{zw_{\varsigma_\star,t}}^{(\alpha)}\right) \\ \qquad = \left(\lambda_{b_{\varsigma_\star,2}^{(\alpha)}}, \pm\sqrt{k_{l_\star}^2 - \left(k_{rw_{\varsigma_\star,t}}^{(\alpha)}\right)^2}\right) \end{cases} \tag{168}$$

with $\star = 1, 2$ and

$$\begin{cases} \left(k_{rw_{\chi,s}}^{(\alpha)}, k_{zw_{\chi,s}}^{(\alpha)}\right) = \left(k_{rw_{\chi,u}}^{(\alpha)}, k_{zw_{\chi,u}}^{(\alpha)}\right) \\ \qquad = \left(\sqrt{k_t^2 - \left(k_{zw_{\chi,s}}^{(\alpha)}\right)^2}, \frac{b_{\chi,1}^{(\alpha)}\pi}{L_z^{(\alpha)}}\right) \\ \left(k_{rw_{\chi,t}}^{(\alpha)}, k_{zw_{\chi,t}}^{(\alpha)}\right) \\ \qquad = \left(\lambda_{b_{\chi,2}^{(\alpha)}}, \pm\sqrt{k_t^2 - \left(k_{rw_{\chi,t}}^{(\alpha)}\right)^2}\right) \end{cases} \tag{169}$$

with $b_{\bullet,1}^{(\alpha)} = 0, 1, 2, ...$ and the coefficients $b_{\bullet,2}^{(\alpha)} = 0, 1, 2, ...$ are associated with positive roots, $\lambda_{b_{\bullet,2}^{(\alpha)}}$, of $J_1(L_r^{(\alpha)} r)$, with $\bullet = \varsigma_1, \varsigma_2, \chi$. The wave functions that are strictly zero, for instance the sine functions with wave number component zero, are excluded from the resulting wave function sets. $L_r^{(\alpha)}$ and $L_z^{(\alpha)}$ are the dimensions of the smallest rectangular bounding box circumscribing the poroelastic problem subdomain $\Omega^{(\alpha)}$ as illustrated by Figure 12.

5.1.5 Construction and solution of the system of equations

With the use of the selected wave functions in the previous sections, the governing Biot equations are always exactly satisfied, irrespective of the values of the unknown wave function contribution factors. However, the resulting dynamic fields may violate the imposed boundary and interface continuity conditions. Each field variable $a^{(\alpha)}(\mathbf{r})$, which can be the stresses and displacements in both phases, can be written in terms of the strain or potential fields by applying the corresponding differential operator:

$$a^{(\alpha)}(\mathbf{r}) = \mathcal{L}_a^{(\alpha)} \begin{bmatrix} \varsigma_1^{s(\alpha)}(\mathbf{r}) \\ \varsigma_2^{s(\alpha)}(\mathbf{r}) \\ \chi^{s(\alpha)}(\mathbf{r}) \end{bmatrix}. \tag{170}$$

The differential operators for the normal and tangential displacements and the stresses in both the solid and the fluid phase are defined as follows for 2D Cartesian

coordinates:

$$\mathcal{L}^{(\alpha)}_{u^s_n} = \left[c_{l_1} \frac{\partial}{\partial \gamma^{(\alpha)}_n}, \quad c_{l_2} \frac{\partial}{\partial \gamma^{(\alpha)}_n}, \quad c_t \frac{\partial}{\partial \gamma^{(\alpha)}_s} \right], \tag{171}$$

$$\mathcal{L}^{(\alpha)}_{u^s_s} = \left[c_{l_1} \frac{\partial}{\partial \gamma^{(\alpha)}_s}, \quad c_{l_2} \frac{\partial}{\partial \gamma^{(\alpha)}_s}, \quad -c_t \frac{\partial}{\partial \gamma^{(\alpha)}_n} \right], \tag{172}$$

$$\mathcal{L}^{(\alpha)}_{u^f_n} = \left[c_{l_1}\mu_{l_1} \frac{\partial}{\partial \gamma^{(\alpha)}_n}, \; c_{l_2}\mu_{l_2} \frac{\partial}{\partial \gamma^{(\alpha)}_n}, \; c_t\mu_t \frac{\partial}{\partial \gamma^{(\alpha)}_s} \right], \tag{173}$$

$$\mathcal{L}^{(\alpha)}_{\sigma^s_n} = \Bigg[c_{l_1}(2N \frac{\partial^2}{\partial {\gamma^{(\alpha)}_n}^2} + (A + \mu_{l_1} Q)\nabla^2) \,, \; c_{l_2}(2N \frac{\partial^2}{\partial {\gamma^{(\alpha)}_n}^2} + (A + \mu_{l_2} Q)\nabla^2), \; 2c_t N \frac{\partial^2}{\partial \gamma^{(\alpha)}_n \partial \gamma^{(\alpha)}_s} \Bigg], \tag{174}$$

$$\mathcal{L}^{(\alpha)}_{\sigma^s_s} = \left[2N c_{l_1} \frac{\partial^2}{\partial \gamma^{(\alpha)}_n \partial \gamma^{(\alpha)}_s}, \quad 2c_{l_2} N \frac{\partial^2}{\partial \gamma^{(\alpha)}_n \gamma^{(\alpha)}_s}, \quad c_t N (\frac{\partial^2}{\partial {\gamma^{(\alpha)}_s}^2} - \frac{\partial^2}{\partial {\gamma^{(\alpha)}_n}^2}) \right], \tag{175}$$

$$\mathcal{L}^{(\alpha)}_{\sigma^f} = \left[c_{l_1}(Q + \mu_{l_1} R)\nabla^2, \; c_{l_2}(Q + \mu_{l_2} R)\nabla^2, \; 0 \right], \tag{176}$$

where c_{l_1}, c_{l_2} and c_t depend on whether the strain (151) or the potential (153) formulation is used:

$$\text{strains}: \quad c_{l_1} = -\frac{1}{k^2_{l_1}} \quad c_{l_2} = -\frac{1}{k^2_{l_2}} \quad c_t = \frac{1}{k^2_t} \tag{177a}$$

$$\text{potentials}: \quad c_{l_1} = 1 \qquad c_{l_2} = 1 \qquad c_t = 1 \tag{177b}$$

The differential operators for the displacements and the stresses in both the solid and the fluid phase for axisymmetric coordinates read:

$$\mathcal{L}_{u^s_r} = \left[c_{l_1} \frac{\partial}{\partial r}, \quad c_{l_2} \frac{\partial}{\partial r}, \quad -c_t \frac{\partial}{\partial z} \right], \tag{178}$$

$$\mathcal{L}_{u^s_z} = \left[c_{l_1} \frac{\partial}{\partial z}, \quad c_{l_2} \frac{\partial}{\partial z}, \quad c_t \left(\frac{1}{r} + \frac{\partial}{\partial r} \right) \right], \tag{179}$$

$$\mathcal{L}_{u^f_r} = \left[c_{l_1}\mu_{l_1} \frac{\partial}{\partial r}, \quad c_{l_2}\mu_{l_2} \frac{\partial}{\partial r}, \quad -c_t\mu_t \frac{\partial}{\partial z} \right], \tag{180}$$

$$\mathcal{L}_{u^f_z} = \left[c_{l_1}\mu_{l_1} \frac{\partial}{\partial z}, \; c_{l_2}\mu_{l_2} \frac{\partial}{\partial z}, \; c_t\mu_t \left(\frac{1}{r} + \frac{\partial}{\partial r} \right) \right], \tag{181}$$

$$\mathcal{L}_{\sigma^s_{rr}} = \Bigg[c_{l_1} \left(-k^2_{l_1} (A + \mu_{l_1} Q) + 2N \frac{\partial^2}{\partial r^2} \right), \; c_{l_2} \left(-k^2_{l_2} (A + \mu_{l_2} Q) + 2N \frac{\partial^2}{\partial r^2} \right), \; 2c_t N \left(\frac{\partial^2}{\partial r \partial z} \right) \Bigg], \tag{182}$$

$$\mathcal{L}_{\sigma^s_{rz}} = \left[2c_{l_1} N \frac{\partial^2}{\partial r \partial z}, \quad 2c_{l_2} N \frac{\partial^2}{\partial r \partial z}, \quad c_t N \left(-\frac{1}{r^2} + \frac{1}{r}\frac{\partial}{\partial r} + \frac{\partial^2}{\partial r^2} - \frac{\partial^2}{\partial z^2} \right) \right], \tag{183}$$

$$\mathcal{L}_{\sigma^s_{zz}} = \Bigg[c_{l_1} \left(-k^2_{l_1} (A + \mu_{l_1} Q) + 2N \frac{\partial^2}{\partial z^2} \right), \; c_{l_2} \left(-k^2_{l_2} (A + \mu_{l_2} Q) + 2N \frac{\partial^2}{\partial z^2} \right), \; 2c_t N \left(\frac{1}{r}\frac{\partial}{\partial z} + \frac{\partial^2}{\partial r \partial z} \right) \Bigg], \tag{184}$$

$$\mathcal{L}_{\sigma^f} = \Big[-c_{l_1} k^2_{l_1} (Q + \mu_{l_1} R), \; -c_{l_2} k^2_{l_2} (Q + \mu_{l_2} R), \quad 0 \Big]. \tag{185}$$

The boundary and interface residuals of the porous material can be expressed in terms of wave functions using the same differential operators. The mutual coupling between the three wave field components is entirely contained within the conditions specified along the boundaries and interfaces. For each subdomain $\Omega^{(\alpha)}$, the error residual functions are weighted with respect to some arbitrary weighting functions, indicated by $\tilde{\bullet}$. The resulting expression is given in Equation (186). This weighted residual formulation very generally considers all kinds of possible boundary conditions, when only poroelastic subdomains are considered. If also acoustic or elastic subdomains are considered, of course the associated weighted residuals should be added. On each boundary of subdomain $\Omega^{(\alpha)}$ three residuals are imposed. The first six integrals result from the kinematic, mixed and mechanical boundary conditions. As can be seen, on every boundary $\Gamma_\bullet$, exactly the three residuals belonging to this boundary are evaluated. The two last terms in this equation result from interfaces between the considered subdomain $\Omega^{(\alpha)}$ and adjoining subdomains $\Omega^{(\beta)}$. It is supposed that the problem geometry

$$\begin{aligned}\int_{\Gamma_{ki}^{(\alpha)} \cup \Gamma_{mi}^{(\alpha)}} \tilde{\sigma}_n^{s(\alpha)}(\mathbf{r}) R_{u_n^s}^{(\alpha)}(\mathbf{r}) d\Gamma + \int_{\Gamma_{ki}^{(\alpha)}} \tilde{\sigma}_s^{s(\alpha)}(\mathbf{r}) R_{u_s^s}^{(\alpha)}(\mathbf{r}) d\Gamma + \int_{\Gamma_{ki}^{(\alpha)} \cup \Gamma_{mi}^{(\alpha)}} \tilde{\sigma}^{f(\alpha)}(\mathbf{r}) R_{u_n^f}^{(\alpha)}(\mathbf{r}) d\Gamma - \int_{\Gamma_{me}^{(\alpha)}} \tilde{u}_n^{s(\alpha)}(\mathbf{r}) R_{\sigma_n^s}^{(\alpha)}(\mathbf{r}) d\Gamma \\ - \int_{\Gamma_{me}^{(\alpha)} \cup \Gamma_{mi}^{(\alpha)}} \tilde{u}_s^{s(\alpha)}(\mathbf{r}) R_{\sigma_s^s}^{(\alpha)}(\mathbf{r}) d\Gamma - \int_{\Gamma_{me}^{(\alpha)}} \tilde{u}_n^{f(\alpha)}(\mathbf{r}) R_{\sigma^f}^{(\alpha)}(\mathbf{r}) d\Gamma \\ + \sum_{\beta=1, \beta \neq \alpha}^{N_\Omega} \left[\int_{\Gamma_I^{(\alpha,\beta)}} (\tilde{\sigma}_n^{s(\alpha)}(\mathbf{r}) R_{u_n^s}^{(\alpha,\beta)}(\mathbf{r}) + \tilde{\sigma}_s^{s(\alpha)}(\mathbf{r}) R_{u_s^s}^{(\alpha,\beta)}(\mathbf{r}) + \tilde{\sigma}^{f(\alpha)}(\mathbf{r}) R_{u_n^f}^{(\alpha,\beta)}(\mathbf{r})) d\Gamma \right] \\ - \sum_{\beta=1, \beta \neq \alpha}^{N_\Omega} \left[\int_{\Gamma_I^{(\alpha,\beta)}} (\tilde{u}_n^{s(\alpha)}(\mathbf{r}) R_{\sigma_n^s}^{(\alpha,\beta)}(\mathbf{r}) + \tilde{u}_s^{s(\alpha)}(\mathbf{r}) R_{\sigma_s^s}^{(\alpha,\beta)}(\mathbf{r}) + \tilde{u}_n^{f(\alpha)}(\mathbf{r}) R_{\sigma^f}^{(\alpha,\beta)}(\mathbf{r})) d\Gamma \right] = 0.\end{aligned} \tag{186}$$

can consist of N_Ω subdomains. Each two subdomains may or may have not an intermediate interface, which is taken into account by the summation. For every interface, in total six residuals are evaluated. One set is evaluated on the considered subdomain $\Omega^{(\alpha)}$, the other set is evaluated on the adjacent subdomain $\Omega^{(\beta)}$; so for every interface either the first set or the second set is taken into account. The weighting functions $\tilde{a}$ (with a=u_n^s, u_s^s, u_n^f, σ_n^s, σ_s^s, σ^f) are expressed in terms of the same set of wave functions as used in the field variable expansions:

$$\tilde{a}(\mathbf{r}) = \mathcal{L}_a \begin{bmatrix} \tilde{\varsigma}_1^s(\mathbf{r}) \\ \tilde{\varsigma}_2^s(\mathbf{r}) \\ \tilde{\chi}^s(\mathbf{r}) \end{bmatrix} \tag{187}$$

with

$$\tilde{\varsigma}_1^s(\mathbf{r}) = \mathbf{\Phi}_{\mathbf{w}_{\varsigma_1^\mathbf{s}}}^{(\alpha)}(\mathbf{r}) \tilde{\mathbf{u}}_{\mathbf{w}_{\varsigma_1^\mathbf{s}}}^{(\alpha)} \tag{188}$$

$$\tilde{\varsigma}_2^s(\mathbf{r}) = \mathbf{\Phi}_{\mathbf{w}_{\varsigma_2^\mathbf{s}}}^{(\alpha)}(\mathbf{r}) \tilde{\mathbf{u}}_{\mathbf{w}_{\varsigma_2^\mathbf{s}}}^{(\alpha)} \tag{189}$$

$$\tilde{\chi}^s(\mathbf{r}) = \mathbf{\Phi}_{\mathbf{w}_{\chi^\mathbf{s}}}^{(\alpha)}(\mathbf{r}) \tilde{\mathbf{u}}_{\mathbf{w}_{\chi^\mathbf{s}}}^{(\alpha)} \tag{190}$$

Substituting the field variable expansions and the weighting function expansions into the weighted residual formulation for subdomain $\Omega^{(\alpha)}(\mathbf{r})$, yields an algebraic equation which links together the wave function contribution factors of subdomain $\Omega^{(\alpha)}$ and those of the adjacent subdomains. This procedure is repeated for each subdomain. Since these equations should hold for any weighting function and thus for every possible combination of $\tilde{u}_{w_{\bullet_i}}^{(\alpha)}$, a fully populated, complex and generally nonsymmetric system of frequency dependent equations (191) is obtained.

The matrices $\mathbf{A}^{(\bullet,\bullet)}$ are the system matrices, the matrices $\mathbf{C}^{(\bullet,\bullet)}$ are the coupling matrices, linking the wave functions of two adjacent subdomains and $\mathbf{f}^{(\bullet)}$ are the loading vectors resulting from non-homogeneous kinematic, mechanical or mixed boundary condition. For axisymmetric problems, the weighted residual formulation is given in [158].

5.1.6 Accuracy and efficiency

In [156,158] various numerical examples indicate the potential of the WBM for 2D Cartesian and axisymmetric coordinates, respectively. The authors have selected two cases to discuss its potential in this review paper. All WB routines are implemented in Matlab R2010a and the resulting systems of equations are solved using Gaussian elimination. The FE predictions are obtained using COMSOL3.5, a commercial software package, capable of handling weak integral forms. The FE models use a ($\mathbf{u^s}$,$\mathbf{u^f}$)-formulation. Cubic Lagrangian finite elements are used and the models are solved using a direct UMFPACK solver. Subsequent FE meshes are constructed adaptively, based on the L2 norm of the prediction errors. Calculation times always include the construction and the solution time of the system matrices since the models are frequency dependent.

2D Cartesian multilayer problem As an illustration, this review paper discusses the multilayer example presented in [156]. It consists of three poroelastic layers as shown in Figure 13. The top and the bottom layer contain the same polyurethane foam and the middle layer consists of a carpet material. All material properties are given in Appendix A. On all boundaries, except for the top one, sliding edge conditions (86) are imposed. On the top layer an acoustic pressure with the shape $p(x) = 2x^3 - 3x^2 + 1[N/m^2]$ excites the system, leading to the following mechanical boundary conditions on the top layer: $\sigma^{f(3)} = -\phi^{(3)} p^a$, $\sigma_y^{s(3)} = -(1-\phi^{(3)}) p^a$ and $\sigma_{xy}^s = 0[N/m^2]$.

Figure 14 shows the contour map of the absolute value of the relative flux at 600Hz in the multilayer. The results are nicely continuous over the domain interfaces, indicated by dashed lines.

Figure 15 shows frequency response functions of respectively u_y^s and σ^f obtained in two different points in subdomains $\Omega^{(1)}$ and $\Omega^{(2)}$. The FE results are obtained applying 6 adaptive refinements, leading to approximately 330.000 DOFs per frequency line. The results of both methods coincide, indicating a good accuracy

$$\begin{bmatrix} \mathbf{A^{(1,1)}} & \mathbf{C^{(1,2)}} & \dots & \mathbf{C^{(1,N_\Omega)}} \\ \mathbf{C^{(2,1)}} & \mathbf{A^{(2,2)}} & \dots & \mathbf{C^{(2,N_\Omega)}} \\ \vdots & \vdots & \ddots & \vdots \\ \mathbf{C^{(N_\Omega,1)}} & \mathbf{C^{(N_\Omega,2)}} & \dots & \mathbf{A^{(N_\Omega,N_\Omega)}} \end{bmatrix} \cdot \begin{bmatrix} [\mathbf{u^{(1)}_{w_{\varsigma_1}}}\, \mathbf{u^{(1)}_{w_{\varsigma_2}}}\, \mathbf{u^{(1)}_{w_{\chi_t}}}]^\mathbf{T} \\ [\mathbf{u^{(2)}_{w_{\varsigma_1}}}\, \mathbf{u^{(2)}_{w_{\varsigma_2}}}\, \mathbf{u^{(2)}_{w_{\chi_t}}}]^\mathbf{T} \\ \vdots \\ [\mathbf{u^{(N_\Omega)}_{w_{\varsigma_1}}}\, \mathbf{u^{(N_\Omega)}_{w_{\varsigma_2}}}\, \mathbf{u^{(N_\Omega)}_{w_{\chi_t}}}]^\mathbf{T} \end{bmatrix} = \begin{bmatrix} \sum_\beta \mathbf{f^{(1,\beta)}} \\ \sum_\beta \mathbf{f^{(2,\beta)}} \\ \vdots \\ \sum_\beta \mathbf{f^{(N_\Omega,\beta)}} \end{bmatrix} \tag{191}$$

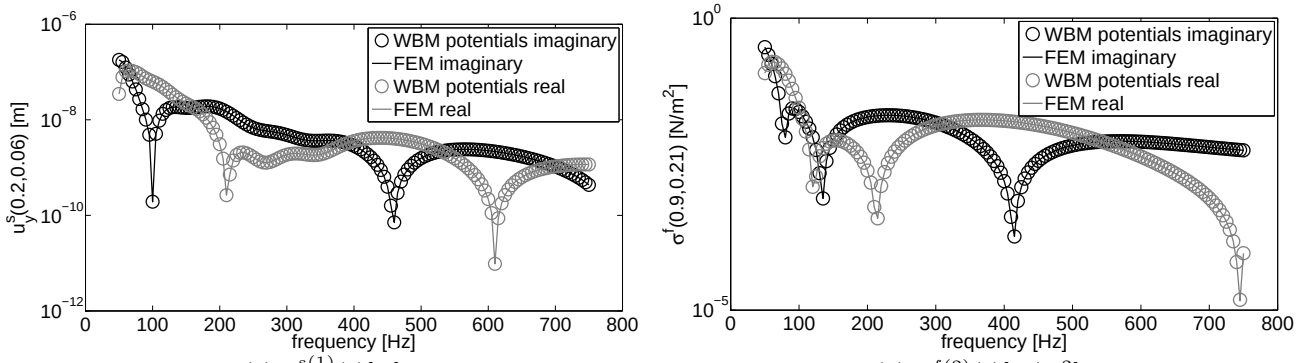

(a) $u_y^{s(1)}(\mathbf{r})[m]$ (b) $\sigma^{f(2)}(\mathbf{r})[N/m^2]$

Fig. 15 Frequency response functions of two different field variables obtained in two different response points in subdomains $\Omega^{(1)}$ and $\Omega^{(2)}$ applying both the FEM and the WB potentials formulation.

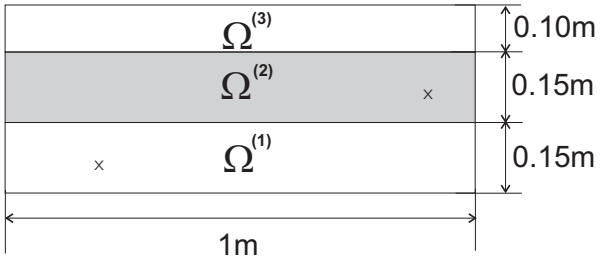

Fig. 13 Multilayer problem description, x indicates postprocessing points.

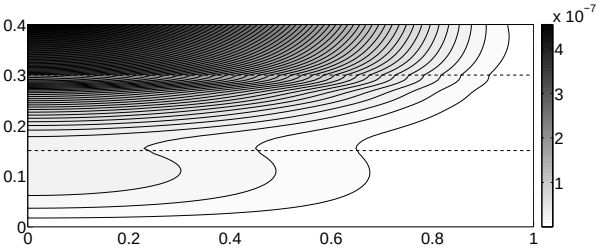

Fig. 14 Contour plot of the relative flux $\phi^{(\alpha)}(u_y^{f(\alpha)}(\mathbf{r}) - u_y^{s(\alpha)}(\mathbf{r}))[m]$ at 600Hz.

is obtained. To compare the convergence rate of the different methods, the relative prediction error $|\epsilon|$ of a variable a is calculated as a function of CPU time. This prediction error is averaged over N response points in the poroelastic domain:

$$|\epsilon| = \frac{1}{N}\sum_{j=1}^{N} \epsilon_j \quad \text{with} \quad \epsilon_j = \frac{|a(\mathbf{r_j}) - a^{ref}(\mathbf{r_j})|}{|a^{ref}(\mathbf{r_j})|} \tag{192}$$

Table 1 FEM reference data for the multilayer problem

200Hz		400Hz	
dofs	cputime [s]	dofs	cputime [s]
1,285,260	779	1,157,736	691

For this example, 36 equally distributed response points are considered in each problem domain. Figures 16 and 17 show convergence curves of $u_y^f(\mathbf{r})$ and $\sigma_{xy}^s(\mathbf{r})$ at 200 and 400Hz, respectively. Eight adaptive refinements are performed on the first FE mesh, which consists of 5688 degrees of freedom. The finest FE models are used as a reference. Details of these models are given in Table 1. For the WBM, the number of wave functions is gradually increased. The relative prediction error is calculated for u_x^f and σ_{xy}^s in each poroelastic subdomain. A high convergence rate and good accuracies are obtained with the WBM, which stagnates at the accuracy of the FE reference model.

For some of the problems presented in [156], the convergence of the WBM is hampered by the matrix condition number. The convergence curves start stagnating before the accuracy of the FE reference is reached. Engineering accuracy is, however, always obtained in a very short calculation time.

Axisymmetric problem case Whereas in [158] a number of convergence studies are performed to validate the efficiency of the axisymmetric WBM, examples of more practical interest are discussed here: the Kundt's tube, as shown in Figure 18. The set-up, dimensions and material properties are inspired by the paper of Vigran

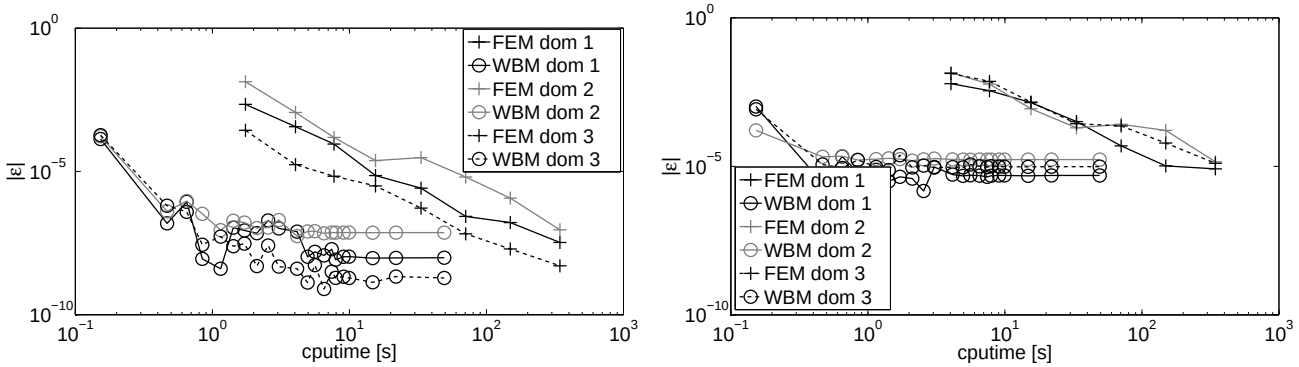

(a) $u_x^f(\mathbf{r})[m]$ (b) $\sigma_{xy}^s(\mathbf{r})[N/m^2]$

Fig. 16 Convergence curves of $u_x^f(\mathbf{r})$ and $\sigma_{xy}^s(\mathbf{r})$ at 200 Hz in each of the three subdomains, calculated with the WB potential formulation and the FEM.

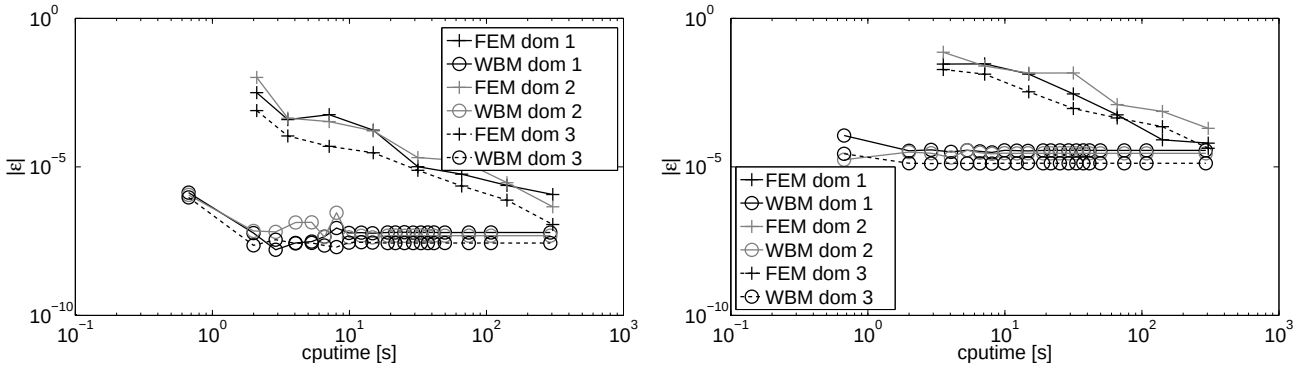

(a) $u_x^f(\mathbf{r})[m]$ (b) $\sigma_{xy}^s(\mathbf{r})[N/m^2]$

Fig. 17 Convergence curves of $u_x^f(\mathbf{r})$ and $\sigma_{xy}^s(\mathbf{r})$ at 400 Hz in each of the three subdomains, calculated with the WB potential formulation and the FEM.

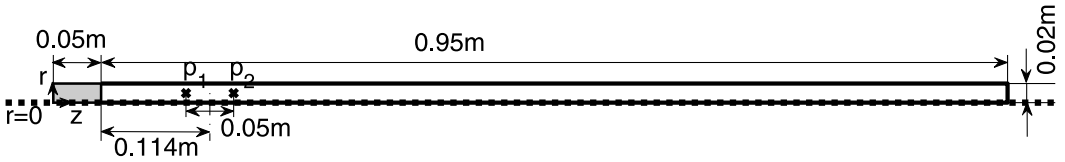

Fig. 18 Problem description Kundt tube set-up.

et al. [167]. The poroelastic material is a polyurethane foam Fireflex of which the properties are given in Appendix A. The poroelastic sample is a cylinder of 5cm thickness, indicated by a grey rectangle on Figure 18. The Kundt tube has a diameter of 4cm and the sample is glued onto a rigid backing, applying fixed boundary conditions (85). The white rectangle in the figure indicates the acoustic domain. On the top edge of the acoustic domain, a normal velocity of zero is imposed, taking into account that the tube is rigid. The acoustic domain is excited with a normal velocity of 1 m/s, imposed on the right hand side of the domain. The x-marks show the positions of two microphones, which are separated by 5cm. In this way, the two-microphone method can be studied, measuring the acoustic pressure at the two nodes and applying the formulas developed for this measurement procedure in order to determine the absorption coefficient. The damping in the acoustic domain is small, but needs to be taken into account when precise measurements, and consequently simulations, are required. The first order high frequency approximation of the acoustic wave number is then given by [168]:

$$k = \frac{\omega}{c_0}\left[1 + \frac{1}{2}(1-j)\frac{\delta}{\Lambda}\left(1+\frac{\gamma-1}{\sqrt{N_{pr}}}\right)\right], \tag{193}$$

with c_0 the speed of sound in free air. As the value for Λ the tube radius is taken. This wave number k is taken into account in the acoustic domain of the problem.

In this numerical example, the influence of two different ways of mounting the sample in the tube is compared. In a first set-up, the sample is free to slide along the wall of the tube, applying sliding edge boundary conditions (86). In a second set-up, the sample is glued to the side wall, applying fixed boundary conditions (85).

Figures 19 and 20 show contour plots of the displacement field $u_z^s(\mathbf{r})$ and the acoustic stress field $\sigma^f(\mathbf{r})$ within the poroelastic domain obtained with the WBM. The (a) figures show the results for a poroelastic sample which is allowed to slide along the side wall of the tube, applying mixed boundary conditions, and the (b) figures show the same dynamic variables obtained for a fixed sample. The figures show that for the sliding edge boundary conditions a perfect 1D behaviour is obtained. This is to be expected, since the shear wave is not excited. For this simple set-up analytical formulas could be employed to predict the dynamic fields. For the second setup, a more complex behaviour is obtained.

By calculating the absorption coefficient α, the influence of different boundary conditions can be verified. The absorption coefficient is given by:

$$\alpha = 1 - |R|^2, \tag{194}$$

with R the reflection coefficient. The reflection coefficient is calculated using the obtained pressure field $p(p_1)$ and $p(p_2)$ at the microphone locations [168]:

$$R = \frac{e^{jkd_1} - e^{jkd_2} p(p_1)/p(p_2)}{e^{-jkd_2} p(p_1)/p(p_2) - e^{-jkd_1}}, \tag{195}$$

with d_1 and d_2 the distances from the poroelastic-acoustic interface to the microphone positions p_1 and p_2, respectively. Figure 21 shows the absorption coefficient obtained with the WBM and the FEM for both configurations of boundary conditions and for a frequency range between 250Hz and 5000Hz in steps of 25Hz. In case sliding edge boundary conditions are applied, the absorption coefficient can be exactly calculated [23]. The exact absorption curve is also shown in Figure 21(a).

The effect of the presence of the shear wave is clear when comparing Figure 21(a) and Figure 21(b), indicating the importance of the mounting conditions. The shear wave is not present when sliding edge boundary conditions are imposed. The effect of imposing fixed edge boundary conditions is that the sample exhibits a stiffer behaviour, shifting the peak in the absorption curve related to a resonance in the poroelastic material towards higher frequencies. The obtained results are in good agreement with the results obtained by Vigran et al. [167], indicating the possibility of the method to predict/evaluate measurement outcomes.

5.1.7 Stress singularities in poroelastic domains

As indicated by Vanmaele [155] for structural dynamic problems, the accuracy of the WBM deteriorates when singularities are present in the dynamic fields. These problems originate from the fact that the wave functions are smooth and have difficulties capturing local steep gradients. As indicated by Sinclair [169], infinite values of stresses are physically impossible, but indicate that no finite stresses can be computed by the linear theory of elasticity. Three types of linearization are made in the classical elasticity: the relationship between stresses and strains are linear, the strains depend linearly on the displacement gradients and the deflections are small. Singularities violate all three of these assumptions. Nevertheless they comply with all of the field equations. Due to the simplification of the governing equations, compliance with the assumptions becomes unpoliced by the theory itself.

In general, two classes of singularities can be distinguished. The first class originates from concentrated loads applied over regions with a vanishingly small area, which typically leads to non-homogenous Helmholtz equations and a particular solution is necessary. The second class considers singularities that originate from discontinuities. It is this second class that we consider here. Discontinuity singularities can be expected at the corner points. Typically, this kind of singularity arises when the internal angle formed by the two sides of a corner exceeds a critical value, which depends on the imposed boundary conditions.

Vanmaele proposed the use of special purpose enrichment functions, also called corner functions (CF), to account for the singular behaviour in the vicinity of a corner for structural dynamic problems [155]. By adding these corner functions to the regular wave function sets, convergence problems were remedied. Since a poroelastic material consists of both a solid and a fluid phase, it is expected that singularities can arise in variables related to the solid phase and in variables related to the fluid phase. This section briefly summarises the work on stress singularities on poroelastic materials, without going into details.

Analytical solutions are sought which asymptotically describe the dynamic fields in the near vicinity of a corner. The aim of an asymptotic analysis is twofold: (i) a criterion can be defined to determine when singularities will be present, and (ii) enrichment functions which accurately represent the singular behaviour close to the corner point can be identified. For the asymptotic analysis, a 2D infinite wedge domain is studied, as shown in Figure 22. The solutions of the infinite wedge domain only exactly describe the dynamic fields when the

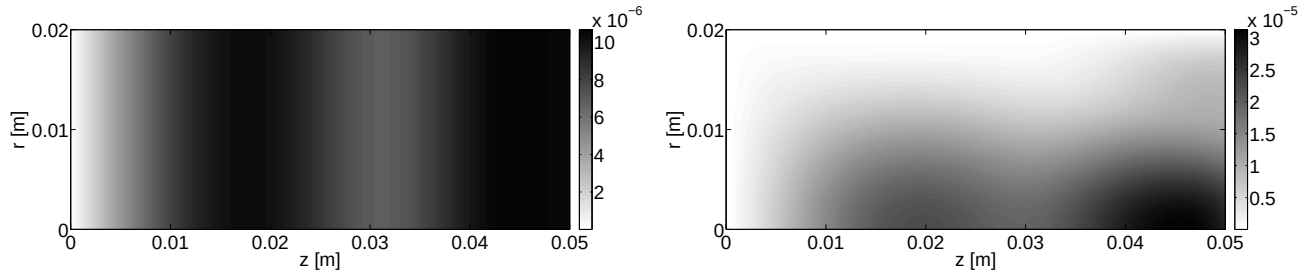

(a) Sliding edge boundary conditions (b) Fixed edge boundary conditions

Fig. 19 Contour of the amplitude of $u_z^s(\mathbf{r})$ [m] at 2500Hz with two different types of boundary conditions.

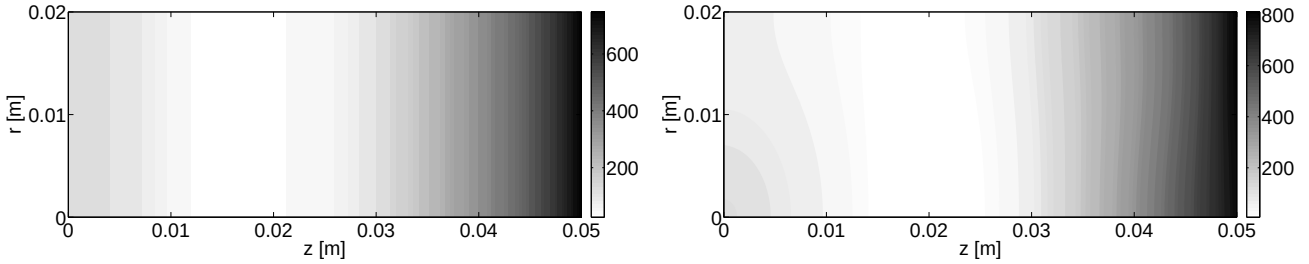

(a) Sliding edge boundary conditions (b) Fixed edge boundary conditions

Fig. 20 Contour of the amplitude of $\sigma^f(\mathbf{r})$ [Pa] at 2500Hz with two different types of boundary conditions.

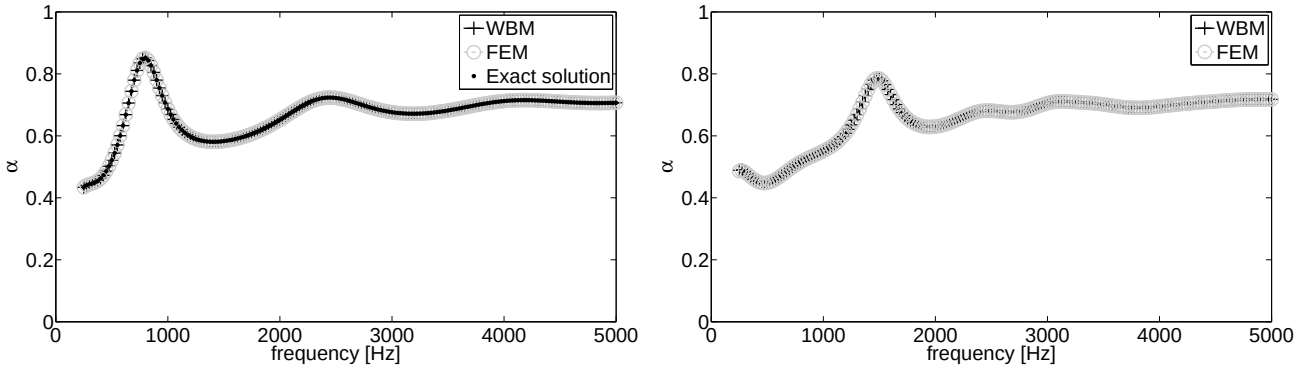

(a) Sliding edge boundary condition (b) Fixed edge boundary condition

Fig. 21 Absorption coefficient of the porous material obtained with a Kundt tube set-up for two types of boundary conditions, as calculated with the WBM and the FEM.

edges extend to infinity. However, they present a good approximation for the actual behaviour in the vicinity of the corner of a finite problem domain as long as the same boundary conditions are imposed on both sides of the wedge as for the real finite problem.

The analytical solutions of interest need to satisfy:

A. The governing equations.
B. The imposed boundary conditions.
C. The regularity requirements at the vertex.

In [157] the mathematical derivation of the analytical solutions is given. It is shown that exact solutions fulfilling the Biot equations and the boundary conditions can only be found when sliding edge boundary conditions are imposed on both sides of the wedge. It can be concluded that for this combination of boundary conditions, stress singularities are present in the solid phase of the material if the internal angle is larger than 90°. An analytical description of the dynamic fields in the vicinity of a singular corner is given. Although not discussed in that paper, additionally, singularities in the fluid displacement fields exist for sliding edge boundary conditions when the internal angle is larger than 180° [170].

An important remark when applying special purpose enrichment functions within the WBM, is that they do not form a Trefftz-complete set. Consequently, by only using corner functions in the wave function set, the convergence towards the exact solution of the

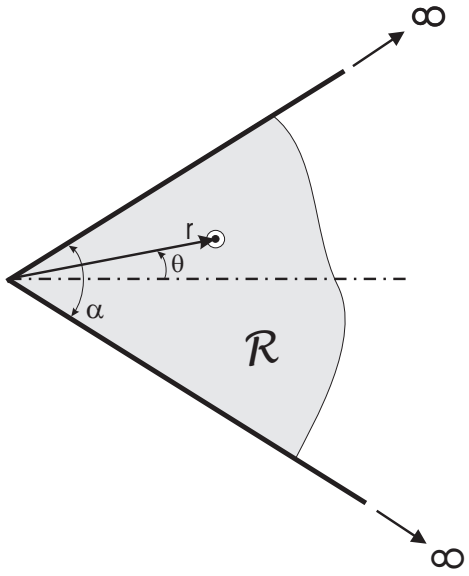

Fig. 22 2D infinite wedge domain.

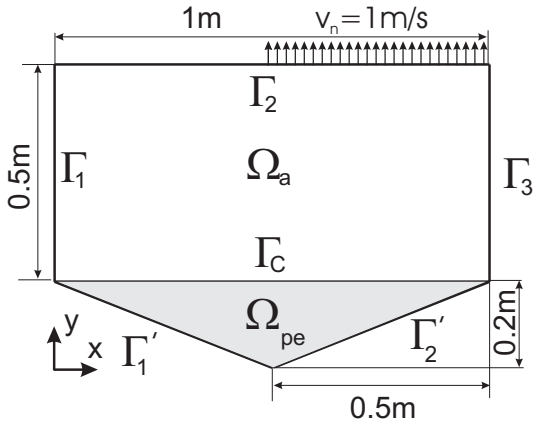

Fig. 23 Problem geometry of a rectangular air cavity coupled with a triangular poroelastic domain

problem is not ensured. As such, corner functions can only be used in combination with the conventional set of wave functions. For each corner of the problem domain where a singularity exists, a set of corner functions will be added to the field variable expansion of the bounded subdomain(s) to which the corner belongs. Unlike wave functions, corner functions are not necessarily restricted to one subdomain. Similarly as for regular wave functions the same corner functions are also applied as weighting functions.

Assessment of the beneficial effect of corner functions
To show the adverse effect of singularities and the beneficial effect of corner functions, the problem setting shown in Figure 23 is considered. The problem geometry consists of a 2D rectangular acoustic subdomain Ω_a, containing air, and a triangular poroelastic subdomain Ω^{pe} consisting of a polyurethane foam. The material properties of both subdomains are given in Appendix A. Boundaries Γ_1, Γ_3 and the left half side of Γ_2 are rigid boundaries, equation (44) with $\bar{v}_n = 0$. On the right hand side of Γ_2 a normal velocity with amplitude 1m/s is imposed, exciting the acoustic cavity. On the coupling edge Γ_C, the coupling conditions (87) are imposed. The edges Γ_1' and Γ_2' of the poroelastic domain are sliding edges with imposed conditions (86). Stress singularities exist in the bottom corner of the poroelastic domain as it is larger than 90°.

To illustrate the beneficial effect of corner functions and the adverse effect of singularities, Figure 24 shows contour plots of the predicted shear stress field $\sigma^s_{xy}(x, y)$ at 200Hz calculated with the WBM. In Figure 24(a) only the regular wave functions are used in the wave function expansion while in Figure 24(b) the same number of wave functions have been used and three special purpose enrichment functions have been added. By adding the appropriate enrichment functions, the accuracy and the stability of the WBM are clearly improved. In order to more clearly illustrate the adverse effect of the singular corner on the WB predictions in the whole poroelastic field, twelve contour lines between $1N/m^2$ and $46N/m^2$ are added to the figures. These lines clearly show the presence of irregularities in the WBM prediction which do not appear when adding the three special purpose enrichment functions. As shown in [157], also the convergence improves by adding these special purpose enrichment functions. In general, the convergence rate and the stability is improved, while only a small increase of computational effort is incurred.

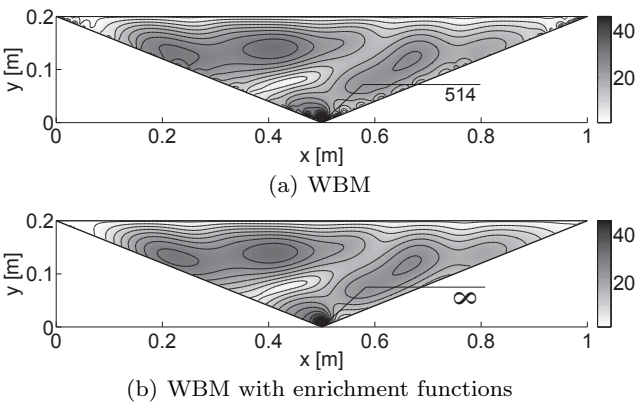

(a) WBM

(b) WBM with enrichment functions

Fig. 24 Predicted stress field $\sigma^s_{xy}(x, y)[N/m^2]$ at 200 Hz.

5.2 Hybrid models

As discussed earlier, the FEM and the WBM have their own specific strengths and weaknesses through their fundamental differences in modelling approach.

The FEM is a very flexible technique, capable of tackling very complex geometries. However, with increasing frequency, the computational efficiency strongly deteriorates through interpolation and pollution errors [6–8]. These errors are inherent to the polynomial approximation functions used. The WBM, on the other hand, makes use of wave functions which are exact solutions to the governing differential equation and therefore does not introduce errors when representing the field. Often a low number of wave functions is sufficient to accurately capture the field, leading to a high efficiency. The system matrices are per definition complex valued and frequency dependent. Therefore, the introduction of frequency dependent material parameters does not affect the performance. Nevertheless, the geometrical flexibility is limited.

This section of the paper treats the details of the hybrid FE-WBM for trimmed vibro-acoustic problems, combining the poroelastic FEM and the acoustic WBM in a fully coupled model. Subsection 5.2.1 motivates the development of this hybrid approach. Thereafter, in subsection 5.2.2, the coupling terms for the hybrid system of equations are derived, both for the ($\mathbf{u^s}$,$\mathbf{u^f}$)- and for the ($\mathbf{u^s}$,p^f)-formulation. The efficiency and accuracy of the approach are illustrated by means of two numerical examples.

5.2.1 Motivation

In many industrial vibro-acoustic applications, a trim layer consists of a multitude of very thin, stacked layers, often with inclusions or stiffeners, thus requiring a geometrically flexible technique. Problem geometries like these are the strength of the FEM.

The surrounding acoustic cavity, however, is often geometrically quite simple. Moreover, the dissipation mechanisms in the coupled system, which have evanescent waves with a high decay rate and hence very local effects, require additional mesh refinements in the acoustic FE model. This leads the coupled acoustic models to be even more refined than the uncoupled ones. In practical applications even longer calculation times are needed as a result. The WB solution expansion by definition contains evanescent wave functions which can capture these near-field effects. Furthermore, the acoustic FE model, which typically can be decomposed into frequency independent submatrices, loses its efficiency because of the frequency dependent and complex valued material properties of the trim. The system matrix for the WBM is inherently frequency dependent, complex valued and cannot be decomposed into frequency independent matrices. Therefore, the coupling to a material with frequency dependent damping phenomena does not impair the method's performance, contrarily to the acoustic FEM, where the computational effort substantially increases.

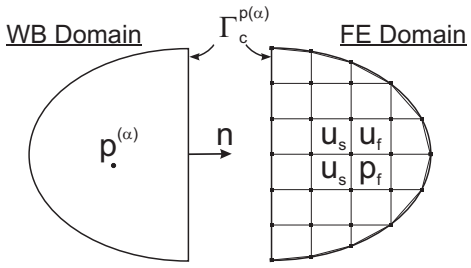

Fig. 25 Direct hybrid FE-WBM coupling approach.

The hybrid FE-WB approach is thus a best-of-two-worlds strategy for problems involving acoustic cavities and localised damping layers; the FEM covers the complexly layered trim, while the efficiency of the WBM is exploited in the acoustic domain.

5.2.2 Direct hybrid coupling strategy

By using a direct coupling strategy (see Figure 25), the mutual interactions between the acoustic cavity and the poroelastic material can be directly introduced into the weighted residual formulations and thus into the uncoupled systems of equations (96)-(149). This way, the coupling does not introduce additional variables (e.g. Lagrange Multipliers [171]) and the coupling terms are easy to interpret since they have a physical meaning.

The coupling terms are derived from the mathematical formulation of the acoustic/poroelastic interaction (87) by using a weighted residual Galerkin approach. The field variables and weighting functions are derived from the expansion for the WBM (145)-(148) and for the FEM (92) and (95) and read:

$$\begin{cases} p^a(\mathbf{r}) = \mathbf{\Phi}_\mathbf{a}^{(\alpha)}(\mathbf{r})\mathbf{u}_\mathbf{a}^{(\alpha)} + \hat{u}_{p,a}^{(\alpha)}(\mathbf{r}) \\ \tilde{p}^a(\mathbf{r}) = \mathbf{\Phi}_\mathbf{a}^{(\alpha)}(\mathbf{r})\tilde{\mathbf{u}}_\mathbf{a}^{(\alpha)} \end{cases}, \tag{196}$$

$$\begin{cases} \mathbf{u^s}(\mathbf{r}) = \mathbf{N}_{\mathbf{u_s}}(\mathbf{r})\mathbf{u_s} \\ \tilde{\mathbf{u}}^\mathbf{s}(\mathbf{r}) = \mathbf{N}_{\mathbf{u_s}}(\mathbf{r})\tilde{\mathbf{u}}_\mathbf{s} \end{cases}, \tag{197}$$

$$\begin{cases} \mathbf{u^f}(\mathbf{r}) = \mathbf{N}_{\mathbf{u_f}}(\mathbf{r})\mathbf{u_f} \\ \tilde{\mathbf{u}}^\mathbf{f}(\mathbf{r}) = \mathbf{N}_{\mathbf{u_f}}(\mathbf{r})\tilde{\mathbf{u}}_\mathbf{f} \end{cases}, \tag{198}$$

$$\begin{cases} p^f(\mathbf{r}) = \mathbf{N}_{\mathbf{p_f}}(\mathbf{r})\mathbf{p_f} \\ \tilde{p}^f(\mathbf{r}) = \mathbf{N}_{\mathbf{p_f}}(\mathbf{r})\tilde{\mathbf{p}}_\mathbf{f} \end{cases}. \tag{199}$$

The derived coupling terms differ for the two presented formulations and are therefore treated separately.

Note that for the ease of notation, the spatial ($\mathbf{r}$)-dependency of all field variables, error residuals, shape functions, wave functions and particular solution terms is omitted in the remainder of this subsection.

5.2.3 Hybrid ($\mathbf{u^s}$,$\mathbf{u^f}$) *FE-WBM*

On the coupling interface between the acoustic WB model and the poroelastic FE model, the coupling conditions (87) have to be imposed. Considering the ($\mathbf{u^s}$,$\mathbf{u^f}$)-formulation, the weak integral form is given in [83] and contains the following two boundary integrals:

$$-\int_{\Gamma_C^{pa}} \tilde{\mathbf{u}}^{\mathbf{s}} \left[\boldsymbol{\sigma}^{\boldsymbol{s}}.\mathbf{n}\right] d\Gamma, \tag{200}$$

$$-\int_{\Gamma_C^{pa}} \tilde{\mathbf{u}}^{\mathbf{f}} \left[\boldsymbol{\sigma}^{\boldsymbol{f}}.\mathbf{n}\right] d\Gamma. \tag{201}$$

Consequently, it is a natural choice to impose the first two coupling coupling conditions in (87), expressing the equilibrium of stresses on the interface, on the FE part. The fourth condition, the continuity of the normal volume velocity, is imposed on the WB part, leading to the weighted boundary residual:

$$\begin{aligned}\int_{\Gamma_C^{pa}} \tilde{p}^a R_u^{pa} d\Gamma = \int_{\Gamma_C^{pa}} \tilde{p}^a \left[\mathcal{L}_v(p^a)\right. \\ \left. -j\omega\left[(1-\phi)u_n^s + \phi u_n^f\right]\right] d\Gamma.\end{aligned} \tag{202}$$

The three resulting boundary integrals (200)-(202) are discussed below:

- $-\int_{\Gamma_C^{pa}} \tilde{\mathbf{u}}^{\mathbf{s}}[\boldsymbol{\sigma}^{\boldsymbol{s}}.\mathbf{n}]d\Gamma$ – By considering the second condition of (87), it is clear that the integral involving the shear stress components vanishes. By using the second condition of (87) and expanding the expression for the distributed loading on the solid phase in terms of the WB wave functions and the FE shape functions, the weighted residual formulation for the solid phase is extended with the following term:

$$\begin{aligned}&-\int_{\Gamma_C^{pa}} \tilde{\mathbf{u}}^{\mathbf{s}}[\boldsymbol{\sigma}^{\boldsymbol{s}}.\mathbf{n}]d\Gamma \\ &\quad= \int_{\Gamma_C^{p(\alpha)}} (1-\phi)\, \tilde{u}_n^s p^a d\Gamma, \\ &\quad= \tilde{\mathbf{u}}_{\mathbf{sn}}^T \left[\int_{\Gamma_C^{p(\alpha)}} (1-\phi)\, \mathbf{N_{u_s}}^T \boldsymbol{\Phi}_{\mathbf{a}}^{(\alpha)} \mathbf{u}_{\mathbf{a}}^{(\alpha)} d\Gamma\right. \\ &\qquad \left. + \int_{\Gamma_C^{p(\alpha)}} (1-\phi)\, \mathbf{N_{u_s}}^T \hat{u}_{p,a}^{(\alpha)} d\Gamma\right], \\ &\quad= \tilde{\mathbf{u}}_{\mathbf{sn}}^T \left[-\mathbf{C}_{\mathbf{sa}}^{\mathbf{uu}} \mathbf{u}_{\mathbf{a}}^{(\alpha)} + \mathbf{c}_{\mathbf{sa}}^{\mathbf{uu}}\right],\end{aligned} \tag{203}$$

  with $\Gamma_C^{p(\alpha)} = \partial\Omega^p \cap \partial\Omega^{(\alpha)}$ being the interaction surface between the poroelastic medium and the WBM domain $\Omega^{(\alpha)}$.

- $-\int_{\Gamma_C^{pa}} \tilde{\mathbf{u}}^{\mathbf{f}} \left[\boldsymbol{\sigma}^{\boldsymbol{f}}.\mathbf{n}\right] d\Gamma$. – Analogously to the solid phase (203), the weighted residual formulation of the fluid phase is extended with a distributed loading term using the third condition of (87):

$$\begin{aligned}&-\int_{\Gamma_C^{pa}} \tilde{\mathbf{u}}^{\mathbf{f}} \left[\boldsymbol{\sigma}^{\boldsymbol{f}}.\mathbf{n}\right] d\Gamma \\ &\quad= \int_{\Gamma_C^{p(\alpha)}} \phi \tilde{u}_n^f p^a d\Gamma, \\ &\quad= \tilde{\mathbf{u}}_{\mathbf{fn}}^T \left[\int_{\Gamma_C^{p(\alpha)}} \phi \mathbf{N_{u_f}}^T \boldsymbol{\Phi}_{\mathbf{a}}^{(\alpha)} \mathbf{u}_{\mathbf{a}}^{(\alpha)} d\Gamma\right. \\ &\qquad \left. + \int_{\Gamma_C^{p(\alpha)}} \phi \mathbf{N_{u_f}}^T \hat{u}_{p,a}^{(\alpha)} d\Gamma\right], \\ &\quad= \tilde{\mathbf{u}}_{\mathbf{fn}}^T \left[-\mathbf{C}_{\mathbf{fa}}^{\mathbf{uu}} \mathbf{u}_{\mathbf{a}}^{(\alpha)} + \mathbf{c}_{\mathbf{fa}}^{\mathbf{uu}}\right].\end{aligned} \tag{204}$$

- $\int_{\Gamma_C^{p(\alpha)}} \tilde{p}^a \left[\mathcal{L}_v(p^a) - j\omega\left[(1-\phi)u_n^s + \phi u_n^f\right]\right] d\Gamma$ – The continuity between the out-of-plane deformation and the normal acoustic particle displacement leads to the final contributions to the coupled system of equations:

$$\begin{aligned}&\int_{\Gamma_C^{p(\alpha)}} \tilde{p}^a \left[\mathcal{L}_v(p^a)\right. \\ &\qquad \left. - j\omega\left[(1-\phi)u_n^s + \phi u_n^f\right]\right] d\Gamma \\ &\quad= \tilde{\mathbf{u}}_{\mathbf{a}}^{(\alpha)^T} \left[\int_{\Gamma_C^{p(\alpha)}} \boldsymbol{\Phi}_{\mathbf{a}}^{(\alpha)^T} \mathcal{L}_v(\boldsymbol{\Phi}_{\mathbf{a}}^{(\alpha)}) \mathbf{u}_{\mathbf{a}}^{(\alpha)} d\Gamma\right. \\ &\qquad + \int_{\Gamma_C^{p(\alpha)}} \boldsymbol{\Phi}_{\mathbf{a}}^{(\alpha)^T} \mathcal{L}_v(\hat{u}_{p,a}^{(\alpha)}) d\Gamma \\ &\qquad - j\omega \int_{\Gamma_C^{p(\alpha)}} (1-\phi) \boldsymbol{\Phi}_{\mathbf{a}}^{(\alpha)^T} \mathbf{N}_{\mathbf{u_s}} \mathbf{u}_{\mathbf{sn}} d\Gamma \\ &\qquad \left. - j\omega \int_{\Gamma_C^{p(\alpha)}} \phi \boldsymbol{\Phi}_{\mathbf{a}}^{(\alpha)^T} \mathbf{N}_{\mathbf{u_f}} \mathbf{u}_{\mathbf{fn}} d\Gamma\right], \\ &\quad= \tilde{\mathbf{u}}_{\mathbf{a}}^{(\alpha)^T} \left[\mathbf{C}_{\mathbf{aa}}^{\mathbf{uu}} \mathbf{u}_{\mathbf{a}}^{(\alpha)} - \mathbf{c}_{\mathbf{aa}}^{\mathbf{uu}}\right. \\ &\qquad \left. + j\omega \mathbf{C}_{\mathbf{sa}}^{\mathbf{uu}^T} \mathbf{u_s} + j\omega \mathbf{C}_{\mathbf{fa}}^{\mathbf{uu}^T} \mathbf{u_f}\right].\end{aligned} \tag{205}$$

These relations should hold for any weighting function $\tilde{\mathbf{u}}_{\mathbf{a}}^{(\alpha)}$, $\tilde{\mathbf{u}}_{\mathbf{sn}}$ or $\tilde{\mathbf{u}}_{\mathbf{fn}}$. Therefore, only the expressions between brackets are introduced into the coupled system of equations in terms of wave function contribution factors $\mathbf{u_a}$ and the nodal values for the displacement fields $\mathbf{u_s}$ and $\mathbf{u_f}$, in the solid and the fluid phase, respectively:

$$\begin{bmatrix} \mathbf{A_{aa}} + \mathbf{C}_{\mathbf{aa}}^{\mathbf{uu}} & j\omega \mathbf{C}_{\mathbf{sa}}^{\mathbf{uu}^T} & j\omega \mathbf{C}_{\mathbf{fa}}^{\mathbf{uu}^T} \\ \mathbf{C}_{\mathbf{sa}}^{\mathbf{uu}} & \mathbf{D}_{\mathbf{ss}}^{\mathbf{uu}} & \mathbf{D}_{\mathbf{sf}}^{\mathbf{uu}} \\ \mathbf{C}_{\mathbf{fa}}^{\mathbf{uu}} & \mathbf{D}_{\mathbf{fs}}^{\mathbf{uu}} & \mathbf{D}_{\mathbf{ff}}^{\mathbf{uu}} \end{bmatrix} \begin{bmatrix} \mathbf{u_a} \\ \mathbf{u_s} \\ \mathbf{u_f} \end{bmatrix} = \begin{bmatrix} \mathbf{b_a} + \mathbf{c}_{\mathbf{aa}}^{\mathbf{uu}} \\ \mathbf{f_s}^{\mathbf{uu}} + \mathbf{c}_{\mathbf{sa}}^{\mathbf{uu}} \\ \mathbf{f_f}^{\mathbf{uu}} + \mathbf{c}_{\mathbf{fa}}^{\mathbf{uu}} \end{bmatrix}, \tag{206}$$

where $\mathbf{A_{aa}}$ and $\mathbf{b_a}$ represent the uncoupled WBM system matrices, $\mathbf{D_\bullet^{uu}}$ and $\mathbf{f_\bullet^{uu}}$ are the uncoupled FEM system matrices and $\mathbf{C_\bullet^{uu}}$ and $\mathbf{c_\bullet^{uu}}$ are the mutual coupling matrices.

5.2.4 Hybrid ($\mathbf{u^s}$,p^f) *FE-WBM*

When using the ($\mathbf{u^s}$,p^f)-formulation for the poroelastic FE model, the coupling is again made directly through the boundary integrals of the FEM and the boundary residuals of the WBM. The weak integral form is given in [88] and contains the following two boundary integrals:

$$-\int_{\Gamma_C^{pa}} \tilde{\mathbf{u}}^{\mathbf{s}} \left[\boldsymbol{\sigma}^t.\mathbf{n}\right] d\Gamma, \tag{207}$$

$$-\int_{\Gamma_C^{pa}} \tilde{p}^f \left[\phi\left(u_n^f - u_n^s\right)\right] d\Gamma, \tag{208}$$

On the WB model, the following residual applies:

$$\int_{\Gamma_C^{pa}} \tilde{p}^a \frac{1}{j\omega} R_u^{pa} d\Gamma = \int_{\Gamma_C^{pa}} \tilde{p}^a \left[\frac{1}{j\omega}\mathcal{L}_v(p^a) - \left[(1-\phi)u_n^s + \phi u_n^f\right]\right] d\Gamma. \tag{209}$$

Note that the WBM residuals have been orthogonalised on a pressure-displacement-basis (as is done in the internal poroelastic coupling between the solid and fluid phase), instead of pressure-velocity, as was done so far in the WBM [146]. This choice will become clear below. Moreover, the equivalence dynamic equilibrium conditions for the fluid phase (87) should hold:

$$\sigma_f + \phi p^a = p^a - p^f = 0, \tag{210}$$

which is in a pure FE model satisfied through the assembly.

Equation (209) contains a normal gradient of the fluid phase pressure p^f inside the term u_n^f (105). Imposing this results in a loss of accuracy over the interface, since the polynomial shape functions of the FE submodel have to be spatially derived.

The substitution of (210) into the weighting functions $\tilde{p}^a$ of equation (209) and the combination with (208) reveals the opportunity to eliminate the first two of three resulting integrals:

$$\begin{aligned} &-\int_{\Gamma_C^{pa}} \tilde{p}^f \left[\phi\left(u_n^f - u_n^s\right)\right] d\Gamma \\ &\quad + \int_{\Gamma_C^{pa}} \tilde{p}^f \left[\phi\left(u_n^f - u_n^s\right)\right] d\Gamma \\ &\quad + \int_{\Gamma_C^{pa}} \tilde{p}^f \left[\frac{1}{j\omega}\mathcal{L}_v(p^a) - u_n^s\right] d\Gamma. \end{aligned} \tag{211}$$

Consequently, the coupling conditions do not contain terms with u_n^f anymore. This leaves coupling condition (210) to be imposed. As indicated before, in a pure FEM procedure, this would be enforced during matrix assembly, since both acoustic and fluid phase pressure are primary variables [88]. In a hybrid context, however, this *a priori* elimination is not possible due to the indirect nature of the WBM. Therefore, the pressure continuity is enforced on the WB model:

$$\int_{\Gamma_C^{p(\alpha)}} \tilde{u}_n^a \left(p^a - p^f\right) d\Gamma. \tag{212}$$

Equations (207), (211) and (212) lead to following coupling terms between an acoustic WB model and a poroelastic FE model using the ($\mathbf{u^s}$,p^f)-formulation:

$-\int_{\Gamma_C^{pa}} \tilde{\mathbf{u}}^{\mathbf{s}} \left[\boldsymbol{\sigma}^t.\mathbf{n}\right] d\Gamma$ – On the interface, the shear stress components should again be zero and the normal component of the total stress σ_n^t should be equal to $-p^a$. By expanding the expression for the distributed loading of the solid phase in terms of the wave function and shape function expansions, the right hand side of the original weighted residual formulation for the solid phase is extended with the following term:

$$\begin{aligned} &-\int_{\Gamma_C^{pa}} \tilde{\mathbf{u}}^{\mathbf{s}} \left[\boldsymbol{\sigma}^t.\mathbf{n}\right] d\Gamma \\ &\quad = \int_{\Gamma_C^{p(\alpha)}} \tilde{u}_n^s p^a d\Gamma, \\ &\quad = \tilde{\mathbf{u}}_{\mathbf{sn}}^T \left[\int_{\Gamma_C^{p(\alpha)}} \mathbf{N_{u_s}}^T \boldsymbol{\Phi}_{\mathbf{a}}^{(\alpha)} \mathbf{u}_{\mathbf{a}}^{(\alpha)} d\Gamma + \int_{\Gamma_C^{p(\alpha)}} \mathbf{N_{u_s}}^T \hat{u}_{p,a}^{(\alpha)} d\Gamma\right], \\ &\quad = \tilde{\mathbf{u}}_{\mathbf{sn}}^T \left[-\mathbf{C}_{\mathbf{sa}}^{\mathbf{up}} \mathbf{u}_{\mathbf{a}}^{(\alpha)} + \mathbf{c}_{\mathbf{sa}}^{\mathbf{up}}\right]. \end{aligned} \tag{213}$$

$\int_{\Gamma_C^{pa}} \tilde{p}^f \left[\frac{1}{j\omega}\mathcal{L}_v(p^a) - u_n^s\right] d\Gamma$ – The continuity between the out-of-plane deformation and the normal acoustic particle displacement leads to the final

contributions to the coupled system equations:

$$\begin{aligned}
&\int_{\Gamma_C^{p(\alpha)}} \tilde{p}^f \left[\frac{1}{j\omega}\mathcal{L}_v(p^a) - u_n^s\right] d\Gamma, \\
&\quad = \tilde{\mathbf{p}}_\mathbf{f}^T \left[\int_{\Gamma_C^{p(\alpha)}} \frac{1}{j\omega} {\mathbf{N}_{\mathbf{p_f}}}^T \mathcal{L}_v(\mathbf{\Phi}_\mathbf{a}^{(\alpha)})\mathbf{u}_\mathbf{a}^{(\alpha)} d\Gamma \right. \\
&\qquad + \int_{\Gamma_C^{p(\alpha)}} \frac{1}{j\omega} {\mathbf{N}_{\mathbf{p_f}}}^T \mathcal{L}_v(\hat{u}_{p,a}^{(\alpha)}) d\Gamma \\
&\qquad \left. - \int_{\Gamma_C^{p(\alpha)}} {\mathbf{N}_{\mathbf{p_f}}}^T \mathbf{N}_{\mathbf{u_s}} \mathbf{u_{sn}} d\Gamma \right], \\
&\quad = \tilde{\mathbf{p}}_\mathbf{f}^T \left[\mathbf{C}_\mathbf{fa}^\mathbf{up} \mathbf{u}_\mathbf{a}^{(\alpha)} - \mathbf{c}_\mathbf{fa}^\mathbf{up} + \mathbf{B}_\mathbf{fa}^\mathbf{up} \mathbf{u_s}\right].
\end{aligned} \tag{214}$$

$\int_{\Gamma_C^{p(\alpha)}} \tilde{u}_n^a \left(p^a - p^f\right) d\Gamma$ – The pressure continuity between the fluid phase and the acoustic cavity gives:

$$\begin{aligned}
&\int_{\Gamma_C^{p(\alpha)}} \tilde{u}_n^a \left(p^a - p^f\right) d\Gamma \\
&\quad = \tilde{\mathbf{u}}_\mathbf{a}^T \left[\int_{\Gamma_C^{p(\alpha)}} \frac{1}{j\omega} \mathcal{L}_v(\mathbf{\Phi}_\mathbf{a}^{(\alpha)})^T \mathbf{\Phi}_\mathbf{a}^{(\alpha)} \mathbf{u}_\mathbf{a}^{(\alpha)} d\Gamma \right. \\
&\qquad + \int_{\Gamma_C^{p(\alpha)}} \frac{1}{j\omega} \mathcal{L}_v(\mathbf{\Phi}_\mathbf{a}^{(\alpha)})^T \hat{u}_{p,a}^{(\alpha)} d\Gamma \\
&\qquad \left. - \int_{\Gamma_C^{p(\alpha)}} \frac{1}{j\omega} \mathcal{L}_v(\mathbf{\Phi}_\mathbf{a}^{(\alpha)})^T \mathbf{N}_{\mathbf{p_f}} \mathbf{p_f} d\Gamma \right], \\
&\quad = \tilde{\mathbf{u}}_\mathbf{a}^T \left[\mathbf{C}_\mathbf{aa}^\mathbf{up} \mathbf{u}_\mathbf{a}^{(\alpha)} - \mathbf{c}_\mathbf{aa}^\mathbf{up} + \mathbf{C}_\mathbf{af}^\mathbf{up} \mathbf{p_f}\right].
\end{aligned} \tag{215}$$

These relations should hold for any weighting function $\tilde{\mathbf{u}}_\mathbf{a}^{(\alpha)}$, $\tilde{\mathbf{u}}_\mathbf{sn}$ or $\tilde{\mathbf{p}}_\mathbf{f}$. Therefore, only the expressions between brackets are introduced into the coupled system of equations in terms of the wave function contribution factors $\mathbf{u_a}$ and the nodal values for the solid phase displacement field $\mathbf{u_s}$ and the fluid phase pressure distribution $\mathbf{p_f}$:

$$\begin{bmatrix} \mathbf{A_{aa}} + \mathbf{C_{aa}^{up}} & \mathbf{0} & \mathbf{C_{af}^{up}} \\ \mathbf{C_{sa}^{up}} & \mathbf{D_{ss}^{up}} & \mathbf{D_{sf}^{up}} \\ \mathbf{C_{fa}^{up}} & \mathbf{D_{fs}^{up}} + \mathbf{B_{fa}^{up}} & \mathbf{D_{ff}^{up}} \end{bmatrix} \begin{bmatrix} \mathbf{u_a} \\ \mathbf{u_s} \\ \mathbf{p_f} \end{bmatrix} = \begin{bmatrix} \mathbf{b_a} + \mathbf{c_{aa}^{up}} \\ \mathbf{f_s^{up}} + \mathbf{c_{sa}^{up}} \\ \mathbf{f_f^{up}} + \mathbf{c_{fa}^{up}} \end{bmatrix}. \tag{216}$$

where $\mathbf{A_{aa}}$ and $\mathbf{b_a}$ represent the uncoupled WBM system matrices, $\mathbf{D_\bullet^{up}}$ and $\mathbf{f_\bullet^{uu}}$ are the uncoupled FEM system matrices and $\mathbf{C_\bullet^{up}}$ and $\mathbf{c_\bullet^{up}}$ are the mutual coupling matrices.

Note that for the $(\mathbf{u^s}, p^f)$-approach, additional entry $\mathbf{B_{fa}^{up}}$ in the uncoupled poroelastic matrices are necessary, contrarily to the hybrid approach using the $(\mathbf{u^s}, \mathbf{u^f})$-formulation (206). The uncoupled FEM system matrices thus cannot be straightforwardly used. Normally, this does not pose a problem, since the coupling degrees of freedom are known. However, if information about for instance the weighting procedure in the FE submodel is not available when using closed source commercial software for the FEM matrix system assembly, the extra term $\mathbf{B_{fa}^{up}}$ may introduce practical difficulties.

Partitioned solution strategy As conventionally done in hybrid FE-WB models [144,172] a matrix partitioning procedure is used for the solution of a coupled system of equations in order to benefit from efficient solvers, which differ for sparse and dense matrix systems.

5.2.5 Numerical examples

This section evaluates the performance of the hybrid FE-WBM for the modelling of trimmed acoustic problems by two examples.

In a first example, the concept of both hybrid approaches is illustrated by means of a simple, cube-shaped cavity with a thick layer of poroelastic material on the bottom. In a second example, the influence of a thin multilayered poroelastic material on a convex cavity with non-parallel walls is studied. All used material properties, which are available from literature, are listed in Appendix A.

In all examples, the hybrid FE-WBM is compared with results obtained with the FEM, both in the $(\mathbf{u^s}$,$\mathbf{u^f})$- and in the $(\mathbf{u^s}$,$p^f)$-formulation. This comparison is done in terms of calculation times and accuracy. For the FEM reference models and for the hybrid FE submodels Comsol 4.1 is used. The WB routines are implemented in Matlab R2010a. For all operations with respect to the solution of sparse system matrices (pure FEM systems and hybrid FEM subsystems), Nastran 2010 is used as a solver in order to have a comparable solution time. The operations related to the solution of dense system matrices (hybrid WB subsystems) are performed using Matlab's backslash, i.e. by Gaussian elimination. All calculations are performed on a Linux-based 2.66GHz Intel Xeon system with 32 GB RAM.

Example 1: single layer in cavity with parallel walls The first example considers a rigid acoustic cavity (1m × 1m × 0.7m) with parallel walls. On the bottom of the cavity, a thick layer (thickness 0.2m) of a poroelastic Fireflex material is placed. The poroelastic layer has sliding edge boundary conditions and is acoustically excited with a symmetric boundary condition of $\overline{v} = 1$m/s on the top surface of the cavity (indicated as a black plane in Figure 26).

Because of the symmetry and the sliding edge poroelastic boundary conditions, no Poisson effects are excited and the 3D solution behaves uni-axially. An analytical solution is available. This solution serves as the reference for a full 3D solution.

Table 2 Example 1 – Model properties for the hybrid FE-WB models.

FEM						WBM	
Form.	Order	Elements		DOF $\left(\frac{\text{DOF}}{\text{thickness}}\right)$		DOF	
		3D	$\sim$ 1D	3D	$\sim$ 1D	3D	$\sim$ 1D
$(\mathbf{u^s},\mathbf{u^f})$	2	$9 \times 9 \times 8$	8	36822 (102)	34	144	2
$(\mathbf{u^s},p^f)$	2	$9 \times 9 \times 8$	8	24548 (68)	34	144	2

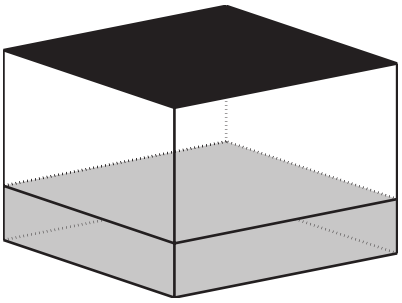

Fig. 26 Example 1 – Acoustic cavity ▭ with a velocity excitation ■ ($\overline{v} = 1$m/s) and a poroelastic Fireflex layer ▭ with sliding edge boundary conditions.

For the hybrid FE-WBM, the model properties are given in Table 2. For both the $(\mathbf{u^s}, \mathbf{u^f})$- and $(\mathbf{u^s}, p^f)$-formulation, the same mesh with quadratic elements ($9 \times 9 \times 8$) was used. Apart from the actual 3D model data, the table also gives the equivalent data if the problem would be solved in 1D with the same accuracy. In this case, the poroelastic material can be described using two scalar variables, either u^s and u^f or u^s and p^f. For a purely 1D-WB model, two propagating wave functions suffice. Figure 27 shows the absolute value of the predicted pressure field at 500Hz, obtained using three approaches: the analytical solution and the two hybrid FE-WB approaches, using the $(\mathbf{u^s},\mathbf{u^f})$- and the $(\mathbf{u^s},p^f)$-formulation with quadratic elements in the FE submodel. A good agreement can be observed. In order to assess the differences as related to the analytical model, the relative error ε on the pressure prediction is calculated as:

$$\varepsilon(\mathbf{r}) = \left| \frac{p_\bullet(\mathbf{r}) - p_{ref}(\mathbf{r})}{p_{ref}(\mathbf{r})} \right|, \tag{217}$$

where $\bullet$ represents the type of hybrid technique. The analytical solution is used as a reference.

Figure 27 also shows the relative prediction error. It shows that a good accuracy is obtained and that in this case both hybrid approaches give results of a similar accuracy. However, although only slightly visible on Figure 27, contrarily to what was shown for the pure FEM [64], the accuracy is not exactly the same for the $(\mathbf{u^s},\mathbf{u^f})$- and the $(\mathbf{u^s},p^f)$-formulation for the same discretisation. This will be indicated further in the following example.

Example 2: multilayer in cavity with non-parallel walls
The second example further demonstrates the applicability of the method on a convex cavity (1.122m $\times$ 0.82m $\times$ 0.982m) with non-parallel walls (Figure 28). The walls of the acoustic cavity are considered rigid and the cavity is excited by an acoustic volume source with an amplitude of $1\text{m}^3/\text{s}$, located in the point (1.03,0.12,0.3), indicated by the concentric circles. The air inside the cavity is in contact with a poroelastic multilayer placed at the bottom. The material properties of this multilayer are specified in Appendix A. The multilayer constists of a stack of 0.025m Fireflex on top of 0.025m carpet material. Sliding edge boundary conditions are imposed on the boundaries of the poroelastic material layers which are in contact with the cavity walls.

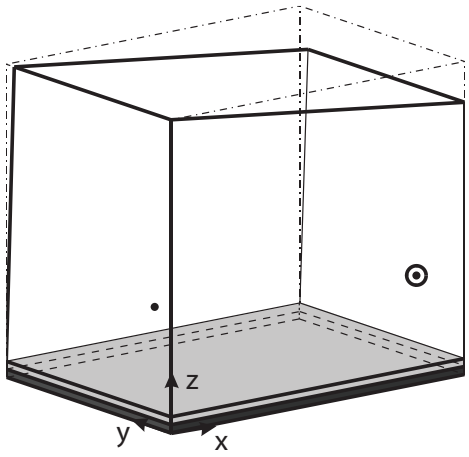

Fig. 28 Example 2 – Geometry with an acoustic cavity ▭ with a multilayer (sliding edge boundary conditions) consisting of Carpet material ■ and Fireflex ▭ excited by an acoustic volume source ⊙ with $q = 1\text{m}^3/\text{s}$.
The post-processing point for the frequency response is indicated by •.

The first validation for this problem case considers the frequency response of the acoustic pressure in a response point (0.35,0.8,0.1), indicated by •, for a frequency range from 50 to 650Hz. The WB curves are obtained using 150 to 382 wave functions. Both FE submodels in the hybrid approaches use the same mesh ($8 \times 8 \times 10$ elements), which consists of 38148 poroelastic degrees of freedom for the $(\mathbf{u^s}, \mathbf{u^f})$-formulation

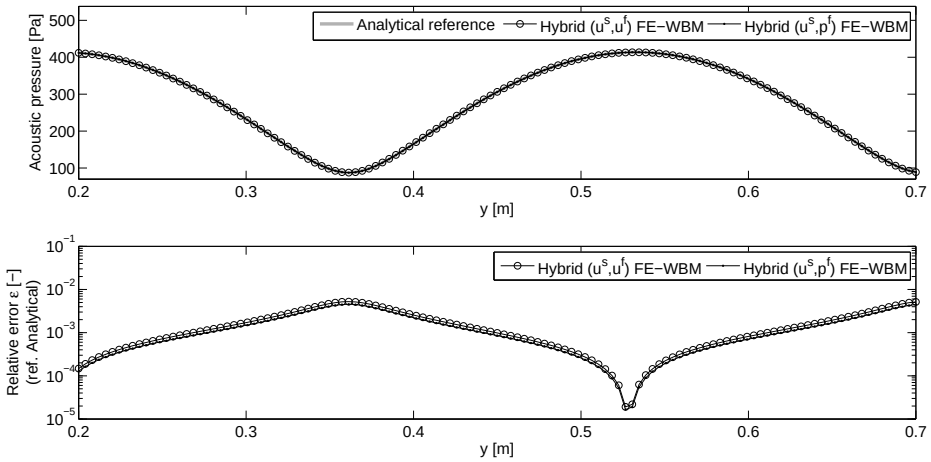

Fig. 27 Example 1 – Acoustic pressure $p^a(\mathbf{r})$ (Amplitude) [Pa] and Relative error ε [-] at 500Hz.

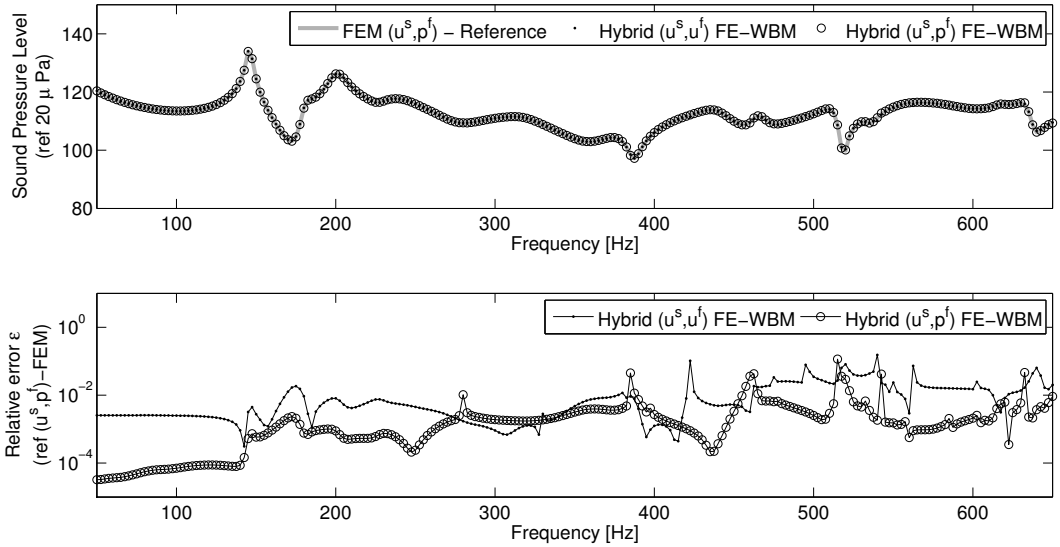

Fig. 29 Example 2 – Sound Pressure Level [dB] and relative error ε [-] for a response point at (0.35,0.80,0.10) from 50 to 650 Hz.

and 25432 for the $(\mathbf{u^s}, p^f)$-formulation. The reference FEM calculations are performed on a cubic mesh with hexahedral Lagrangian elements ($7 \times 7 \times 7$ elements in the acoustic cavity and $7 \times 7 \times 8$ elements in the poroelastic domain), resulting in a total of 10648 acoustic and 50336 poroelastic degrees of freedom, using the $(\mathbf{u^s}, p^f)$-formulation. In addition to the actual frequency response, also the error relative to the reference solution is studied. The relative error $\varepsilon(\mathbf{r_j})$ is defined in equation (217).

Figure 29 shows an excellent prediction accuracy, even with a small distance (5cm) to the near field of multilayer and to the hybrid coupling interface. This indicates that the evanescent functions in the WBM can efficiently model the near field effects caused by the presence of the trim, even though the WBM is a global technique. The figure of the relative error ε for this point further illustrates that the hybrid $(\mathbf{u^s}, \mathbf{u^f})$ FE-WBM and the hybrid $(\mathbf{u^s}, p^f)$ FE-WBM do not produce results of the same accuracy, even though the same mesh discretisation is used. For the largest part of the frequency band, the hybrid $(\mathbf{u^s}, p^f)$ FE-WBM performs best.

To further investigate this accuracy difference between formulations which is contrary to earlier studies in the pure FEM [64], and to assess the gain in efficiency, the convergence of the hybrid FE-WB approaches is studied and compared to their pure FE counterpart models with matching interface discretisations. To avoid averaging out of possible outliers, a global quadratic error estimator $< \delta >$ is defined similarly to (217):

$$< \delta >= \sqrt{\frac{\sum_{i=1}^{n} |p_\bullet(\mathbf{r_i})^2 - (p_{ref}(\mathbf{r_i}))^2|}{\sum_{i=1}^{n} |(p_{ref}(\mathbf{r_i}))^2|}}. \tag{218}$$

In this case, the acoustic pressure data at 450Hz in $n = 512$ uniformly distributed points is used. Model refinements are made both in the acoustic and in the poroelastic domain. The model properties for all FE and hybrid FE-WB models and the reference model are listed in Table 3 and Table 4.

Figure 30 compares the convergence behaviour of the hybrid FE-WB methods to that of the FEM for different refinement strategies for the (sub)model(s). To this extent, the quadratic error estimator $< \delta >$ is shown as a function of the CPU time. This CPU time is the sum of the time required for system build-up, solution and post-processing.

The curves for the pure FE models confirm earlier observations on poroelastic FE models: the accuracy of the pure FE models using the ($\mathbf{u^s}$,$\mathbf{u^f}$)- and the ($\mathbf{u^s}$,p^f)-formulation is the same for the same mesh discretisation. The required CPU time, however, is different since the ($\mathbf{u^s}$,p^f)-formulation only has 4 degrees of freedom per node whereas the ($\mathbf{u^s}$,$\mathbf{u^f}$)- has 6.

When the FE- and WB submodels are coherently refined, Figure 30(a) is obtained. This figure clearly shows the benefits of the hybrid approach. The accuracy has increased one order for a given computational cost or, for the same prediction accuracy, the computational cost has decreased one or even two orders for higher accuracies.

The convergence behaviour of hybrid FE-WBM for acoustic/poroelastic problems shows two important characteristics. Firstly, the convergence, especially for the hybrid ($\mathbf{u^s}$,$\mathbf{u^f}$) FE-WBM, is not necessarily monotonic. Secondly, in the hybrid FE-WBM, both formulations give a different accuracy, contrarily to the pure FEM.

The cause for the non-monotonic convergence behaviour can be investigated by refining one submodel while keeping the other submodel fixed. Figure 30(b) shows the convergence of the hybrid model by keeping the number of wave functions constant and by increasing the number of elements in the FE submodel. Two WB models with a constant number of wave functions – T3 and T5 – are studied while refining the FE submodel. A clear stagnation can be observed. However, for the model T5, the stagnation occurs at a lower error level than for T3, indicating that the WB submodel limits the accuracy in this case. Figure 30(c) shows the complementary curves for two constant FE discretisations Q2 and Q3. Again stagnation occurs. In this case, a higher number of wave functions makes no sense if the FE model cannot follow the increased spectral content of the WB model.

Figure 30(c) also shows that the non-monotonic convergence behaviour originates from the WBM sub-

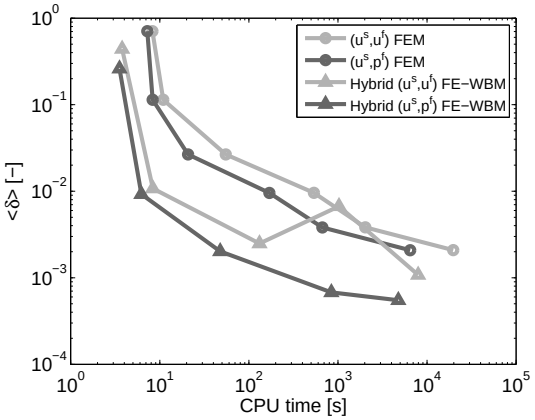

(a) Combined FE-WBM refinement

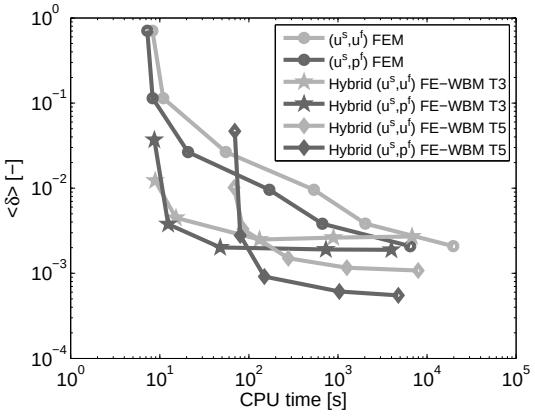

(b) FEM refinement (fixed number of wave functions)

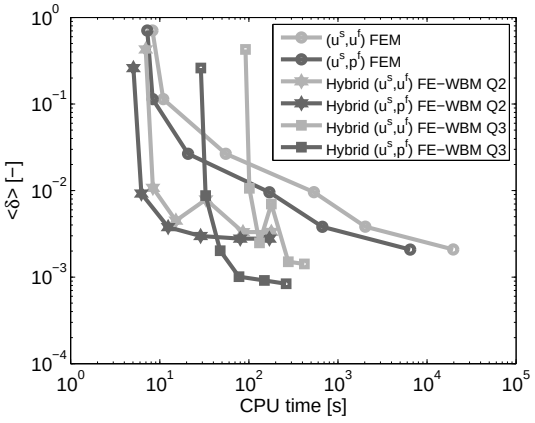

(c) WBM refinement (fixed FEM discretisation)

Fig. 30 Example 2 – Acoustic pressure $p^a(\mathbf{r})$: Relative error $< \delta >$ [−] as a function of CPU time at 450Hz.

model and its ill-conditioned system matrices. The fact that the hybrid ($\mathbf{u^s}$,p^f) FE-WBM does exhibit semi-monotonicity for this case, can be interpreted as an indication of higher stability.

The difference in accuracy for different poroelastic formulations also originates from the WBM. As an indirect Trefftz-approach, the WBM exhibits ill-

Table 3 Example 2 – Model properties for the FE models.

Discretisation				poroelastic/Acoustic DOF	
FE model	Element			$(\mathbf{u^s},\mathbf{u^f})$	$(\mathbf{u^s},p^f)$
	Order	poroelastic	Acoustic		
Q1	2	$2\times2\times2$	$2\times2\times2$	900/125	600/125
Q2	2	$4\times4\times4$	$4\times4\times4$	4860/729	3240/729
Q3	2	$6\times6\times6$	$6\times6\times6$	14196/2197	9464/2197
Q4	2	$8\times8\times8$	$8\times8\times8$	31212/4913	20808/4913
Q5	2	$10\times10\times10$	$10\times10\times10$	58212/9261	28808/9261
Q6	2	$12\times12\times12$	$12\times12\times12$	97500/15625	65000/15625
Reference	3	$7\times7\times8$	$7\times7\times7$	–	50336/10648

Table 4 Example 2 – Model properties for the hybrid FE-WB models.

Hybrid submodel	Element		Formulation	Nodal DOF (FEM) / Wave functions (WBM)
	order	poroelastic		
FEM (Q1-5)	2	see Table 3	$(\mathbf{u^s},\mathbf{u^f})$	900,4860,14196,31212,58212
FEM (Q1-5)	2	see Table 3	$(\mathbf{u^s},p^f)$	600,3240,9464,20808,38808
WBM (T1-6)	–	–	Acoustic	54,170,382,636,1006,1398

conditioned system matrices [146]. This means that the result is highly susceptible to small changes in the matrix coefficients. Although all different submodels – acoustic WB with either poroelastic $(\mathbf{u^s},\mathbf{u^f})$ or poroelastic $(\mathbf{u^s},p^f)$ – describe the same physics and apply exactly the same wave functions, the ill-conditioned character influences the coupling conditions and thus the solution.

When comparing the efficiency of the hybrid methodologies to standard FE implementations, it is clear that a nice gain is obtained, revealing the potential of the proposed approach.

6 Conclusion

This paper gives an overview of modelling theories and numerical prediction techniques to describe the steady-state dynamic behaviour of poroelastic materials. Poroelastic materials can be described using two homogenised phases on a macroscopic level: the solid phase and the fluid phase.

A first class of theories describes the propagation of sound in those materials using the Helmholtz equation, by using a complex and frequency dependent density and a complex bulk modulus. There are a number of approximations available in literature to calculate these equivalent properties. Simple empirical relations, such as the laws of Delany and Bazley and Miki are detailed. If it is assumed that the solid frame is rigid and consequently motionless and the pores have simple geometries, analytical expressions for the equivalent density and bulk modulus can be derived. It is shown that the equivalent density accounts for viscous losses, whereas the equivalent bulk modulus takes into account thermal losses. When the pore geometry is more complex, analytical expressions cannot be retrieved. In that case, mostly semi-phenomenological models are used. These models apply a relaxation function to take into account the transition from microscale Stokes flow at very low frequencies to inviscid flow as high frequency asymptote. The concept of tortuosity, and viscous characteristic length is introduced. In a similar fashion, a relaxation function is defined to account for the transition from isothermal behaviour as low frequency limit to adiabatic behaviour as high frequency limit using the thermal characteristic length. This model, which is further used in this review paper, is often referred to as the Johnson-Champoux-Allard model. More complex models also exist, but are not commonly applied, due to the higher number of material parameters to be identified. Beside rigid frame equivalent fluid models, also limp models can be applied. In this case the stiffness of the frame can be neglected and again the propagation of sound through the material can be described using a Helmholtz equation. Also double porosity materials, consisting of two networks of pores at a different scale, can be modelled in a one-wave formalism.

When taking into account the elasticity of the frame, the Biot theory is applied. The poroelastic medium is described using a macroscopic description of two homogenised phases: the elastic solid phase and the fluid phase. Both phases mutually interact and the Johnson-Champoux-Allard model is used to account for viscous and thermal losses. The theory by Biot predicts the presence of three propagating waves in a poroelastic material: two compressional waves and one shear wave.

Different numerical prediction techniques are being applied to predict the steady-state response of poroelastic materials in a vibro-acoustic setting. In the lower

frequency range, the Finite Element Method is most commonly applied. It divides the problem domain into a large number of small elements in which the dynamic variables are approximated using simple polynomial functions. A number of formulations are discussed in this paper, which use different primary variables. For higher frequencies the method loses its attractiveness since the number of elements should be increased to be able to accurately capture the dynamics of the three wave types. Reduction schemes to overcome the large computation costs of finite element models are also discussed. Straightforward modal reduction techniques are, however, not applicable due to the complex and frequency dependent material properties.

At higher frequencies, the Transfer Matrix Method is widely used to predict the transmission loss of multilayer structures consisting of an arbitrary lay-up of acoustic, poroelastic and elastic layers. This method assumes layers of an infinite extent and uses a plane wave description for the wave propagation through a layer. Transfer matrices, interface and termination conditions are combined in a global transfer matrix which can be used to relate dynamic quantities on both sides of the multilayer. The ease of use and the method's low computational requirements are its distinct advantages. It is often used to predict trends and works well for locally reacting materials. However at lower frequencies, or when the effect of boundary conditions is important, it is often not sufficiently accurate. Extenstions to the method to partially overcome these restrictions are reviewed.

Recently, Trefftz methods are being applied to predict the behaviour of poroelastic materials as governed by the Biot equations. Trefftz methods are deterministic methods which increase the achievable frequency range of element based prediction techniques by embedding *a priori* known information of the physics of the problem into the numerical model. This review paper discusses one of those promising methods, the Wave Based Method, in detail. The Wave Based Method partitions the problem domain into convex subdomains. Within each subdomain the dynamic field variables are approximated using a weighted sum of wave functions which exactly fulfill the dynamic equations. In the case of the Biot equations, the three wave types are explicitly accounted for. The dynamic field do not comply with the imposed boundary and interface conditions. These errors are minimised using a weighted residual approach, resulting in a system of matrices which may be solved for the unknown wave function contribution factors. The resulting matrices are small, and the convergence of the method is high. Advantages and drawbacks of the method are discussed. So far the method has been applied for two-dimensional and axisymmetric poroelastic problems. A number of validation cases are included in the paper. It can also be used in a hybrid scheme with the Finite Element Method to effectively model acoustic cavities with trim components. The Wave Based Method is used to efficiently model the acoustic domain, whereas the Finite Element Method can be used to model the trim layers in great detail. The $(\mathbf{u^s}, \mathbf{u^f})$-formulation and the $(\mathbf{u^s}, p^f)$-formulation have been used; the latter has shown to be the most efficient and more stable in combination with the acoustic Wave Based Method.

Acknowledgements The Research Fund KU Leuven is gratefully acknowledged for the support of the postdoctoral research of Elke Deckers and the institute for Promotion of Innovation by Science and Technology Flanders (Belgium) (IWT-Vlaanderen) is gratefully acknowledged for the support of the doctoral research of Stijn Jonckheere. Furthermore, the IWT Flanders within the ASTRA project, the Fund for Scientific Research - Flanders (F.W.O.), and the Research Fund KU Leuven are also gratefully acknowledged for their support. The EC within the FP7 eLiQuiD Marie Curie European Industry Doctorate (GA 316422) is also gratefully acknowledged for its support.

A Material properties

This appendix collects the material data used in the examples in this paper. Table 5 shows the air properties used.

Table 5 Material properties of air.

Air properties	
Thermal conductivity	$k_c = 2.57 \cdot 10^{-2}$W(mK)
Specific heat	$c_p = 1.005 \cdot 10^3$J/(kgK)
Gas constant	R^{gas}=286.7m^2/(s^{2}K)
Temperature	T=293.15K
Ratio of specific heats	γ=1.4
Fluid kinematic viscosity	ν_f=15.11$\cdot 10^{-6}$m^2/s
Fluid density	ρ_0=1.205kg/m^3

Table 6 summarises the data of the poroelastic materials used in this review paper. The material properties of melamine have been experimentally determined by the department of physics of KU Leuven, as described in [173]. In the calculations, the average values of the material properties have been used. The polyurethane material properties are taken from [60]. An arbitrary loss factor η_l has been added, as the augmented Hooke's law has not been applied. The carpet material properties are taken from [63]. The fireflex material data are taken from [167]. It is a poluyrethane foam, which is fabricated by Recticel, Belgium.

Table 6 Material properties of the poroelastic media used in this review paper.

Melamine [173]	
Young's modulus	$E = (260 \pm 13 + j(30 \pm 3))$kPa
Shear modulus	$N = (95 \pm 9 + j(6 \pm 0.5))\, kPa$
Bulk density	$\rho_1 = (9.4 \pm 1) kg/m^3$
Porosity	$h \geq 0.95$
Viscous characteristic length	$\Lambda = (166 \pm 17) \cdot 10^{-6}$m
Thermal characteristic length	$\Lambda' = (249 \pm 25) \cdot 10^{-6}$m
Static flow resistivity	$\sigma = (9500 \pm 600) kg/(m^3 \mathrm{s})$
Tortuosity	$\alpha_\infty = 1.01 \pm 0.11$
Polyurethane foam material [60]	
Young's modulus	$E_s = 70 \cdot 10^3 Pa$
Loss factor	$\eta_l = 0.265$
Poisson ratio	$\nu = 0.39$
Bulk density	$\rho_1 = 22.1 kg/m^3$
Porosity	$h = 0.98$
Viscous characteristic length	$\Lambda = 1.1 \cdot 10^{-4} m$
Thermal characteristic length	$\Lambda' = 7.42 \cdot 10^{-4} m$
Static flow resistivity	$\sigma = 3.75 \cdot 10^3 kg/(m^3 s)$
Tortuosity	$\alpha_\infty = 1.17$
Carpet material [63]	
Young's modulus	$E_s = 20 \cdot 10^3 Pa$
Loss factor	$\eta_l = 0.5$
Poisson ratio	$\nu = 0$
Bulk density	$\rho_1 = 60 kg/m^3$
Porosity	$h = 0.99$
Viscous characteristic length	$\Lambda = 1.5 \cdot 10^{-4} m$
Thermal characteristic length	$\Lambda' = 2.2 \cdot 10^{-4} m$
Static flow resistivity	$\sigma = 20 \cdot 10^3 kg/(m^3 s)$
Tortuosity	$\alpha_\infty = 1$
Fireflex [167]	
Young's modulus	$E = 4.3 \cdot 10^5 + j \cdot 1 \cdot 10^5$Pa
Shear modulus	$N = 1.6 \cdot 10^5 + j \cdot 3 \cdot 10^4$Pa
Bulk density	$\rho_1 = 30$kg/m^3
Porosity	$h = 0.93$
Viscous characteristic length	$\Lambda = 10 \cdot 10^{-6}$m
Thermal characteristic length	$\Lambda' = 100 \cdot 10^{-6}$m
Static flow resistivity	$\sigma = 80 \cdot 10^3$kg/(m^{3}s)
Tortuosity	$\alpha_\infty = 2.5$

References

1. W. Passchier-Vermeer and W.F. Passchier. Noise exposure and public health. *Environmental Health Perspectives*, 108(1):123–131, 2000.
2. Bathe K.J. *Finite Element Procedures*. Prentice Hall, New Jersey, 1996.
3. O. C. Zienkiewicz, R.L. Taylor, J.Z. Zhu, and P. Nithiarasu. *The Finite Element Method - The three volume set*. Butterworth-Heinemann, 6th edition, 2005.
4. Banerjee P.K. and Butterfield R. *Boundary element methods in engineering science*. McGraw-Hill Book Co. (UK), 1981.
5. O. Von Estorff. *Boundary Elements in Acoustics: Advances and Applications*. WITpress, 2000.
6. P. Bouillard and R. Ihlenburg. Error estimation and adaptivity for the finite element method in acoustics: 2D and 3D applications. *Computer Methods in Applied Mechanics and Engineering*, 176:147–163, 1999.
7. R. Freymann. *Advanced numerical and experimental methods in the field of vehicle structural-acoustics*. Hieronymus Buchreproduktions GmbH, 2000.
8. S. Marburg. Six boundary elements per wavelength: is that enough? *Journal of Computational Acoustics*, 10: 25–51, 2002.
9. R.H. Lyon and R.G. De Jong. *Theory and application of statistical energy analysis*. Butterworth-Heinemann, 2nd edition, 1995.
10. Y.A. Erlangga. Advances in iterative methods and preconditioners for the Helmholtz equation. *Archives of Computational Methods in Engineering*, 15:37–66, 2008.
11. R.R. Craig Jr. and A.J. Kurdila. *Fundamentals of Structural Dynamics*. John Wiley & Sons, New York Chichester Brisbane Toronto Singapore, 2nd edition, 2005.
12. C. Farhat, I. Harari, and L.P. Franca. The discontinuous enrichment method. *Computer Methods in Applied Mechanics and Engineering*, 190:6455–6479, 2001.
13. J. Melenk and I. Babuška. The partition of unity finite element method: Basic theory and applications. *Computer Methods in Applied Mechanics and Engineering*, 139:289–314, 1996.
14. E. Trefftz. Ein Gegenstück zum Ritzschen Verfahren. In *Proceedings of the 2^{nd} International Congress on Applied Mechanics, Zurich, Switzerland*, pages 131–137, 1926.
15. B. Mace and P. Shorter. Energy flow models from finite element analysis. *Journal of Sound and Vibration*, 233: 369–389, 2000.
16. L. Maxit and J.-L. Guyader. Estimation of SEA coupling loss factors using a dual formulation and FEM modal information, part I: Theory. *Journal of Sound and Vibration*, 239:907–930, 2001.
17. R.S. Langley and J.A. Cordioli. Hybrid deterministic-statistical analysis of vibro-acoustic systems with domain couplings on statistical components. *Journal of Sound and Vibration*, 321:893–912, 2009.
18. P. Shorter and R. Langley. On the reciprocity relationship between direct field radiation and diffuse reverberant loading. *Journal of the Acoustical Society of America*, 117:85–95, 2005.
19. O. Coussy. *Poromechanics*. John Wiley & Sons, Ltd., 2004.
20. H.F. Wang. *Theory of Linear Poroelasticity, with Applications to Geomechanics and Hydrogeology*. Princeton University Press, 2000.
21. F.B. Jensen, W.A. Kuperman, M.B. Porter, and H. Schmidt. *Computational ocean acoustics*. Springer, 2nd edition, 2011.
22. T.H. Smit, J.M. Hyghe, and S.C. Cowin. Estimation of the poroelastic parameters of cortical bone. *Journal of Biomechanics*, 35:829–835, 2002.
23. J.F. Allard and N. Atalla. *Propagation of Sound in Porous Media: Modeling Sound Absorbing Materials*. John Wiley & Sons, West Sussex, United Kingdom, 2nd edition, 2009.
24. C. Zwikker and C.W. Kosten. *Sound absorbing materials*. Elsevier, New York, 1949.
25. M.A. Biot. The theory of propagation of elastic waves in a fluid-saturated porous solid. I. Low frequency range. *Journal of the Acoustical Society of America*, 28:168–178, 1956.
26. M.-E. Delany and E.N. Bazley. Acoustical properties of fibrous materials. *Applied Acoustics*, 3:105–116, 1970.
27. Y. Miki. Acoustical properties of porous materials - Modifications of Delany-Bazley models. *Journal of the Acoustical Society of Japan*, 11:19–24, 1990.
28. F.P. Mechel. Ausweitung der Absorberformel von Delany und Bazley zu tiefen Frequenzen. *Acustica*, 35: 210–213, 1976.
29. T. Komatsu. Improvement of the Delany-Bazley and Miki models for fibrous sound-absorbing materials. *Acoustical Science and Technology*, 29:121–129, 2008.
30. G. Kirchhoff. Über der Einfluss der Wärmeleitung in einem Gase auf die Schallbewegung. *Annalen der Physik and Chemie*, 134:177–193, 1868.

31. M.R. Stinson. The propagation of plane sound waves in narrow and wide circular tubes, and generalization to uniform tubes of arbitrary cross-sectional shape. *Journal of the Acoustical Society of America*, 89:550–558, 1991.
32. M.A. Biot. The theory of propagation of elastic waves in a fluid-saturated porous solid. II. Higher frequency range. *Journal of the Acoustical Society of America*, 28:179–191, 1956.
33. A. Craggs and J.G. Hildebrandt. The normal incidence absorption coefficient of a matrix of narrow tubes with constant cross-section. *Journal of Sound and Vibration*, 105:101–107, 1986.
34. K. Attenborough. Acoustical characteristics of rigid fibrous absorbents and granular media. *Journal of the Acoustical Society of America*, 73:785–799, 1983.
35. D.L. Johnson, J. Koplik, and R. Dashen. Theory of dynamic permeability and tortuosity in fluid-saturated porous media. *Journal of Fluid Mechanics*, 176:379–402, 1987.
36. Y. Champoux and J.F. Allard. Dynamic tortuosity and bulk modulus in air-saturated porous media. *Journal of Applied Physics*, 70:1975–1979, 1991.
37. C. Perrot, F. Chevilotte, M.T. Hoang, G. Bonnet, F.-X. Bécot, L. Gautron, and A. Duval. Microstructures, transport, and acoustic properties of open-cell foam samples: Experiments and three-dimensional numerical simulations. *Journal of Applied Physics*, 111:014911, 2012.
38. M.T. Hoang and C. Perrot. Identifying local characteristic lenghts governing sound wave properties in solid foams. *Journal of Applied Physics*, 113:084905, 2013.
39. W. Lauriks and P. Leclaire. *Chapter 61: Materials Testing, In Handbook of Signal Processing in Acoustics*. Springer, New York, 2008.
40. D. Lafarge, P. Lemarinier, J.F. Allard, and V. Tarnow. Dynamic compressibility of air in porous structures at audible frequencies. *Journal of the Acoustical Society of America*, 102:1995–2006, 1997.
41. C. Perrot, R. Panneton, and X. Olny. Periodic unit cell reconstruction of porous media: Application to open-cell aluminum foams. *Journal of Applied Physics*, 101: 113538, 2007.
42. J.L. Auriault. Heterogeneous medium. Is an equivalent macroscopic description possible? *International Journal of Engineering Science*, 29:785–795, 1991.
43. D.K. Wilson. Relaxation-matched modeling of propagation through porous media, including fractal pore structure. *Journal of the Acoustical Society of America*, 94: 1136–1145, 1993.
44. S.R. Pride, F.D. Morgan, and F.A. Gangi. Drag forces of porous media acoustics. *Physical review B*, 47:4964–4975, 1993.
45. D. Lafarge. *Propagation du son dans les matériaux poreux à structure rigide saturés par un fluide viscothermique: Définition de paramètres géométrique, analogie electromagnétique, temps de relaxation*. PhD. thesis, Université du Maine (France), 1993.
46. R. Panneton and X. Olny. Acoustical determination of the parameters governing viscous dissipation in porous media. *Journal of the Acoustical Society of America*, 119:2027–2040, 2006.
47. X. Olny and R. Panneton. Acoustical determination of the parameters governing thermal dissipation in porous media. *Journal of the Acoustical Society of America*, 123:814–824, 2008.
48. R. Panneton. Comments on the limp frame equivalent fluid model for porous media. *Journal of the Acoustical Society of America*, 122:217–222, 2007.
49. O. Doutres, N. Dauchez, J.-M. Génevaux, and O. Dazel. Validity of the limp model for porous materials: A criterion based on the Biot theory. *Journal of the Acoustical Society of America*, 122:2038–2048, 2007.
50. C. Boutin, P. Royer, and J.L. Auriault. Acoustic absorption of porous surfacing with dual porosity. *International Journal of Solids and Structures*, 35:4709–4737, 1998.
51. X. Olny and C. Boutin. Acoustic wave propagation in double porosity media. *Journal of the Acoustical Society of America*, 114:73–89, 2003.
52. N. Atalla, F. Sgard, X. Olny, and R. Panneton. Acoustic absorption of macro-perforated porous materials. *Journal of Sound and Vibration*, 243:659–678, 2001.
53. F.C. Sgard, X. Olny, N. Atalla, and F. Castel. On the use of perforations to improve the sound absorption of porous materials. *Applied Acoustics*, 66:625–651, 2005.
54. R. Lanoye. *Assessment of the absorption performance of sound absorbing materilas. Use of the Trefftz's method and of a new dual particle velocity-pressure sensor*. KULeuven, Department of Civil Engineering and Department of Acoustics and Thermal Physics, PhD. thesis, 2007.
55. M.A. Biot. Mechanics of Deformation and Acoustic Propagation in Porous Media. *Journal of Applied Physics*, 33:1482–1498, 1962.
56. R. Burridge and J.B. Keller. Poroelasticity equations derived from microstructure. *Journal of the Acoustical Society of America*, 70:1140–1146, 1981.
57. S.R. Pride, A.F. Gangi, and F.D. Morgan. Deriving the equations of motion for porous isotropic media. *Journal of the Acoustical Society of America*, 92:3278–3290, 1992.
58. M.A. Biot and D.G. Willis. The elastic coefficients of consolidation. *Journal of Applied Mechanics*, 34:594–601, 1957.
59. K. Dovstam. Augmented Hooke's law in frequency domain. *International Journal of Solids and Structures*, 32:2835–2852, 1995.
60. N.-E. Hörlin, M. Nordström, and P. Göransson. A 3-D hierarchical FE formulation of Biot's equations for elasto-acoustic modelling of porous media. *Journal of Sound and Vibration*, 245:633–652, 2001.
61. P. Göransson. Acoustic and vibrational damping in porous solids. *Philosophical Transactions of the Royal Society A*, 364:89–108, 2006.
62. P.S. Kurzeja and H. Steeb. About the transition frequency in Biot's theory. *JASA Express Letters*, 131: 454–460, 2012.
63. P. Debergue, R. Panneton, and N. Atalla. Boundary conditions for the weak formulation of the mixed (u,p) poroelasticity problem. *Journal of the Acoustical Society of America*, 106:2383–2390, 1999.
64. N.-E. Hörlin. *Hierarchical finite element modelling of Biot's equations for vibro-acoustic modelling of layered poroelastic media*. Doctoral thesis, KTH Aeronautical and Vehicle Engineering, Stockholm, Sweden, 2004.
65. S. Rigobert, N. Atalla, and F.C. Sgard. Investigation of the convergence of the mixed displacement-pressure poroelastic materials using hierarchical elements. *Journal of the Acoustical Society of America*, 114:2607–2617, 2003.
66. X. Sagartzazu, L. Hervella-Nieto, and J.M. Pagalday. Review in Sound Absorbing Materials. *Archives of*

Computational Methods in Engineering, 15:311–342, 2008.
67. L. Jaouen, A. Renault, and M. Deverge. Elastic and damping characterizations of acoustical porous materials: Available experimental methods and applications to a melamine foam. *Applied Acoustics*, 69:1129–1140, 2008.
68. J. Pan and P. Jackson. Review of Test Methods for Materials Properties of Elastic Porous Materials. In *SAE International*, pages 2009–01–2135, 2009.
69. L. Jaouen. Characterization of acoustic and elastic parameters of porous media. In *Proceedings of the Symposium on the Acoustics of Poro-Elastic Materials, SAPEM2011, Ferrara (Italy)*, 2011.
70. A. Vashishth and P. Khurana. Waves in stratified anisotropic poroelastic media: a transfer matrix approach. *Journal of Sound and Vibration*, 277:239–275, 2004.
71. P. Khuruna, L. Boeckx, W. Lauriks, P. Leclaire, O. Dazel, and J.F. Allard. A description of transversely isotropic sound absorbing porous materials by transfer matrices. *Journal of the Acoustical Society of America*, 125:915–921, 2009.
72. J.M. Carcione. *Wave Fields in Real Media: Wave Propagation in Anisotropic, Anelastic, Porous and Electromagnetic Media*. Elsevier Amsterdam, 2nd edition, 2007.
73. N.-E. Hörlin and P. Göransson. Weak, anisotropic symmetric formulations of Biot's equations for vibro-acoustic modelling of porous elastic materials. *International Journal for Numerical Methods in Engineering*, 84:1519–1540, 2010.
74. P. Göransson and N.-E. Hörlin. Vibro-Acoustic Modelling of Anisotropic Porous Elastic Materials: A Preliminary Study of the Influence of Anisotropy on the Predicted Performance in a Multi-Layer Arrangement. *Acta Acustia United with Acustica*, 96:258–265, 2010.
75. E. Lind Nordgren, P. Göransson, J.-F. Deü, and O. Dazel. Vibroacoustic response sensitivity due to relative alignment of two anisotropic poro-elastic layers. *JASA Express Letters*, 133:426–430, 2013.
76. F.-X. Bécot, O. Dazel, and L. Jaouen. Structural effects in double porosity materials: analytical modeling and numerical validation. In *Proceedings of the Conference on Noise and Vibration Engineering 2010, ISMA2010, Leuven, (Belgium)*, 2010.
77. O. Dazel, F.-X. Bécot, and L. Jaouen. Biot Effects for Sound Absorbing Double Porosity Materials. *Acta Acustica United with Acustica*, 98:567–576, 2012.
78. N. Dauchez, S. Sahraoui, and N. Atalla. Convergence of poroelastic finite elements based on Biot displacement formulation. *Journal of the Acoustical Society of America*, 109:33–40, 2001.
79. N. Dauchez, S. Sahraoui, and N. Atalla. Investigation and modelling of damping in a plate with a bonded porous layer. *Journal of Sound and Vibration*, 265:437–449, 2002.
80. O. Tanneau, P. Lamary, and Y. Chevalier. A boundary element method for porous media. *Journal of the Acoustical Society of America*, 120:1239–1251, 2006.
81. A. Craggs. A finite element model for rigid porous absorbing materials. *Journal of Sound and Vibration*, 61: 101–111, 1978.
82. P. Göransson. Acoustic finite element formulation of a flexible porous material - a correction for inertial effects. *Journal of Sound and Vibration*, 185:559–580, 1995.
83. Y.J. Kang and J.S. Bolton. Finite element modeling of isotropic elastic porous materials coupled with acoustical finite elements. *Journal of the Acoustical Society of America*, 98:635–643, 1995.
84. R. Panneton and N. Atalla. An efficient finite element scheme for solving the three dimensional poro-elasticity problems in acoustics. *Journal of the Acoustical Society of America*, 101:3287–3297, 1997.
85. J.P. Coyette. The use of finite-element and boundary-element models for predicting the vibro-acoustic behaviour of layered structures. *Advances in Engineering Software*, 30:133–139, 1999.
86. V. Easwaran, W. Lauriks, and J.P. Coyette. Displacement-based finite element method for guided wave propagation problems: Application to poroelastic media. *Journal of the Acoustical Society of America*, 100:2989–3002, 1996.
87. P. Göransson. A 3-D symmetric finite element formulation of the Biot equations with application to acoustic wave propagation through an elastic porous medium. *International Journal of Numerical Methods in Engineering*, 41:167–192, 1998.
88. N. Atalla, M.A. Hamdi, and R. Panneton. Enhanced weak integral formulation for the mixed ($\underline{u}$,$\underline{p}$) poroelastic equations. *Journal of the Acoustical Society of America*, 109:3065–3068, 2001.
89. N. Atalla, R. Panneton, and P. Debergue. A mixed displacement-pressure formulation for poroelastic materials. *Journal of the Acoustical Society of America*, 104:1444–1452, 1998.
90. O. Dazel, B. Brouard, C. Depollier, and S. Griffiths. An alternative Biot's displacement formulation for porous materials. *Journal of the Acoustical Society of America*, 121:3509–3516, 2007.
91. N.-E. Hörlin. A symmetric weak form of Biot's equations based on redundant variables representing the fluid, using a Helmholtz decomposition of the fluid displacement vector field. *International Journal for Numerical Methods in Engineering*, 84:1613–1637, 2010.
92. Y.J. Kang, B.C. Gardner, and J.S. Bolton. An axisymmetric poroelastic finite element formulation. *Journal of the Acoustical Society of America*, 106:565–574, 1999.
93. M. Östberg, N.E. Hörlin, and P. Göransson. Weak formulation of Biot's equations in cylindrical coordinates with harmonic expansions in the circumferential direction. *International Journal for Numerical Methods in Engineering*, 81:1439–1454, 2010.
94. S. Rigobert, F.C. Sgard, and N. Atalla. A two-field hybrid formulation for multilayers involving poroelastic, acoustic, and elastic materials. *Journal of the Acoustical Society of America*, 115:2786–2797, 2004.
95. O. Dazel, F. Sgard, C.H. Lamarque, and N. Atalla. An extension of complex modes for the resolution of finite-element poroelastic problems. *Journal of Sound and Vibration*, 253:421–445, 2002.
96. O. Dazel, F. Sgard, and C.H. Lamarque. Application of generalized complex modes to the calculation of the forced response of three-dimensional poroelastic materials. *Journal of Sound and Vibration*, 268:555–580, 2003.
97. F. Sgard, N. Atalla, and R. Panneton. A modal reduction technique for the finite element formulation of Biot's poroelasticity equations in acoustics. In *134^{th} ASA Meeting, San Diego, United States*, 1997.
98. P. Davidsson and G. Sandberg. A reduction method for structure-acoustic and poroelastic-acoustic problems using interface-dependent Lanczos vectors. *Computer*

Methods in Applied Mechanics and Engineering, 195: 1933–1945, 2006.
99. O. Dazel, B. Brouard, N. Dauchez, and A. Geslain. Enhanced Biot's Finite Element Displacement Formulation for Porous Materials and Original Resolution Methods Based on Normal Modes. *Acta Acustica United with Acustica*, 95:527–538, 2009.
100. O. Dazel, B. Brouard, N. Dauchez, A. Geslain, and C.H. Lamarque. A Free Interface CMS Technique to the Resolution of Coupled Problem Involving Porous Materials, Application to a Monodimensional Problem. *Acta Acustica United with Acustica*, 96:247–257, 2010.
101. R. Rumpler, J.-F. Deü, and P. Göransson. A modal-based reduction method for sound absorbing porous materials in poro-acoustic finite element models. *Journal of the Acoustical Society of America*, 132:3162–3179, 2012.
102. R. Rumpler, P. Göransson, and J.-F. Deü. A residue-based mode selection and sorting procedure for efficient poroelastic modeling in acoustic finite element applications. *Journal of the Acoustical Society of America, Accepted for publication*, 2013.
103. R. Rumpler. *Efficient Finite Element Approach for Structural-Acoustic Applications including 3D Modelling of Sound Absorbing Porous Materials*. Doctoral Thesis in Technical Acoustics, Stockholm, Sweden, 2012.
104. O. Dazel, B. Brouard, J.-P. Groby, and P. Göransson. A normal modes technique to reduce the order of poroelastic models: application to 2D and coupled 3D models. *International Journal for Numerical Methods in Engineering*, 2013.
105. J.F. Allard, Y. Champoux, and C. Depollier. Modelization of layered sound absorbing materials with transfer matrices. *Journal of the Acoustical Society of America*, 82:1792–1796, 1987.
106. J.F. Allard, C. Depollier, P. Rebillard, W. Lauriks, and A. Cops. Inhomogeneous Biot waves in layered media. *Journal of Applied Physics*, 66:2278–2284, 1989.
107. M. Villot, C. Guigou, and L. Gagliardini. Predicting the acoustical radiation of finite size multi-layered structures by applying spatial windowing on infinite structures. *Journal of Sound and Vibration*, 245:433–455, 2001.
108. S. Ghinet and N. Atalla. Vibro-acoustic behaviour of multi-layer orthotropic panels. *Canadian Acoustics*, 30: 72–73, 2002.
109. N. Atalla, F. Sgard, and C.K. Amedin. On the modeling of sound radiation from poroelastic materials. *Journal of the Acoustical Society of America*, 120:1990–1995, 2006.
110. D. Rhazi and N. Atalla. Transfer matrix modeling of the vibroacoustic response of multi-materials structures under mechanical excitation. *Journal of Sound and Vibration*, 329:2532–2546, 2010.
111. T.E. Vigran. Sound transmission in multilayered structures - Introducing finite structural connections in the transfer matrix method. *Applied Acoustics*, 71:39–44, 2010.
112. J. Legault and N. Atalla. Numerical and experimental investigation of the effect of structural links on the sound transmission of a lightweight double panel structure. *Journal of Sound and Vibration*, 324:712–732, 2009.
113. J. Legault and N. Atalla. Sound transmission through a double panel structure periodically coupled with vibration insulators. *Journal of Sound and Vibration*, 329: 3082–3100, 2010.
114. K. Verdière, R. Panneton, S. Elkoun, T. Dupont, and P. Leclaire. Prediction of acoustic properties of parallel assemblies by means of transfer matrix method. In *Proceedings of Meetings on Acoustics*, volume 19, 2013.
115. L. Alimonti, N. Atalla, A. Berry, and F. Sgard. A hybrid modelling approach for vibroacoustic systems with attached sound packages. In *Proceedings of Meetings on Acoustics*, volume 19, 2013.
116. M. Tournour, M. Kosaka, and H. Shiozaki. Fast Acoustic Trim Modeling using Transfer Matrix Admittance and Finite Element Method. In *SAE 2007 Noise and Vibration Conference and Exhibition, St. Charles, IL, USA*, 2007.
117. L.D. Pope, E.G. Wilby, C.M. Willis, and W.H. Mayes. Aircraft Interior Noise Models: Sidewall trim, stiffened structures and cabin acoustics with floor partition. *Journal of Sound and Vibration*, 89:371–417, 1983.
118. A. Duval, L. Dejaeger, L. Bischoff, and C. Morgenstern. Trim FEM Simulation of a Headliner Cut Out Module with Structureborne and Airborne Excitations. In *Proceedings of the 7th International Styrian Noise, Vibration & Harshness Congress: The European Automotive Noise Conference, ISNVH2012, Graz, (Austria)*, 2012.
119. A. Duval, L. Dejaeger, L. Bischoff, F. Lhuillier, and J. Monet-Descombey. Generalized Light-Weight Concepts: A New Insulator 3D Optimization Procedure. In *Proceedings of the SAE 2013 Noise and Vibration Conference and Exhibition, Gran Rapids, (United States)*, 2013.
120. B. Pluymers, B. Van Hal, D. Vandepitte, and W. Desmet. Trefftz-based methods for time-harmonic acoustics. *Archives of Computational Methods in Engineering*, 14:343–381, 2007.
121. J.D. Chazot, B. Nennig, and E. Perrey-Debain. Performances of the Partition of Unity Finite Element Method for the analysis of two-dimensional interior sound field with absorbing materials. *Journal of Sound and Vibration*, 332:1918–1929, 2013.
122. R. Lanoye, G. Vermeir, W. Lauriks, F. Sgard, and W. Desmet. Prediction of the sound field above a patchwork of absorbing materials. *Journal of the Acoustical Society of America*, 123:793–802, 2008.
123. J.A. Teixeira de Freitas and M. Toma. Hybrid-Trefftz stress elements for incompressible biphasic media. *International Journal for Numerical Methods in Engineering*, 79:205–238, 2009.
124. I.D. Moldovan. *Hybrid-Trefftz finite elements for elastodynamic analysis of saturated porous media*. PhD thesis, Universidade Técnica de Lisboa, 2008.
125. J.A. Teixeira de Freitas and I.D. Moldovan. Hybrid-Trefftz stress elements for bounded and unbounded poroelastic media. *International Journal for Numerical Methods in Engineering*, 85:1280–1305, 2011.
126. J.A. Teixeira de Freitas, I.D. Moldovan, and C. Cismaşiu. Hybrid-Trefftz displacements elements for poroelastic media. *Computational Mechanics*, 48: 659–673, 2011.
127. B. Nennig, E. Perry-Debain, and J.D. Chazot. The method of fundamental solutions for acoustic wave scattering by a single and a periodic array of poroelastic scatterers. *Engineering Analysis with Boundary Elements*, 35:1019–1028, 2011.
128. G. Gabard. Discontinuous Galerkin methods with plane waves for time-harmonic problems. *Journal of Computational Physics*, 225:1961–1984, 2007.
129. O. Dazel and G. Gabard. Discontinuous Galerkin Methods for poroelastic materials. In *Proceedings of Meeting on Acoustics, ICA 2013 Montreal (Canada)*, 2013.

130. W. Desmet. *A wave based prediction technique for coupled vibro-acoustic analysis*. KULeuven, division PMA, PhD. thesis 98D12, 1998.
131. W. Desmet, B. Pluymers, O. Atak, B. Bergen, R. D'Amico, E. Deckers, S. Jonckheere, K. Koo, J.S. Lee, A. Maressa, N. Navarrete, B. Van Genechten, D. Vandepitte, and K. Vergote. *Chapter 1: "The Wave Based Method", in "Mid-Frequency CAE Methodologies for Mid-Frequency Analysis in Vibration and Acoustics"*. KULeuven, 2012.
132. E. Deckers, O. Atak, L. Coox, R. D'Amico, H. Devriendt, S. Jonckheere, K. Koo, B. Pluymers, D. Vandepitte, and W. Desmet. The Wave Based Method: an overview of 15 years of research. *submitted for publication in Wave Motion*, 2013.
133. H.L.F. Helmholtz. Über Integrale der hydrodynamischen Gleichungen, welch den Wirbelbewegungen entsprechen. *Crelles Journal*, 55:25–55, 1958.
134. O. Cessenat and B. Deprès. Using plane waves as base functions for solving time harmonic equations with the ultra weak variational formulation. *Journal of Computational Acoustics*, 11:227–238, 2003.
135. I. Herrera. *Boundary Methods: an Algebraic Theory*. Applicable mathematic series. Pitman Advanced Publishing Programm, 1984.
136. B. Van Hal. *Automation and performance optimization of the wave based method for interior structural-acoustic problems*. PhD Thesis, Faculty of Engineering, Katholieke Universiteit Leuven, 2004.
137. B. Van Genechten, B. Bergen, D. Vandepitte, and W. Desmet. A Trefftz-based numerical modelling framework for Helmholtz problems with complex multiple scatterer configurations. *Journal of Computational Physics*, 229(18):6623–6643, 2010.
138. B. Van Genechten, K. Vergote, D. Vandepitte, and W. Desmet. A multi-level wave based numerical modelling framework for the steady-state dynamic analysis of bounded Helmholtz problems with multiple inclusions. *Computer Methods in Applied Mechanics and Engineering*, 199:1881–1905, 2010.
139. B. Van Genechten, D. Vandepitte, and W. Desmet. A direct hybrid finite element - Wave based modelling technique for efficient coupled vibro-acoustic analysis. *Computer Methods in Applied Mechanics and Engineering*, 200:742–764, 2011.
140. T. Huttunen, P. Gamallo, and R.J. Astley. Comparison of two wave element methods for the Helmholtz problem. *Communications in Numerical Methods in Engineering*, 25:35–52, 2009.
141. A. P. Zieliński and I. Herrera. Trefftz method: fitting boundary conditions. *International Journal on Numerical Methods in Engineering*, 24:871–891, 1987.
142. J.M. Varah. A practical examination of some numerical methods for linear discrete ill-posed problems. *SIAM Review*, 21:100–111, 1979.
143. J.M. Varah. Pitfalls in the numerical solution of linear ill-posed problems. *SIAM Journal on Scientific and Statistical Computing*, 4:164–176, 1983.
144. B. Pluymers. *Wave based modelling methods for steady-state vibro-acoustics*. KU Leuven, division PMA, PhD. thesis 2006D04, Leuven, 2006.
145. E. Deckers, B. Bergen, B. Van Genechten, D. Vandepitte, and W. Desmet. An efficient Wave Based Method for 2D acoustic problems containing corner singularities. *Computer Methods in Applied Mechanics and Engineering*, 241-244:286–301, 2012.
146. B. Van Genechten, O. Atak, B. Bergen, E. Deckers, S. Jonckheere, J.S. Lee, A. Maressa, K. Vergote, B. Pluymers, D. Vandepitte, and W. Desmet. An efficient Wave Based Method for solving Helmholtz problems in three-dimensional bounded domains. *Engineering Analysis with Boundary Elements*, 36:63–75, 2012.
147. B. Pluymers, W. Desmet, D. Vandepitte, and P. Sas. On the use of a wave based prediction technique for steady-state structural-acoustic radiation analysis. *Computer Modeling in Engineering & Sciences*, 7(2): 173–184, 2005.
148. D. Colton and R. Kress. *Inverse acoustic and electromagnetic scattering theory*. Springer-Verlag, Berlin, Heidelbert, New York, 2nd edition, 1998.
149. B. Bergen, B. Van Genechten, D. Vandepitte, and W. Desmet. An efficient Trefftz-based method for three-dimensional Helmholtz problems in unbounded domains. *Computer Modeling in Engineering & Sciences*, 61(2):155–175, 2010.
150. B. Bergen, B. Pluymers, B. Van Genechten, D. Vandepitte, and W. Desmet. A Trefftz based method for solving Helmholtz problems in semi-infinite domains. *Engineering Analysis with Boundary Elements*, 36:30–38, 2012.
151. B. Bergen. *Wave based modelling techniques for unbounded acoustic problems*. KULeuven, division PMA, PhD. thesis 2011D07, 2011.
152. C. Vanmaele, D. Vandepitte, and W. Desmet. An efficient wave based prediction technique for plate bending vibrations. *Computer Methods in Applied Mechanics and Engineering*, 196:3178–3189, 2007.
153. C. Vanmaele, D. Vandepitte, and W. Desmet. An efficient wave based prediction technique for dynamic plate bending problems with corner stress singularities. *Computer Methods in Applied Mechanics and Engineering*, 198:2227–2245, 2009.
154. C. Vanmaele, K. Vergote, D. Vandepitte, and W. Desmet. Simulation of in-plane vibrations of 2D structural solids with singularities using an efficient wave based prediction technique. *Computer Assisted Mechanics and Engineering Sciences*, 19:135–171, 2012.
155. C. Vanmaele. *Development of a wave based prediction technique for the efficient analysis of low- and mid-frequency structural vibrations*. KU Leuven, division PMA, PhD. thesis 2007D11, 2007.
156. E. Deckers, N.-E. Hörlin, D. Vandepitte, and W. Desmet. A Wave Based Method for the efficient solution of the 2D poroelastic Biot equations. *Computer Methods in Applied Mechanics and Engineering*, 201-204:245–262, 2012.
157. E. Deckers, B. Van Genechten, D. Vandepitte, and W. Desmet. Efficient treatment of stress singularities in poroelastic Wave Based models using special purpose enrichment functions. *Computers & Structures*, 89:1117–1130, 2012.
158. E. Deckers, D. Vandepitte, and W. Desmet. A Wave Based Method for the axisymmetric dynamic analysis of acoustic and poroelastic problems. *Computer Methods in Applied Mechanics and Engineering*, 257:1–16, 2013.
159. S. Jonckheere, E. Deckers, B. Van Genechten, D. Vandepitte, and W. Desmet. A direct hybrid Finite Element Wave Based Method for the steady-state analysis of acoustic cavities with poro-elastic damping layers using the coupled Helmholtz-Biot equations. *Computer Methods in Applied Mechanics and Engineering*, 263: 144 – 157, 2013.

160. K. Vergote. *Dynamic analysis of structural components in the mid frequency range using the wave based method, Non-determinism and inhomogeneities*. KU Leuven, division PMA, PhD. thesis 2012D03, 2012.
161. B. Van Genechten. *Trefftz-based mid-frequency analysis of geometrically complex vibro-acoustic problems - hybrid methodologies and multi-level modelling*. KU Leuven, division PMA, PhD. thesis 2010D08, 2010.
162. J.B. Keller and D. Givoli. Exact non-reflecting boundary conditions. *Journal of Computational Physics*, 82: 172–192, 1989.
163. J.S. Lee, E. Deckers, S. Jonckheere, and W. Desmet. A direct hybrid wave based finite element modeling of poroelastic materials. In *Proceedings of the Symposium on the Acoustics of Poro-Elastic Materials, SAPEM2011, Ferrara (Italy)*, 2011.
164. O. Atak, B. Bergen, D. Huybrechs, B. Pluymers, and W. Desmet. Coupling of boundary element and wave based methods for efficient solving of complex acoustic multiple scattering problems. *Submitted for publication to Journal of Computational Physics (in review)*, 2013.
165. K. Vergote, B. Van Genechten, D. Vandepitte, and W. Desmet. On the analysis of vibro-acoustic systems in the mid-frequency range using a hybrid deterministic-statistical approach. *Computers & Structures*, 89:868–877, 2011.
166. J.S. Bolton, N.-M. Shiau, and Y.J. Kang. Sound transmission through multi-panel structures lined with elastic porous materials. *Journal of Sound and Vibration*, 191: 317–347, 1996.
167. T.E. Vigran, L. Kelders, W. Lauriks, P. Leclaire, and T.F. Johansen. Prediction and Measurements of the Influence of Boundary Conditions in a Standing Wave Tube. *Acta Acustica United with Acustica*, 83:419–423, 1997.
168. J.F. Allard. *Propagation of Sound in Porous Media: Modeling Sound Absorbing Materials*. Elsevier, New York, 1st edition, 1998.
169. G.B. Sinclair. Stress singularities in classical elasticity - I: Removal, interpretation and analysis. *Applied Mechanics Reviews*, 57:254–297, 2004.
170. E. Deckers. *A wave based approach for steady-state Biot models of poroelastic materials*. KULeuven, Department of Mechanical Engineering, PhD. thesis 2012D12, 2012.
171. F. Brezzi and M. Fortin. *Mixed and hybrid finite element methods*, volume 15. Springer series in computational mathematics, 1991.
172. B. van Hal, W. Desmet, D. Vandepitte, and P. Sas. Hybrid finite element - wave based method for acoustic problems. *Computer Assisted Mechanics and Engineering Sciences*, 11:375–390, 2003.
173. J. Descheemaeker. *Elastic characterization of porous materials by surface and guided acoustic wave propagation analysis*. KU Leuven, Department of physics, PhD. thesis, Leuven, 2011.